ENGINEERING FLUORESCENT NANODIAMONDS AND UPCONVERSION NANOPARTICLES FOR BIO-IMAGING AND OPTICAL TEMPERATURE SENSING

A Dissertation

by

MASFER HASSAN A. ALKAHTANI

Submitted to the Office of Graduate and Professional Studies of
Texas A&M University
in partial fulfillment of the requirements for the degree of

DOCTOR OF PHILOSOPHY

Chair of Committee,	Philip R. Hemmer
Co-Chair of Committee,	M.Suhail Zubairy
Committee Members,	Aleksei Zheltikov
	Carmen L. Gomes
Head of Department,	GrigoryV. Rogachev

May 2018

Major Subject: Physics

ABSTRACT

An ideal fluorescent marker for high contrast imaging and optical temperature sensing in biological applications should be biocompatible, ultrasmall, photostable, and can be excited and detected within the biological transparency window (650-1350nm). To meet these criteria, fluorescent nanodiamonds (FNDs) and upconversion nanoparticles (UCNPs) doped with lanthanide ions Ln^{+3} (Ln=Er,Tm,Ho,etc.) are of interest.

First, multi-color fluorescent nanodiamonds (FNDs) containing variety of color centers are promising fluorescent markers for most of biomedical applications. Compared to colloidal quantum dots and organic dyes, FNDs have the advantage of lower toxicity and better photostability. FNDs can be as small as fluorescent proteins, for example, green fluorescent protein (GFP) with a few nanometers (nm) in size and have exceptional chemical stability. They can be surface functionalized by techniques similar to those used for other nanoparticles. They exhibit a variety of emission wavelengths from visible to near infrared, with narrow or broad bandwidths depending on their color centers. In addition, some color centers can detect changes in magnetic fields, electric fields, and temperature. In this dissertation, I will discuss a new technique of grown small and stable fluorescent nanodiamonds. I will also discuss some applications of FNDs in bioimaging and biosensing.

Second, Upconversion nanoparticles (UCNPs) are of interest because they allow suppression of tissue autofluorescence and are therefore visible deep inside biological tissue. Compared to upconversion dyes, UCNPs have a lower pump intensity threshold, better photostability, and less toxicity. Recently, $YVO_4 : Er^{+3}, Yb^{+3}$ nanoparticles were shown to exhibit strong up-conversion luminescence (UCL) with a relatively low 10 $kW.cm^{-2}$ excitation intensity even in water, which makes them excellent bio-imaging and biosensors candidates. In this dissertation, I will discuss the UCNPs in terms of synthesis, applications in bioimaging and biosensing.

DEDICATION

To my mother, my father, and my family.

ACKNOWLEDGMENTS

First, I would like to thank my supervisor, professor Philip Hemmer, for his guidance, encouragement, and helpful advices which inspired me during my PhD study. I have been so lucky to have a professor who is a pioneer and world expert in his field. It was a great opportunity to spend my PhD program in his laboratories and gain enough knowledge and excellent research skills.

Second, I also would like to express my greatest appreciation to professor M. Suhail Zubairy for offering me an admission to Texas A&M University. His excellent teaching and advices guided me throughout my PhD study.

Third, I would like to thank Dr. Fahad Alghannam, professor Mohammad Al-amri, professor Carmen L. Gomes, professor Robert Brick, and professor Marlan Scully for their valuable discussions and successful collaborations.

Fourth, I would like to thank my family for their unlimited support during my PhD study.

Finally, I would like to thank King Abdulaziz city for science and technology (KACST) for funding my scholarship.

CONTRIBUTORS AND FUNDING SOURCES

Contributors

We gratefully acknowledge the offer of the fluorescent nanodiamonds used in chapter 3 by professor Arfaan A. Rampersaud from Columbus NanoWorks Inc.company.

We gratefully acknowledge the offer of fire ants used in chapter 4 by professor Hong Liang from the mechanical engineering department at Texas A&M University.

We gratefully acknowledge the offer of bovine embryos for use in chapter 6 by the Center for Reproductive Sciences of the College of Veterinary Medicine and Biomedical Sciences at Texas A&M University.

All other work conducted for the dissertation was completed by the student independently.

Funding Sources

We acknowledge the support of the TAMU CRI and GRUI grants, King Adulaziz City for Science and Technology (KACST), Saudi Arabia, the Office of Naval Research Grant N00014-16-1-3054 and the Robert A. Welch Foundation Award A1261.

TABLE OF CONTENTS

LIST OF FIGURES

FIGURE Page

LIST OF TABLES

TABLE Page

1. INTRODUCTION AND LITERATURE REVIEW

1.1 Introduction

Conventional fluorescent markers have attracted special attentions, especially, for high contrast imaging [1–6] and precise optical temperature sensing [7–11] in biological applications. These include quantum dots (QDs) [3, 4, 7, 8], organic dyes [2, 5, 9, 10, 12], fluorescent polymers [11] and thermal imaging [13]. Most of these fluorescent nanothermometers are good imaging agents and sensitive enough to detect a sub-kelvin rise in temperature in living cells [7–11, 13–15]. However, many of the existing nanothermometers are limited by photostability [2–10], toxicity [2–10, 16], and chemical environment sensitivity [11]. An ideal fluorescent marker for such interesting applications should be biocompatible, ultrasmall, photostable, and can be excited and detected within the biological transparency window (650-1350nm). To meet these criteria, fluorescent nanodiamonds (FNDs) and upconversion nanoparticles (UCNPs) doped with lanthanide ions Ln^{+3} (Ln=Er,Tm,Ho,etc.) are of interest because they allow visible deep imaging inside biological tissues. Also they both have shown precise optical temperature measurements in living organisms. In this dissertation, we will discuss both FNDs and UCNPs fluorescent markers in term of growth/synthesis and applications.

1.1.1 Fluorescent nanodiamonds (FNDs)

1.1.1.1 Overview

Over the past decades, efforts have been focused on the development of fluorescent nanoparticles to analyze complex biological processes as well as to track and localize individual drugs, proteins, nucleic acids and small molecules [17–21]. Ideal fluorescent nanoparticles should exhibit most if not all of the following features: 1) high sensitivity, down to a single molecule level, 2) high spatial resolution (with correspondingly small size at the nanoscale), 3) high molar absorption coefficient at the excitation wavelength with high fluorescence quantum yield, 4) absence of blinking and photo bleaching for real-time imaging, 5) robust surface chemistry, 6) biocompatibility, and 7) lack of toxicity. Furthermore, a suitable fluorescent marker should be conveniently excitable and detectable in the biological transparency window to avoid simultaneous excitation of endogenous fluorescent molecules such as blood constituents, cofactors and water. Unfortunately, most fluorescent markers do not possess all of these features.

The most widely used fluorescent markers are organic dyes, such as rhodamine, coumarin and cyanine dyes and their derivatives. Within the group of dyes, we could also include fluorophores that are part of a protein's structure (such as phycobiliproteins and fluorescent proteins that can be genetically encoded) [22]. While most organic dyes exhibit moderate to high quantum yields, many are photolabile and undergo photobleaching during continuous excitation. The Stokes shift (the difference between the spectral positions of the maxima of the absorption and emission spectra) [23] for most fluorescent dyes are often very small [24] which poses problems such as cross-talk between different dye molecules. Additionally, the intensity of the fluorescence depends on the local environment and can be influenced by pH, hydrophobicity, temperature and solvent [23]. The only fluorophore that is FDA approved for clinical use is the organic dye indocyanine green (ICG) [25]. However, ICG suffers from very low fluorescence quantum yield, limited stability and binding to plasma proteins.

Fluorescent nanoparticles overcome some of the limitations of organic dyes, such as quenching and environmental factors, and can be separated into a few distinct groups quantum dots [16, 26], upconverting nanoparticles [27–29], gold nanoparticles [30], carbon dots [31] as well as a large group that can be described as dye-doped polymeric nanoparticles [30] . Quantum dots (QDs) are clusters of semiconductor nanocrystals, created from II/VI and III/V elements, that display size-dependent luminescence [16, 26]. QDs absorb photons in the ultraviolet region then emit photons at longer wavelengths, in a size-dependent fashion. Relative to organic dyes, QDs exhibit non-quenching fluorescence, with large Stokes shifts, high fluorescence quantum yields, and can be made in an ultrasmall size (< 2nm) for single molecule imaging [16, 26]. However, QDs have not gained broad and substantial acceptance in the biological sciences due in part to the known toxicity of the Cd that forms the core of most QDs. While it is possible to coat the Cd core with a protective shell, their biocompatibility is still debated [16, 32], largely due to concerns about leaking of Cd^{2+}, and cytotoxic surface ligands [33] . On the other hand, upconverting nanoparticles (UCNPs) and gold nanoparticles have good biocompatibility and photostability but show low fluorescence quantum efficiency [27,28,34,35].

Fluorescent nanodiamonds (FNDs), owing to their unique optical and chemical properties, are proposed to be the best alternative probes that can meet the ideal fluorescent marker's criteria. In this chapter, I will discuss FNDs in terms of optical properties, biocompatibility, some demonstrations of their use in bioimaging and biosensing, and new color centers that have recently been discovered in diamonds.

1.1.1.2 Optical properties

Fluorescent nanodiamonds (FNDs) have important optical, chemical, and photochemical, and photophysical properties that make them excellent fluorescent markers. FNDs have color centers defects that act like isolated atoms or molecules in a solid host. Therefore, photoluminescence of FNDs originates from local defects (color centers) in nanodiamond crystals and, at least in principle, is not expected to be strongly affected by crystal size until the nanodiamond size becomes less than 5 nm. FNDs unique bright and photostable photo-luminescence cover a wide range of the VIS to NIR spectrum-for instance; blue emission for N3 center diamonds, green emission for H3 (N2V) complex, red-NIR emission for nitrogen-vacancy NV-centers, silicon-center (SiV), germanium-vacancy (GeV), tin-vacancy (SnV) and Nickel center (Ni) color centers) [36–41] as shown in Figure 1.1 [42]. Here it is important to note that new color centers are being discovered on a monthly basis, as only a fraction of the periodic table has so far been implanted into diamond [43]. Many of new color centers are narrowband as preferred for bio-markers, especially for large-atom implantation.

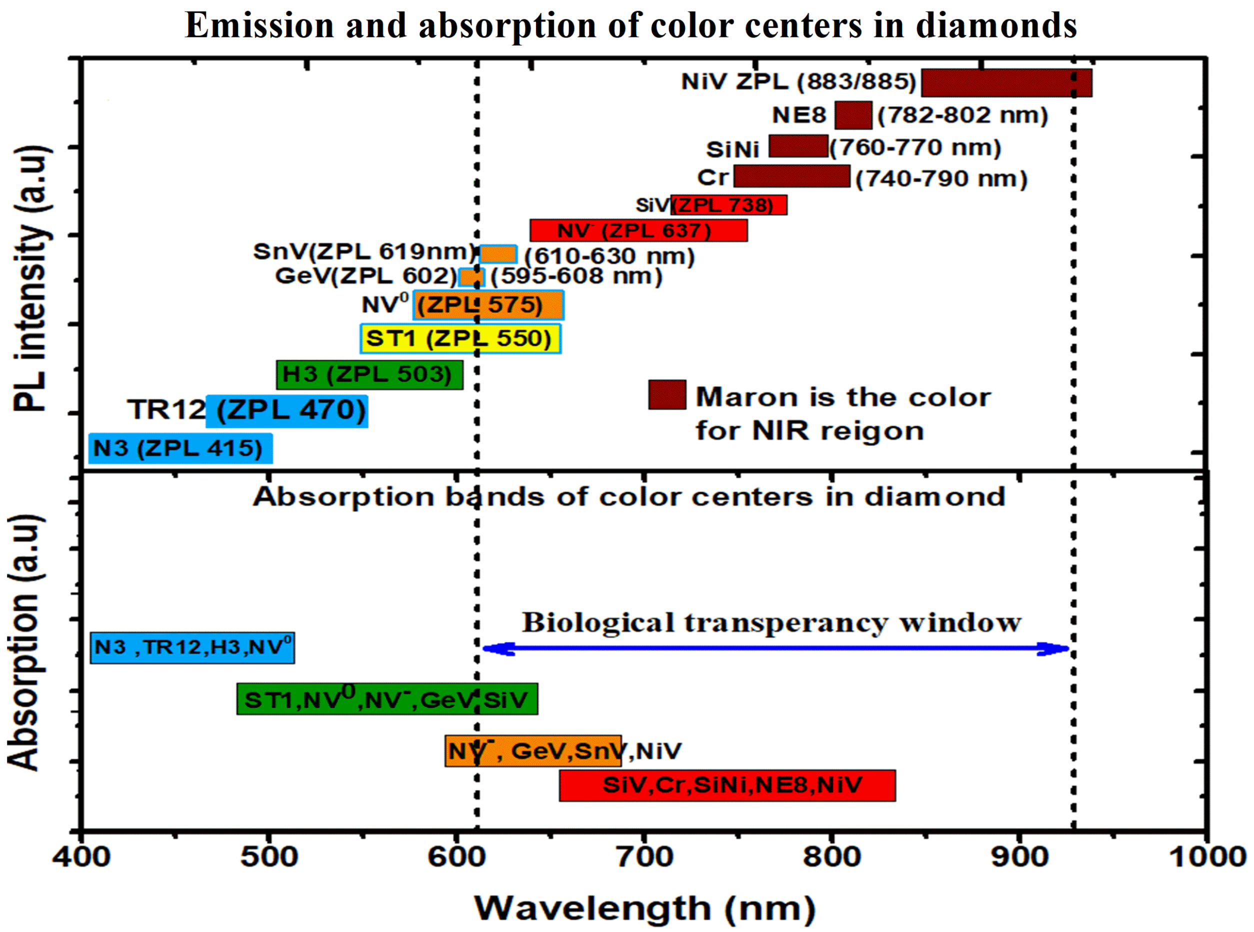

Figure 1.1: Absorption and emission bands of most of the color centers in diamonds.

Before introducing the physics of Nitrogen-vacancy (NV center), it has been reviewed in detail in [39]. Briefly, the NV color center is formed by a nitrogen atom and adjacent lattice vacancy in diamond lattice as shown in Figure 1.2(a). The electronic structure of the NV center consist of six electrons. These electrons are formed by nitrogen atom (two electrons), dangling bonds from the three carbon atoms surrounding the vacancy (three electrons) and the sixth electron is captured from the diamond lattice (typically, nitrogen donors) as shown in Figure 1.2(b). This electronic configuration forms negatively charged state NV center. The electronic structure of the NV^- center consist of three electronic levels, ground state (^3A), excited state (^3E), and singlet state (^1A).

The ground and excited states are spin triplet (S=1) which split into three spin sublevels. The unique photoluminescence of NV center appears when NV center get excited at most excitation wavelengths (450nm-640nm) via the main transition from ground state to excited state. The emission of the NV center is located in red to NIR bands between 630 and 800 nm with zero-phonon lines of the neutral and negatively charged NV centers peaked at 575nm and 637nm, respectively as shown in Figure 1.2(c). The quantum yield of the NV color center has been reported to be approximately 70-80% [44].

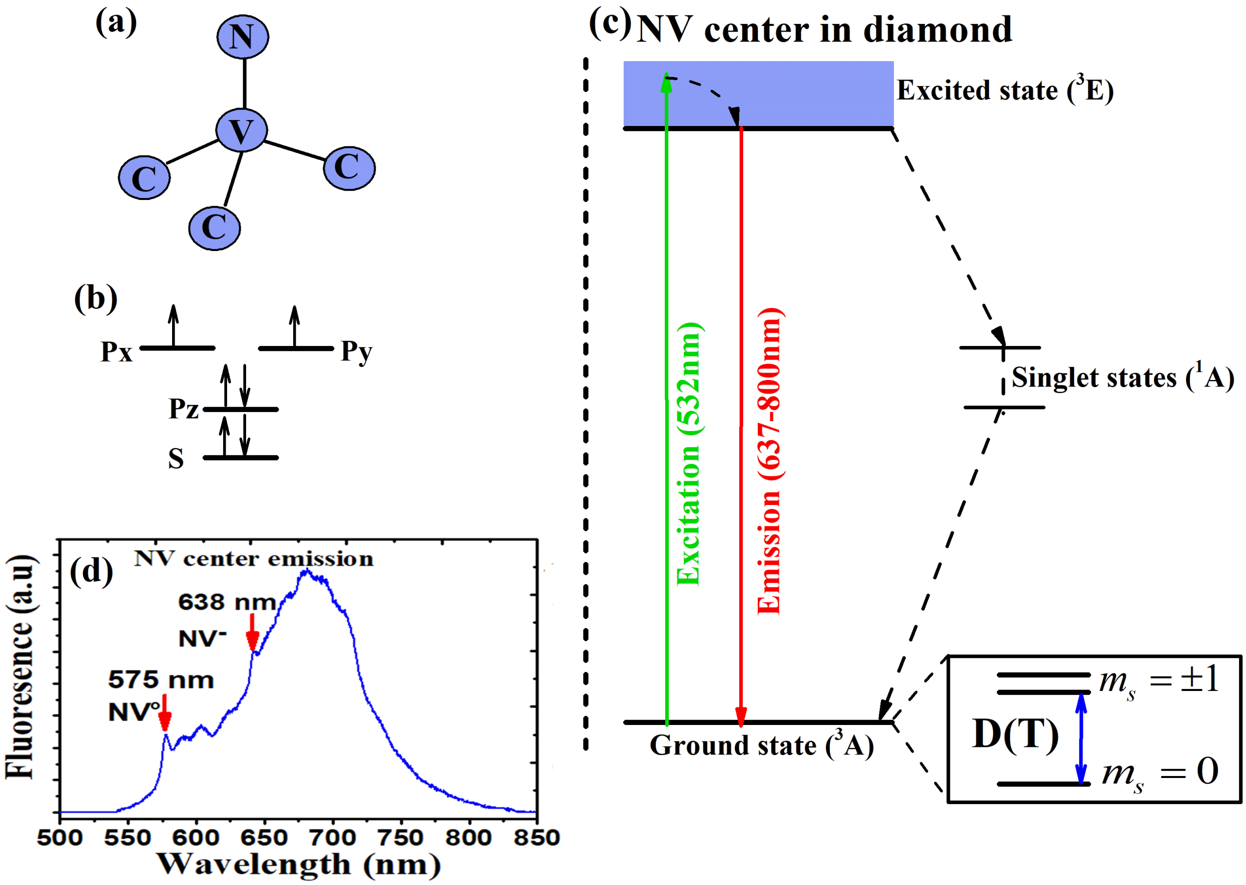

Figure 1.2: (a) The NV center consists of a vacancy with an adjacent substitutional nitrogen atom. (b) The NV- has a spin triplet ground state due to C_{3v} symmetry causing a degeneracy. (c) The energy levels of the NV showing all the electronic states, optical pumping and emission. (d) Photoluminescence emission spectra of NV center revealing the NV^o and NV^- zero-phonon lines (ZPL) peaks at (575 nm and 638 nm) respectively.

Interestingly, NV center have considerable potential in quantum limited sensing of important physical quantities such as magnetic fields [45], electric fields [46] and temperature [47]. For magnetic field sensing, a single NV center in an ultra-pure bulk diamond can detect magnetic fields with sensitivity of a few nT/$\sqrt{Hz}$ [48,49]. In principle this has nanometric spatial resolution owing to the small size of the NV [50]. For biological applications, magnetic field detection has been proposed to non-invasively monitor neuron firing [51, 52], and electric fields to monitor membrane potentials [39].

The NV color center senses magnetic fields via the optically detected magnetic resonance (ODMR) [39]. Briefly the NV has a S = 1 spin ground state which is split into three spin sublevels ($m_s = \pm 1$ and $m_s = 0$) with zero-field splitting D = 2.87 GHz due to spin-orbit interactions and the diamond crystal field as shown in Figure 1.3(a) [50, 53]. The optical pumping excitation polarizes the NV center into the $m_s = 0$ spin sublevel via intersystem crossing to an intermediate S=0 singlet state. This crossing occurs only for spins in the $m_s = \pm 1$ states which then decay into the $m_s = 0$ state. Since the intermediate singlet is dark and has a relatively long lifetime, NV spins with magnetic quantum number $m_s = 0$ fluoresce brighter, scattering 30% more photons than $m_s = \pm 1$ states. Hence, when a resonant microwave field induces magnetic dipole transitions between these spin sublevels it equalizes the spin populations, resulting in a significant decrease of the nitrogen-vacancy center fluorescence [50]. Due to symmetry, the $m_s = \pm 1$ sublevels of the nitrogen-vacancy defect are degenerate at zero magnetic field (B= 0), resulting in a single resonance line appearing in the ODMR spectrum as shown in Figure 1.3(b). An external magnetic field lifts the degeneracy of $m_s = \pm 1$, leading to the appearance of two lines. The external magnetic field can be measured from the positions of these two lines (w1 and w2) as shown in Figure 1.3(b). The separation between the ODMR two lines increases as the axial magnetic field increases [50], and in addition both lines can shift in the same direction for non-axial magnetic fields.

For electric field sensing, J.Wrachtrup and his co-workers have demonstrated electric-field sensitivity reaching $2026 V/cm.Hz^{-1/2}$ using the NV color center in bulk diamonds [46]. The electric field was generated by the application of a controlled voltage to a gold microstructure fabricated by lithography and electroplating directly on a bulk diamond sample containing NV centers as shown in Figure 1.3(c) [46]. To measure electric-field-induced shifts of spin sub-levels, they monitored the zero-field splitting of the $m_s = 0$ and $m_s = \pm 1$ transition which is split by the local crystal field. They observed a resonance line shift (or increase in the zero field splitting) of 28.4kHz corresponding to an electric field of about 3000v/cm. Figure 1.3(d) shows the shift of the ODMR resonance frequency for different voltages applied to the electrodes [46].

As already mentioned, M. Lukin and co-workers used the NV for temperature sensing at precision up to 1.8 mk/$\sqrt{Hz}$ in ultra-pure bulk diamond [14]. However in living cells the precision was only 200 mk/$\sqrt{Hz}$ due to the relatively worse spin linewidth in nanodamonds [14]. As discussed earlier, the mechanism of temperature measurement is the shift of the zero field splitting which is near D=2.87 GHz at room temperature as shown in Figure 1.3(e and f) [54, 55].

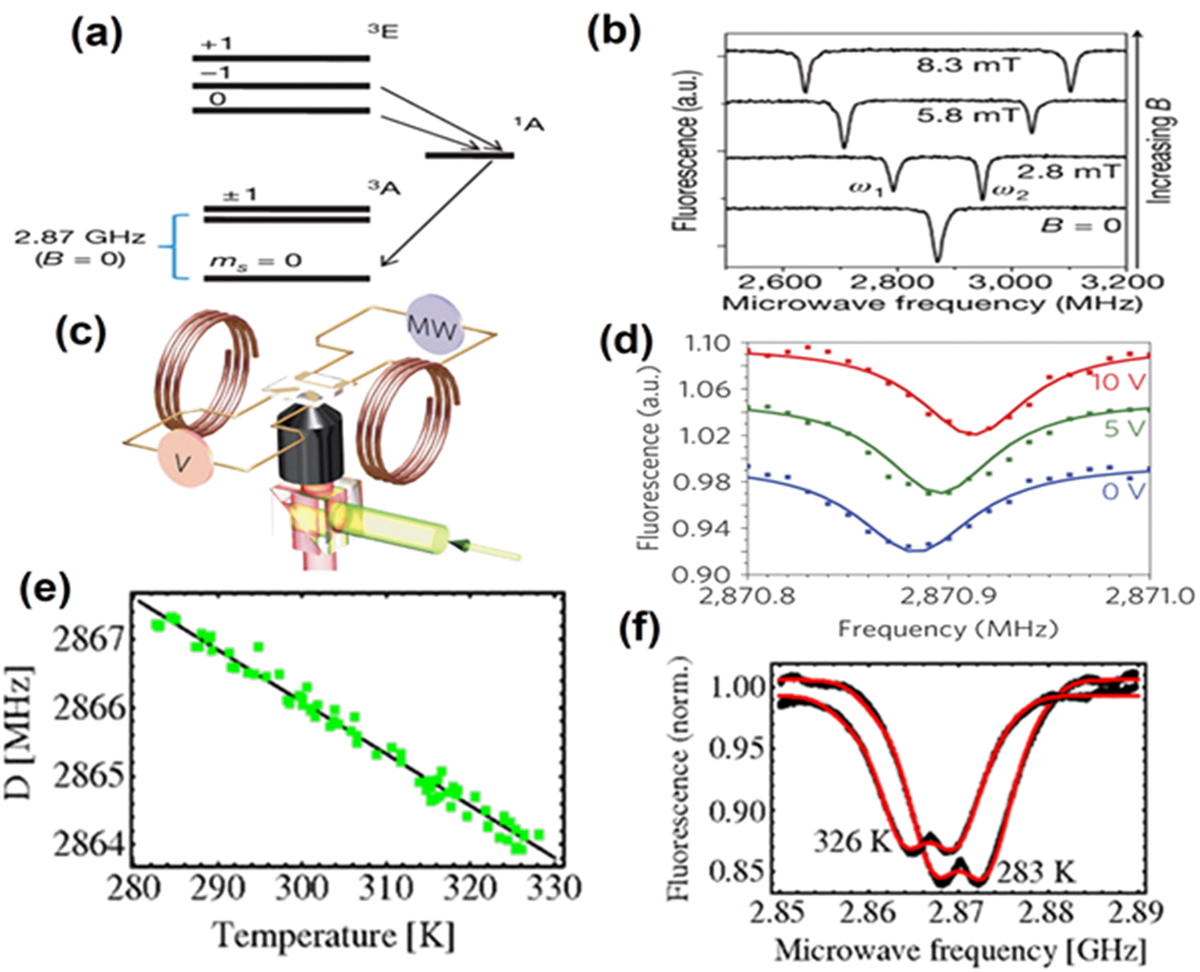

Figure 1.3: (a) An illustration of the energy level of the nitrogen-vacancy (NV) defect in diamond. (b) Optically detected magnetic resonance spectra (ODMR) for a single nitrogen-vacancy defect at increasing magnetic field (from bottom to top).(c) Schematic of the confocal set-up used with Helmholtz coils for magnetic field alignment and a microstructure on the diamond sample to create the electric field and coupled with the microwaves. (d) Observed shift of the ODMR resonance lines for different voltages applied to the electrodes, clearly showing the effect of a Stark shift.(e) A linear fit of the NV center ODMR spectra changes as a function of ambient temperatures. (f) ODMR changes linearly as a function of temperatures from 280 K to 330 K. Figures a and b reprinted with permission from [50];figures c and d reprinted with permission from [46];and figures e and f reprinted with permission from [55].

The brightness of NV-centers depends on the average number of emitting color centers per particle [56]. Recently, the brightness of these centers has been optimized as a function of size [57]. Accordingly, irradiated 100 nm FNDs (with NV color centers) are 12 times brighter than a conventional organic dye (Auto 532 dye) [57]. For small FNDs, with a size less than or equal to 20nm, brightness will decrease by about two orders of magnitude compared to that for 100 nm FNDs. Recent efforts have been made to optimize the brightness stability of small NDs down to 10nm (almost single emitter) and they are commercially available for biomedical applications [57].

1.1.1.3 FNDs biocompatibility

The toxicity of FNDs is entirely related to the surface purity. For example, nanodiamonds produced by detonation (DNDs) have been reported to have strong anti-bacterial properties if not well cleaned [58]. However, aggressively FNDs do not show this behavior. Additionally, functionalization can suppress toxicity of uncleaned DNDs, for example strong bonds (C-C bonds) can be created between the graphitic shell and the surface functional groups following Diels-Alder reactions [59] and diazonium chemistry [60].

However, it is preferable to remove the graphitic shell for quantum efficiency and phototoxicity considerations. This is normally done with aggressive oxidation both in liquid (boiling in acids) and in air at temperatures above 500 ^{o}C [61]. Once the surface has been cleaned to expose a pristine diamond surface, there are a number of functionalization strategies that have been applied. For example, one approach is to reduce all carboxyl-COOH groups to hydroxyl-OH. From this a silane linkage can be made, [62]or alternatively nitrogen can be attached directly to the surface carbon, serving as a basis for linkers like PEG, antibodies, proteins, DNA, etc [63–65]. Recently, Havlik et al developed a synthetic method to replace the carboxylic group on nanodiamonds(NDs) surface by fluorine using selective sp3-based radical chemistry [66]. This surface modification produces nanodiamonds with a highly hydrophilic interface with mixed C-F and C-OH terminations. These dual terminations on NDs surface suppress hydrophobic interactions which cause NDs agglomeration in solutions. Furthermore, fluorination of NDs leads to surface band-bending that stabilizes shallow fluorescent NV center in small size FNDs (especially size <100nm) [66]. All these surface advanced modifications make NDs suitable for a variety of biomedical applications

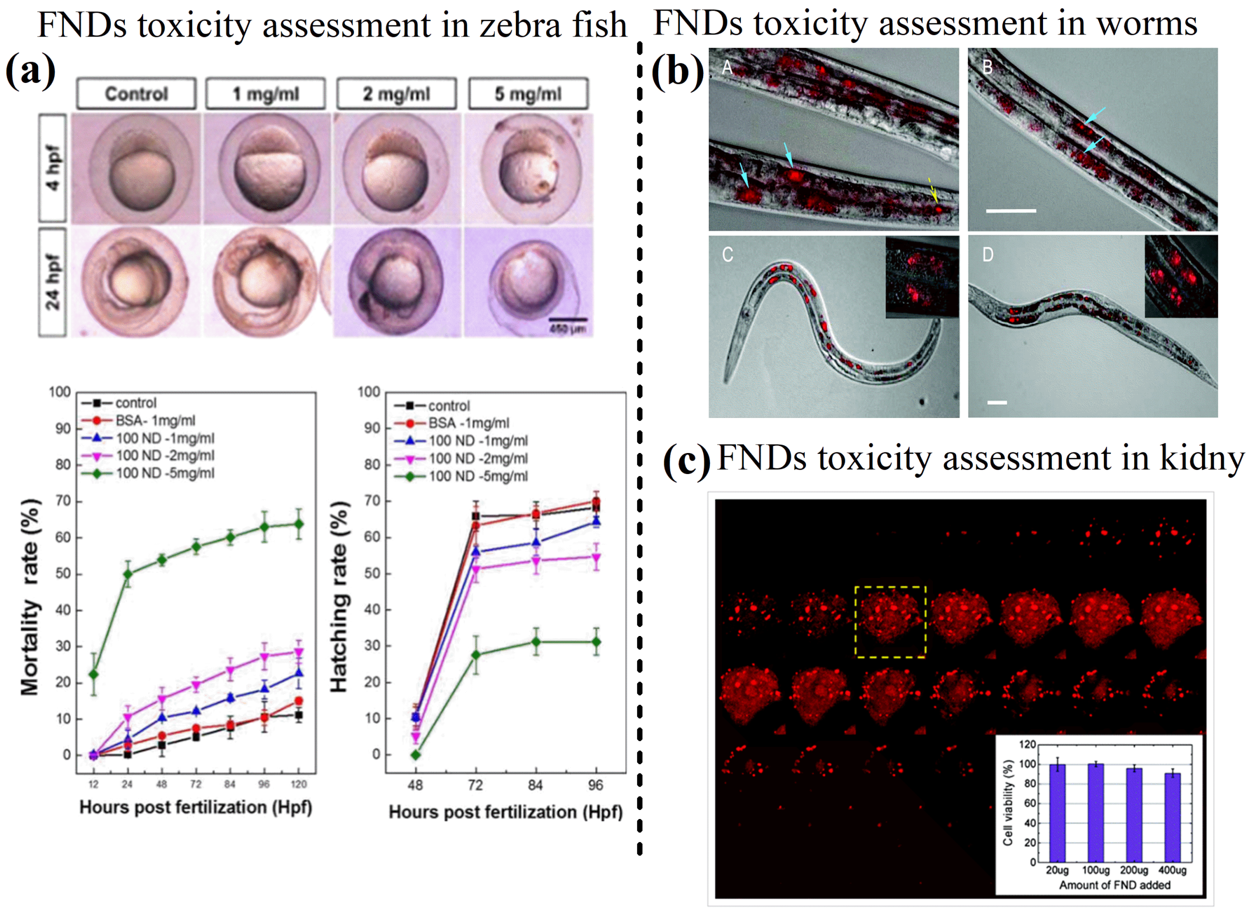

Figure 1.4: (a) Zebrafish embryos development stages with various concentrations of nanodiamond for different periods at 4 hour-post-fertilization (hpf) and 24 hpf (upper image in Figure 1.4(a)). Mortality and hatching of zebrafish embryos as a function of the NDs concentrations (lower image in Figure 1.4(a)). (b) Images of worms fed with FNDs coated with BSA and DOX. Insets: magnified images of the FNDs within the intestinal cells. (c) Optical images of a single human kidney cell after fluorescent nanodiamonds uptake. The red spots are the FNDs. Inset: Toxicity assessments of showing the survival percentage of the kidney cells versus the FNDs doses. Figure a reprinted with permission from[67];figure b reprinted with permission from[68];and figure c reprinted with permission from[69].

Toxicity assessments, after surface preparation, have been performed on FNDs by in vitro and vivo experiments. The most sensitive experiments were done by C.-L. Cheng and coworkers [67] who conducted toxicity tests of nanodiamonds (NDs) on the zebrafish embryo model in vivo. This model is especially sensitive to toxicity at critical stages of embryo development. They found that for ND concentrations below 1 mg/ml, even in the critical stage, zebrafish embryos exhibit similar development as compared to the control groups, as shown in Figure 1.4(a). However, at higher concentrations, the NDs affect the zebrafish embryos at the Pharyngula stage as shown in Figure 1.4(a). The results suggested that NDs are safe as a drug delivery agent for concentrations below 1 mg/ml [67]. In earlier work, FNDs also were fed to worms (C. Elegans) and did not cause any detectable stress to the worms for several days as shown in Figure 1.4(b) [68]. Upon microinjection of the worms with FNDs, some were passed along to offspring without any apparent effect on development. Another early study showed low toxicity of fluorescence nanodiamonds (FNDs) after uptake by 293T kidney cells as shown in Figure 1.4(c) [69]. Recently, FNDs have been injected into groups of mice for more than five months at a dosage of up to 75 mg/ kg body mass and shown no evidence of toxicity, neither in the living animals, nor in the histopathological examinations [70]. In another important study on nanodiamonds toxicity assessment, 0.002 to 0.05 wt% of NDs hydrosols were given to mice instead of water for 6 months and showed no significant effects on growth rates or organs weight or reproductive rates for at least 3 generations [71]. For more extensive discussion of ND toxicity including those with cleaned and uncleaned surfaces a recent review is recommended [61].

1.1.1.4 Application of FNDs in drug delivery

Drug delivery is one of earliest bio-medical applications for nanodiamonds (NDs) that has been investigated. Initially non-fluorescent nanodiamonds were used.

First, Early studies on the use of nanodiamonds as drug delivery vehicles were reported by the group of Ho in 2007 [72]. These studies showed that the chemotherapeutic agent doxorubicin (DOX) could be passively absorbed onto the surface of non-fluorescent nanodiamonds to create nanodiamond-drug complexes (NDX) then delivered into cancer cells with preserved efficacy, as well as slow and sustained DOX release [72, 73]. The NDX treatment overcomes a problem seen with drug resistant tumors in which transporter proteins facilitate the efflux of drug compounds out of the cell, markedly decreasing, or precluding treatment efficacy. A mechanism of how these nanodiamonds act to circumvent drug resistance is shown in Figure 1.5(a) [74]. Similarly, absorption and delivery of other drugs have been reported including, anticancer agents mitoxantrone

(MTX), cisplatin, 4-hydroxytamoxifen (4-OHT), and purvalanol A [75–78], an anti-inflammatory drug dexamethasone [78], and the diabetes drug insulin [79].

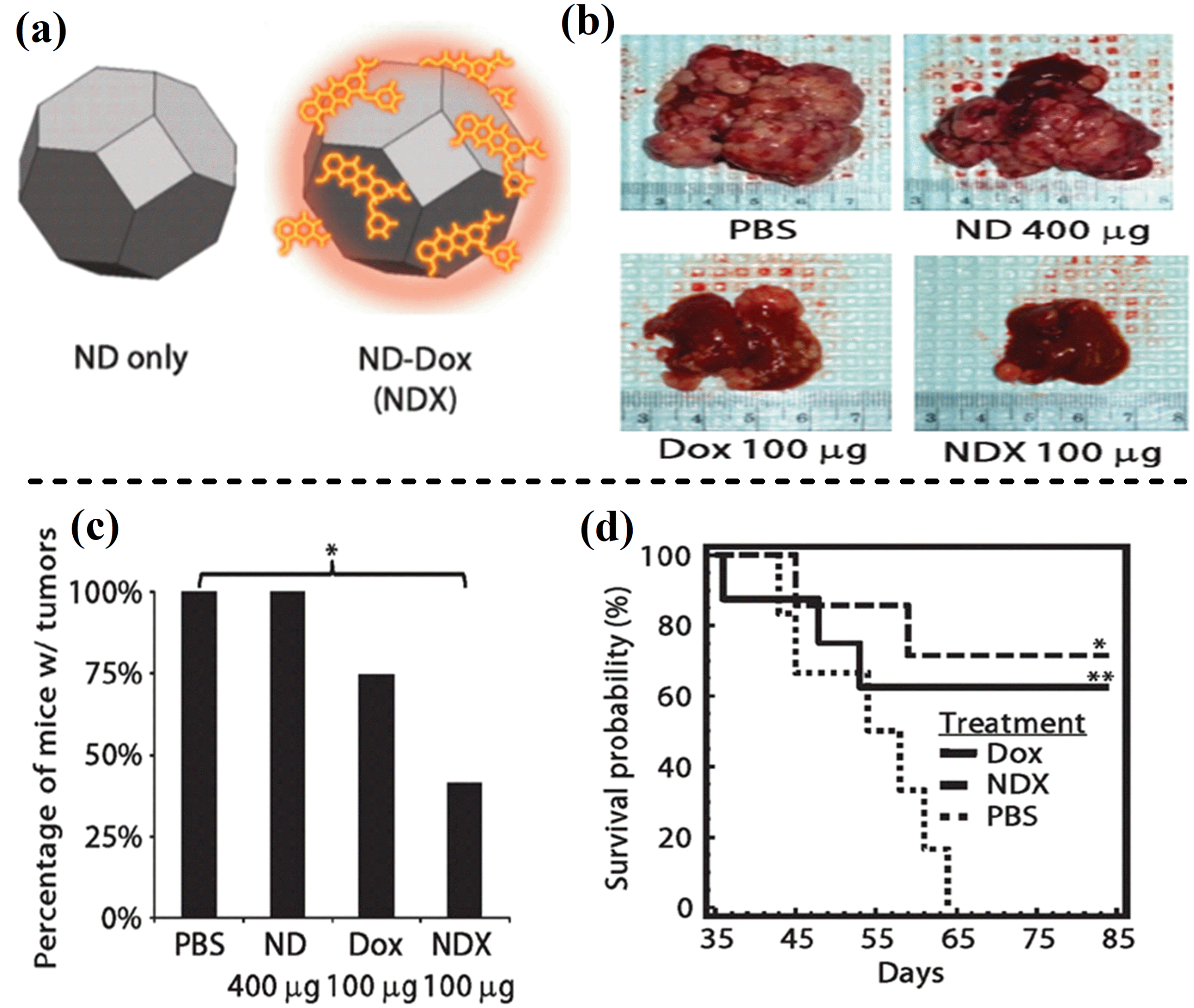

Figure 1.5: (a) Scheme of ND and ND with DOX(NDX). (b) Images of livers/tumors from treated mice with PBS, ND 400 μg, Dox 100 μg , and ND-Dox 100 μg. (c) Percentage of mice exhibiting macroscopic tumor nodules (defined as >1 mm). *P < 0.03. (d) Kaplan-Meier survival plot for LT2-Myc mice treated with PBS (n = 5), DOX (100 g) (n = 8), or NDX (100 g of Dox equivalent) (n = 7) by tail vein injection every 7 days. *P < 0.03; **P < 0.06. Reprinted with permission from[74].

In preclinical experiments, the NDX complex was shown to inhibit tumor growth in both murine LT2-Myc liver tumor and 4T1 mammary tumor without affecting normal tissues [73]. Figure 1.5(b) [74] shows that treatment with 100 g of a Dox equivalent of either free Dox or NDX effectively inhibited liver tumor growth, with a measurable preference for NDX. ND with Dox has decreased the percentage of mice with tumors, after treatment, to less than 50% and increased the survival probability over a long period of time as shown in Figure 1.5(c and d) [74]. In additional safety studies, NDX was found not to elicit myelosuppression, which is an unwanted side effect of free DOX chemotherapy underlying patient mortality.

Second, In general, fluorescent nanodiamonds (FND) are normally made from crushed high-pressure high-temperature (HPHT) bulk diamonds or in some cases CVD-grown nanodiamonds, as these are typically much brighter than detonation diamonds. Therefore, for drug delivery non-detonation FNDs are preferred as discussed in two studies [80, 81]. In the second of these studies, FNDs were coated with biopolymers and proteins to ensure colloidal stability and conjugated to DOX molecules for treatment of cancer cell lines. The FNDs-DOX complex uptake and drug release process in a cancer cell is illustrated in Figure 1.6(a) [81]. The FNDs-DOX complex was photostable inside living cells, as shown in Figure 1.6(b) [81]. Figure 1.6(c) shows that the fluorescence of the NV color center in diamond overlaps with emission of doxorubicin, but this can be subtracted to show the NV-centers alone. Significant amounts of DOX were released from ND carriers in these studies and in other experiments, FNDs-DOX have shown efficient tumor inhibition of human cancer cells over time, as shown in Figure 1.6(c and d) [81]. Furthermore, tumor luminescence decreased to very low percentages over time, as shown in Figure 1.6(f), which indicates the cancer fighting effect of FNDs-DOX in human cancer [81]. All the advantages above-mentioned indicate that FNDs are intriguing candidates as delivery platforms for chemicals and antibodies.

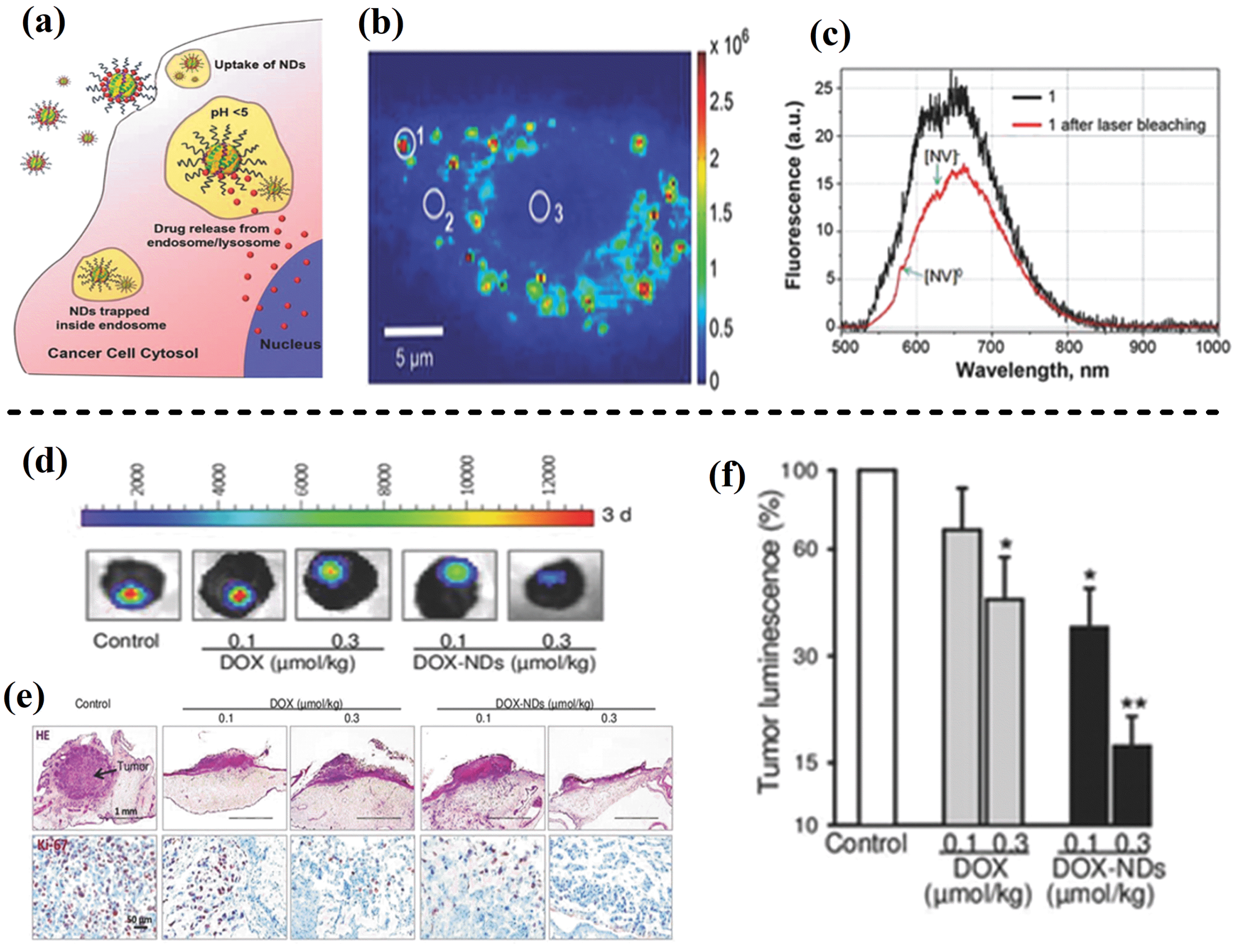

Figure 1.6: (a) Demonstration of living cell uptake and drug release process of DOX-ND. (b) Fluorescence spectra of fluorescent DOX-NDs inside living (A549) cells. (c) Black curve represents the overlapping emission spectra of DOX and NV centers. The red curve illustrates the emission spectrum after laser bleaching of the DOX emission showing a clear NV center spectrum with NVo and NV- peaks at 575 nm and 638 nm, respectively. (d) Human cancer xenografts treated with NDs-DOX after three days. (e) Breast cancer cells treated with DOX-ND over time. NDs-DOX treatment reduced the cancer cell proliferation in a dose-dependent manner. (f) Luminescence imaging analysis of tumor xenograft growth after 3 days treatment by NDs-DOX. Reprinted with permission from[81].

1.1.1.5 Applications of FNDs in temperature sensing in living cells and neurons

Luminescence nano-thermometry has been demonstrated using quantum dots (QDs), organic dyes, gold nanoparticles (GNPs), and polymers to measure temperature changes in intracellular environments [7, 9, 15, 82]. However, many of these fluorescent probes are limited by drawbacks including fluorescence fluctuations, such as photobleaching and blinking, particularly for dyes and QDs [7, 9], as well as fluorescence sensitivity to local environments [11]. The remarkable optical properties of nitrogen color centers (NV) in diamonds, which include photostability, spin long coherence time, and biocompatibility [83–85] make them one of the best alternatives for accurate temperature sensing.

Sensing temperature using the NV color-center in diamond has been well-studied [14, 86, 87]. An increase in environmental temperature (T) can induce crystal expansion, which shifts the zero-field splitting of ground state toward smaller values as temperature is increased, as shown in Figure 1.7(a) [37, 88]. These shifts were detected by optically detected magnetic resonance (ODMR) [39]. The first application of fluorescent nanodiamonds (FNDs) as nano-thermometers in living organisms was done by M. Lukin et al. in 2013 [14]. They used 100 nm nitrogen-vacancy color center nanodiamonds to measure the local temperature of human living cells with a precision of 200 mK/$\sqrt{Hz}$ and a spatial resolution of 200 nm. Briefly, they injected laser-excited gold nanoparticles as a heat source (cross symbol) together with diamond nanocrystals inside the living cells and used the NV center for thermometry (circle symbol), as illustrated in Figure 1.7(b). They precisely measured the change in temperature at the position of NV1 and NV2 relative to the incident laser power applied to the Au NPs, as shown in Figure 1.7(c and d) [14].

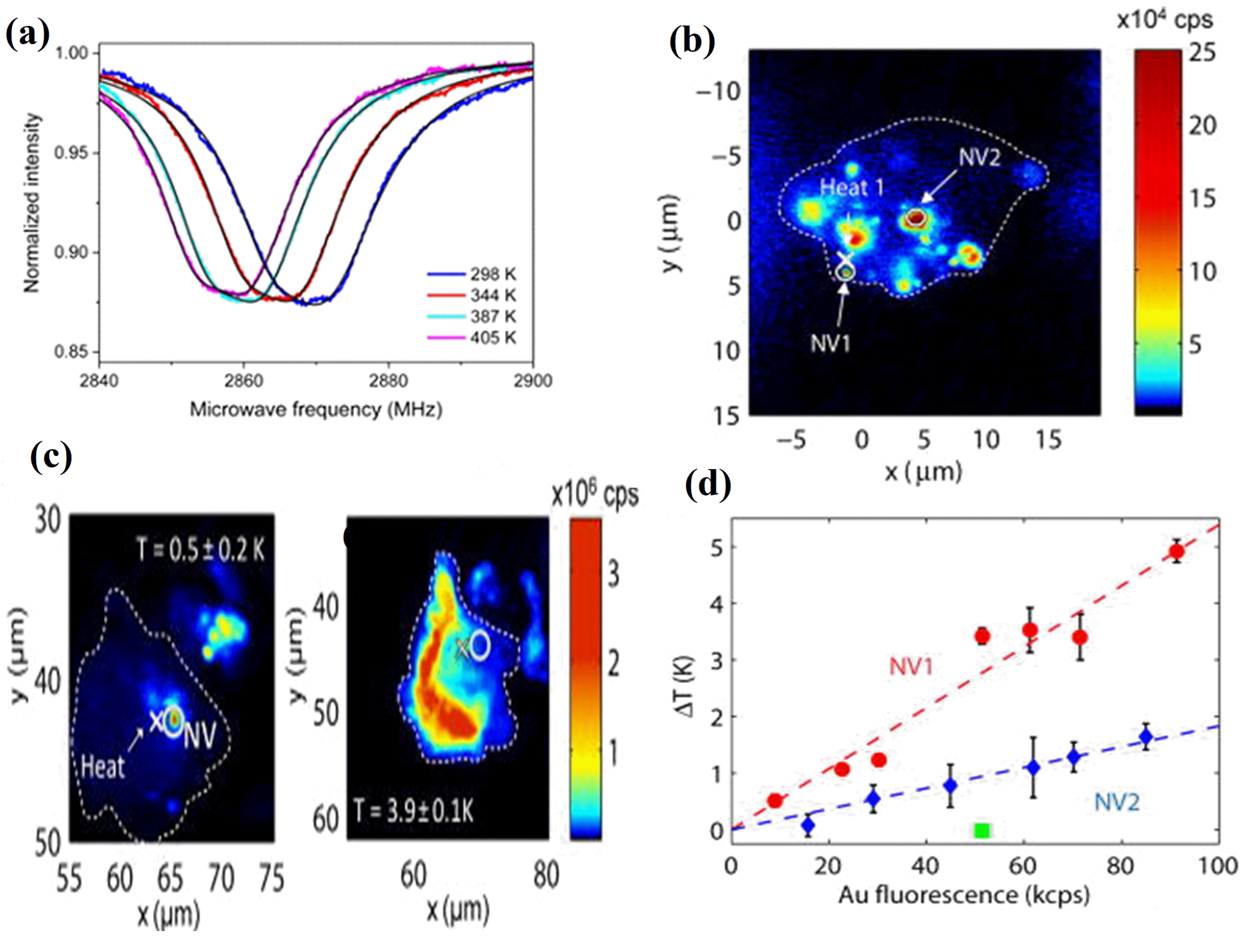

Figure 1.7: (a) ODMR spectra of the NV color center change as a function of local temperature changes. (b) A single living cell injected with fluorescent nanodiamonds and gold nanoparticles (Au NPs) as the heating source and nanoscale thermometer, respectively; followed by excitation under 532 nm. The position of the Au NP is indicated by small cross, while circles represent the location of the NV color centers in nanodiamonds used for thermometry. (c) Measurement of temperature changes precisely as the laser power increases with 0.1 K precision. (d) The change in temperature at the position of NV1 and NV2 relative to the incident laser power applied to the Au NP. Figure a reprinted with permission from [88];figures b-d reprinted with permission from[14].

Following this, there were several other notable achievements in the field of the NV-based nanoscale temperature sensing in biological applications [86, 89, 90]. Remarkably, Ning Wang and his co-authors [91] reported that the temperature sensitivity of the NV center in nanodiamonds can be increased by two orders of magnitude beyond the sensitivity reported in [14]. This was done using a hybrid nano-thermometer composed of NV centers and a magnetic nanoparticle (MNP), in which the temperature sensitivity is enhanced by the critical magnetization of the MNP near the ferromagnetic-paramagnetic transition temperature. In addition to NV, almost all narrowband emitters in diamond have temperature dependence and can be used as a nano-thermometer without the need for microwaves. For example, nano-thermometry with SiV [92] and GeV [93] have been explored recently, where in the case of SiV the excitation and emission is in the tissue transparency window.

Here, it is important to note that there has been some recent controversy in the field of cellular temperature measurement. Specifically, it was argued that the temperature changes reported by many experiments could not have been possible based on simple thermodynamic arguments, [94] and hence, there must have been unknown interferents present in the cells that led to false temperature readings. To address this controversy multi-modal temperature measurement is a good approach, in which two or more temperature probes simultaneously measure temperature. Provided these probes sense temperature by different physical mechanisms, they will not respond to interferents in the same way, and therefore false readings can be ruled out [95].

The temperature sensing capability of fluorescent nanodiamonds, together with their low toxicity suggests possible uses in the treatment of nervous system-related diseases and injuries. For example, monitoring the thermal state of the nervous system is very important to determine the effects of temperature on its operation. As a special case, consider neurons that sense warm, cold, and hot conditions, which have specialized ion channels that convert heat into action potentials [96–98]. Zheltikov and his co-workers have demonstrated the ability to accurately measure the local temperature of TRP-expressing mouse neurons using fiber-coupled nitrogen-vacancy(NV) centers in micron-size diamonds [99]. The mouse neuron was labeled with GCaMP6s fluorescence to serve as a calcium sensor which detects neuron firing via the inward Ca^{2+} current across the cell membrane. When the temperature reaches the neuron activation threshold (Ta =27.4^{o}C), neurons expressing transient receptor potential (TRP) action channels [99] begin to fire, producing spikes of GCaMP6s fluorescence. On the other hand, when the temperature decreases below the activation threshold, the fluorescence of the Ca^{+2} sensor in the neurons gradually decreases [99]. The temperature reading of single neurons obtained with the NV-diamond fiber sensor, strongly correlates with the fluorescence of the calcium-ion sensors. This study opens the door for eventually using fiber-mounted FNDs for temperature sensing in live brains.

1.1.1.6 Application of FNDs in super-resolution imaging

Fluorescence microscopy is an enormously powerful technique to study complicated biological structures down to the sub-cellular level in biological applications [100]. However, the diffraction limit of light is an obstacle that prevents detailed visualization of subcellular processes. In the past couple decades super-resolution imaging microscopy has overcome the diffraction limit of light. There are two main approaches: PALM/STORM and variants that rely on controlled bleaching and measurement of centroids, and stimulated emission depletion (STED)/Ground state depletion (GSD), which rely on the use of donut beams. STED microscopy works when two laser beams at different wavelengths are superimposed. The first (main) laser beam excites the fluorescent marker of interest to its excited state. The second laser beam with a doughnut shape at its focus, depletes the fluorescence from all molecules except those in the middle of the excitation volume. Consequently, the resultant (fluorescent volume) becomes smaller than the diffraction limit [37, 101], as shown in Figure 1.8(a) [101]. Hell and co-workers used diamond color centers in STED field and achieved a remarkable resolution of 6 nm by detecting single NV^- centers in bulk diamonds, as shown in Figure 1.8(b,c and d) [102, 103].

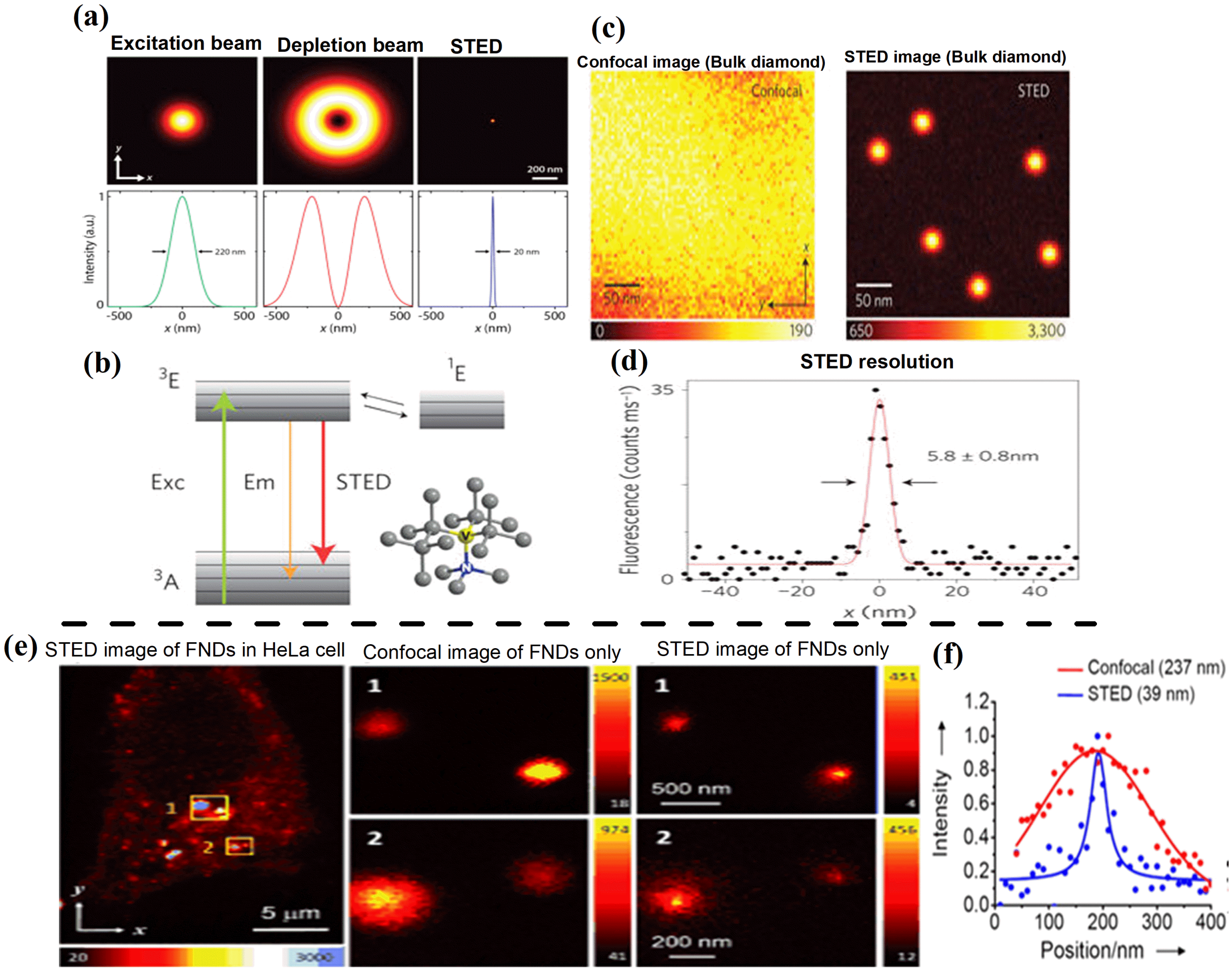

Figure 1.8: (a) An illustration of STED microscopy technique. (b) Energy levels of the triplet (left) and singlet states (right) of the NV center and the excitation beam (EXC), emission beam (Em), and stimulated emission (STED) transitions in nitrogen-vacancy centers. (c) Confocal and STED optical image of bulk diamond containing NV color centers. (d) STED high resolution for NV center in diamond, which reveals high spatial resolution reaching 5.8± 0.8 nm. (e) Confocal and STED imaging of HeLa cells labeled with BSA-conjugated FNDs through electroporation. STED images of single BSA-conjugated FND particles enclosed within the yellow boxes 1 and 2. (f) Display of confocal and STED resolution of NV centers within diamond nanocrystals. Figures b,c,and d reprinted with permission from[102];figures e and f reprinted with permission from[104].

The reason the nitrogen-vacancy color center in diamond gives such high spatial resolution with STED is due to its long-term photostability, even for very strong excitation intensities. For STED with nanodiamonds, a study by Tzeng et al [104] obtained a resolution of 40 nm of fluorescent nanodiamonds in HeLa cell, as shown in Figure 1.8(e and f). A later study by Stefan Hell and his co-workers [105] has also shown that individual NVs within single nanodiamonds can be resolved with 10 nm resolution, which is even smaller than the size of the nanodiamond (average size 40-250 nm). This study highlights the need for smaller nanodiamonds with stable color centers.

1.1.1.7 Application of FNDs in MRI imaging

Magnetic resonance imaging (MRI) is a powerful technique for high-contrast imaging, but it requires large DC magnetic fields to achieve good nuclear spin polarization at room temperatures. This is because of the small nuclear spin flip energy compared to the Boltzmann energy, kT. Electron spins, in contrast, have much larger polarization owing to their larger electron spin flip energy. By using the Overhauser effect [106], it is possible to transfer this electron polarization to the nuclear spins [107]. While many paramagnetic particles have been explored for this purpose [108–111], NDs have the advantage of excellent biocompatibility and chemical stability.

Recently, Waddington et al. [112] demonstrated a Overhauser-enhanced MRI (OMRI) technique [112–116] to image and track water-ND solutions. This is done by transferring the electron spin polarization of paramagnetic impurities at the surface of NDs to ^1H nuclei continually in the surrounding water [117]. To maximize the nuclear polarization efficiency, they use ultra-low magnetic fields (ULF) (6.5 mT) and low frequency RF (190 MHz) excitation, which have the advantage of being compatible with in vivo use. The result was switchable contrast enhancement at biologically relevant ND concentrations. In particular for this experiment, they focused on HPHT NDs with sizes of 18 nm and 125 nm in DI water at concentrations near 100 mg/mL [112].

The mechanism of the Overhauser effect from ND surface spin impurities to water is illustrated in Figure 1.9(a) [112]. Briefly, Overhauser effect occurs when a reservoir of polarized electron spins on the NDs's surfaces are driven by a resonant RF magnetic field at low enough DC magnetic fields that mutual electron-^1H nuclear spin flips can occur in the surrounding solution [118, 119]. This results in enhanced ^1H signal from the water surrounding the ND, as shown in Figure 1.9(b) [112]. The ^1Hsignal enhancement is sensitive to ND concentration, as illustrated in Figure 1.9(c) [112]. After optimizing the experiment conditions to achieve high contrast OMRI images enhanced with NDs, a phantom is imaged, as illustrated in Figure 1.9(d) [112]. This phantom consisted of glass vials filled with 500μl of either pure DI water or aqueous solutions of HPHT ND (125nm at 100mg/ml). A high contrast OMRI image of diamond-shaped pattern in the vials was observed, as shown in Figure 1.9(e) [112], which shows high-contrast signal enhancement only where ND is present. Furthermore, they demonstrated that the OMRI technique can produce grey-level images using different ND concentrations, as shown in Figure 1.9(f and g) [112].

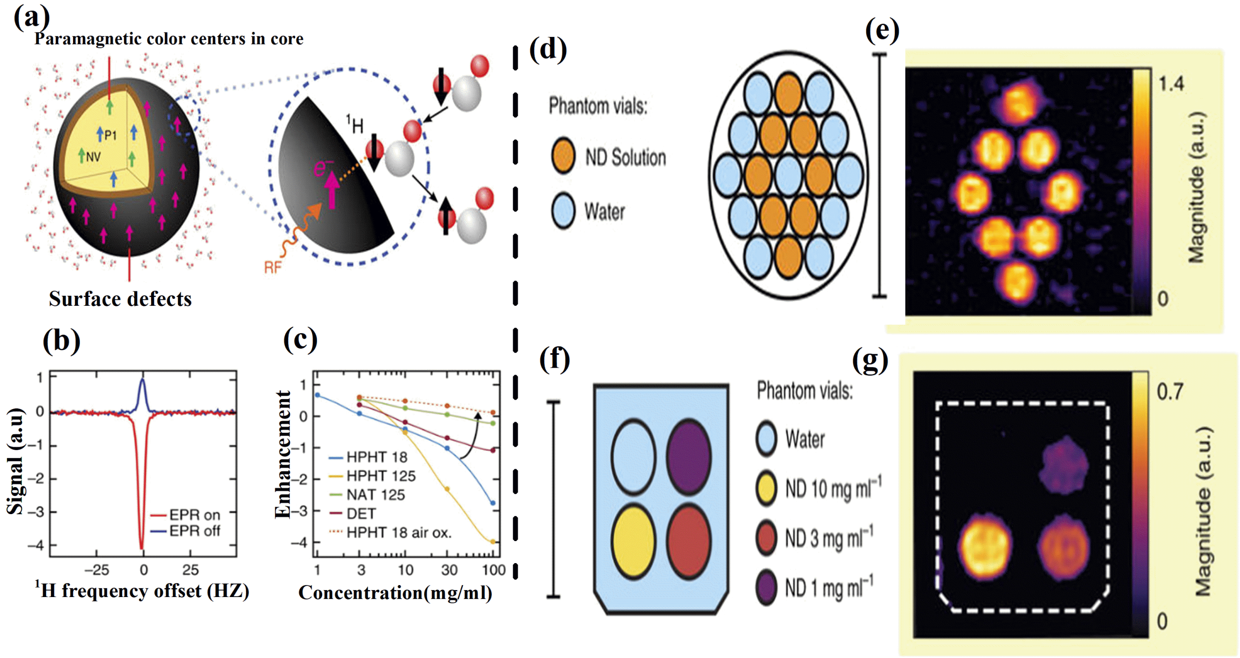

Figure 1.9: (a) An illustration of the Overhauser effect at the ND-water interface. (b) Overhauser enhancement of ^1H polarization in a HPHT 125nm (100mg/ml) ND solution (red). While the thermal hyperpolarized ^1H spectrum is (blue). (c) Overhauser enhancement of ^1H polarization as a function of NDs concentration at 6 mT. (d) Vials of DI water (blue) and vials of HPHT 125nm ND at 100mg/ml (orange) were arranged in a pattern in an imaging phantom. (e) High contrast OMRI image with high signal to noise ratio from only the vials where NDs are present. (f) Imaging phantom prepared with vials with different concentration of ND solutions. (g) ODMR contrast images that change as a function of the NDs concentrations. Reprinted with permission from[112]

Much stronger MRI contrast enhancement is possible in principle using NVs that are strongly spin polarized (up to 90%) [120] by optical excitation. This polarization can then be transferred to nearby nuclear spins like ^{13}C or ^{1}H [120, 121]. Recently, it has been shown that the ^{13}C in bulk diamond can be polarized to 0.054% at room temperature (45 fold enhancement) after 6 minutes of optical excitation of the NVs at a magnetic field of 0.3 T [120]. However, it has also been reported [120,121] that the relaxation time of hyperpolarized nuclei is much shorter for submicron particles [109, 112, 122]. Nonetheless, it has been shown that high contrast MRI images can be produced from spin polarized ^{13}C owing to the lack of background ^{13}C signals [123]. Finally, at cryogenic temperatures, dynamic nuclear polarization (DNP) of the ^{13}C nuclei can boost the small nuclear spin polarization by 10,000 times [122, 124, 125][127, 129, 130]. However, these temperatures are not suitable for in-vivo work.

Efforts have been made to overcome the short relaxation time of nanodiamonds at room temperature by functionalizing the surface of the NDs with paramagnetic Gd(III) chelates to create complexes for imaging with conventional T1-weighted MRI[115]. However, this alternative solution encountered a large background signal, and concerns of the long-term toxicity of gadolinium-based compounds cancels the advantage of non-toxic nanodiamonds [111].

1.1.1.8 New color centers in diamonds

Fluorescent nanodiamonds that have absorption and emission bands located within the biological transparency window are in particular interest for biological applications as illustrated in Figure 1.10(a) [37, 74, 79, 86, 126] . There are several color centers in nanodiamonds that can be called NIR centers. For example, in addition to nitrogen-vacancy (NV) [37, 86], silicon-vacancy (SiV) [127,128], tin-vacancy (SnV) [41] , Nickel-vacancy (NiV) [129,130], and marginally Germanium-vacancy (GeV) [131].

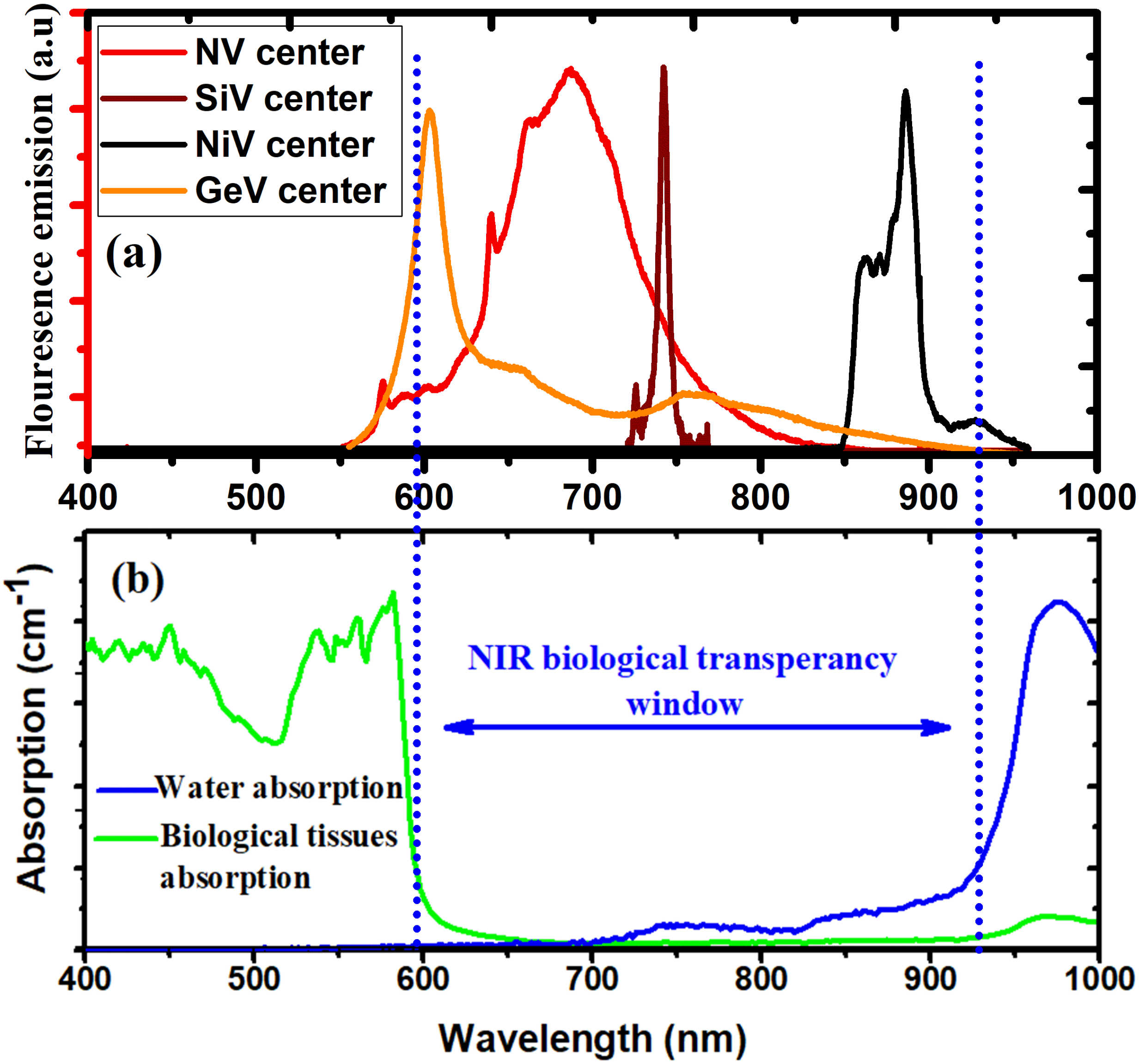

Figure 1.10: (a) Superimposed photoluminescence spectra of color centers in nanodiamonds (FNDs) namely; germanium-vacancy, nitrogen-vacancy, silicon-vacancy, and nickel-vacancy. (b) The fluorescence spectra of all diamond color centers in (a) fit within the biological transparency window. The black, dark gray, and light gray curves are the absorption spectra of H2O, oxygen-bound hemoglobin (HbO2), and hemoglobin (Hb), respectively.

As stated above, the emission of the NV center is perfectly located within the biological transparency window as shown in Figure 1.10(a and b) [70]. However, the maximum of the absorption band (480-600 nm) of the NV color center overlaps with the biological tissues absorption band resulting in autofluorescence background [132, 133]. To overcome this drawback, recent reports have shown that the excitation bands of NV- centers in certain micro and nanodiamonds can be extended to the zero-phonon wavelength of 638nm and possibly beyond, which is in the region of suppressed autofluorescence of the biological tissue [99, 133]. This is a step forward to make NV centers more biocompatible for biological applications.

The silicon vacancy defect in diamond consists of a silicon atom is a split vacancy. It has both emission and absorption bands in the NIR spectral window. The photoluminescence (PL) of SiV displays a large spread of emission wavelengths (between 730 and 750 nm) but most of the emission lies within a fairly sharp zero-phonon line (ZPL) centered at around 738 nm as shown in Figure 1.10(a) [39].The optical excitation wavelength for the SiV color center can be easily selected within the NIR window [39] or in the visible. Notably, the SiV color center was reported as a stable fluorescent marker in a ultra-small (1.2nm) nanodiamond crystals [127]. The nickel color center (Ni) in diamond is a substitutional Ni site in the diamond lattice which may also include a split vacancy. It possesses a strong photoluminescence (PL) doublet around 883/885nm as shown in Figure 1.10(a) [129, 130] which is attributed to ground state splitting caused by the spin orbital interaction. Ni also has a biocompatible excitation range (650-800nm) which makes it an excellent candidate for biological imaging and sensing applications.

Tin-vacancy (SnV) color center in diamond has been recently discovered [41]. Like the SiV, the tin atom sits on an interstitial site with two neighboring vacancies in diamond crystal. It has been incorporated into diamond via ion implantation and subsequent high-temperature annealing. The SnV center exhibits a sharp zero phonon line at 619 nm at room temperature and then this line splits into into four peaks at cryogenic temperatures due to a larger ground state splitting (850 GHZ). Furthermore, the excitation and emission of the SnV color center are located with the biological transparency window [41].

Germanium-vacancy (GeV) is a color center in diamonds, composed of a germanium (Ge) and a vacancy (V) [131] with a structure like the SiV. GeV exhibits a marginally biocompatible photoluminescence band (595-610nm) with most of the emission concentrated in a zero-phonon line at 602nm at room temperature [131]. The excitation wavelengths of GeV can be in green or red bands which make it a potential fluorescent marker in bio-imaging and biomedical applications.

In general elements heavier than Si, when implanted in diamond are expected to give split vacancy structure like the SiV [43]. Based on recent work with Ge and Sn, and more recently Mg, it is estimated that many of these centers will have narrow emission lines in the visible to near IR range and will thus allow multiplexing with other fluors, as desired.

In summary, due to the growing number of NIR and visible color centers in nanodiamonds, as so far only a fraction of the periodic table has been implanted into diamond [43], they promise to be excellent candidates for high contrast fluorescent markers, even deep inside biological tissues when excited with biocompatible wavelengths (635nm-800nm). It is important to know that most of the above mentioned color centers have still only been seen in bulk diamond and in relatively large nanodiamond crystals (>100nm). In order to produce ultrasmall nanodiamonds with stable color centers, nanodiamonds seeded growth is the solution. This growth technique will be discussed in detail in the following section.

In section 2, I will discuss growth of small and quality nanodiamonds (NDs) from a diamond-like organic molecule seed with precise control over the color center defects for bio-imaging and optical temperature sensing in biological applications. In this approach, the basic concept is basically a diamond-like organic molecule is used as a seed crystal and a high quality diamond is grown around it. The advantage is that the types and arrangement of atoms in the seed molecule determine the diamond color-centers. Under these conditions, growing NVs in the range of 2-10 nm or larger, depending on growth conditions, has been achieved [134]. However, further investigations on growth of fluorescent nanodiamonds (FNDs) using different organic seed molecules that are expected to give different color centers to confirm a successful seeded nanodiamonds growth are required. This makes a bottom-up engineering approach to fluorescent NV fabrication impractical. It is clear that by this technique the probabilistic nature of color centers fabrication is eliminated, and bottom-up growth of small, bright, and stable FNDs is made possible.

In section 3, I will show that the optical spectrum of the Ni complex is very sensitive to temperature near room temperature, and is therefore a good candidate for nano thermometry. I will also show that it is possible to excite the NV center with a more biocompatible wavelength (660 nm) where autofluorescence background, overheating, and photodamage are greatly minimized [135]. Since the NV and Ni measure temperature by different physical mechanisms, their simultaneous use can avoid confusion by other cell processes, as these would impact each temperature sensor differently [94].

1.1.2 Upconversion nanoparticles (UCNPs)

1.1.2.1 Overview

Upconverting luminescence idea was first discovered in a solid material by Bloembergen in 1959 [136]. Upconversion is a nonlinear optical process where near-infrared (NIR) light is absorbed sequentially to multiple excited states and emitted in ultraviolet-visible-NIR wavelengths. This interesting phenomena was then demonstrated in early experiments conducted by Auzel in 1973 and 1976 respectively [137, 138]. Rare-earth (RE) ions doped into a solid lattice host are ideal for upconverting process because they exhibit long lifetimes in their intermediate states which allow sequential excitations [139]. The long live times is attributed to the nature of partially forbidden f-f transitions and low phonon energies of host lattice which reduces multi-phonon relaxation of the RE ions [139, 140]. Upconversion materials have been widely used in manufacturing compact solid-state lasers, temperature sensors, and other applications [141]. In late 1990s, upconversion nanoparticles doped with lanthanide ions attracted special interest in biological applications [142–144] . Compared to conventional fluorescent markers such as organic dyes and QDs, upconversion nanoparticles (UCNPs) allow suppression of tissue autofluorescence and are therefore visible deep inside biological tissue. Furthermore, UCNPs have a lower pump intensity threshold, better photostability, and less toxicity [28].

1.1.2.2 Upconversion process in UCNPs

The most efficient upconversion process in rare-earth doped nanomaterials is energy transfer upconversion (ETU) in which sensitizer ions with large absorption cross-sections at near-infrared

(NIR) wavelengths sequentially transfer absorbed energy to emitter ion [140, 145, 146]. Upconversion luminescence in lanthanides can be interpreted based on three main mechanisms: Excited State Absorption (ESA), Energy Transfer Upconversion (ETU), and Photon Avalanche (PA) [139]. Here, we only consider ETU. For this we use ytterbium ion (Yb^{+3}) as a sensitizer and choose the erbium ion (Er^{+3}) as the activator (reaccepter) for two reasons: (i) Er^{+3} ions can efficiently create upconversion fluorescence in the visible and near-infrared, but their absorption at the 980 nm excitation wavelength is relatively weak as shown in Figure 1.11(a) [147], and (ii) the Yb^{+3} ion has a very high absorption cross section at 980 nm, and can efficiently transfer its excitation to Er^{+3} ion [139] using the ETU process as shown in Figure 1.11(b).

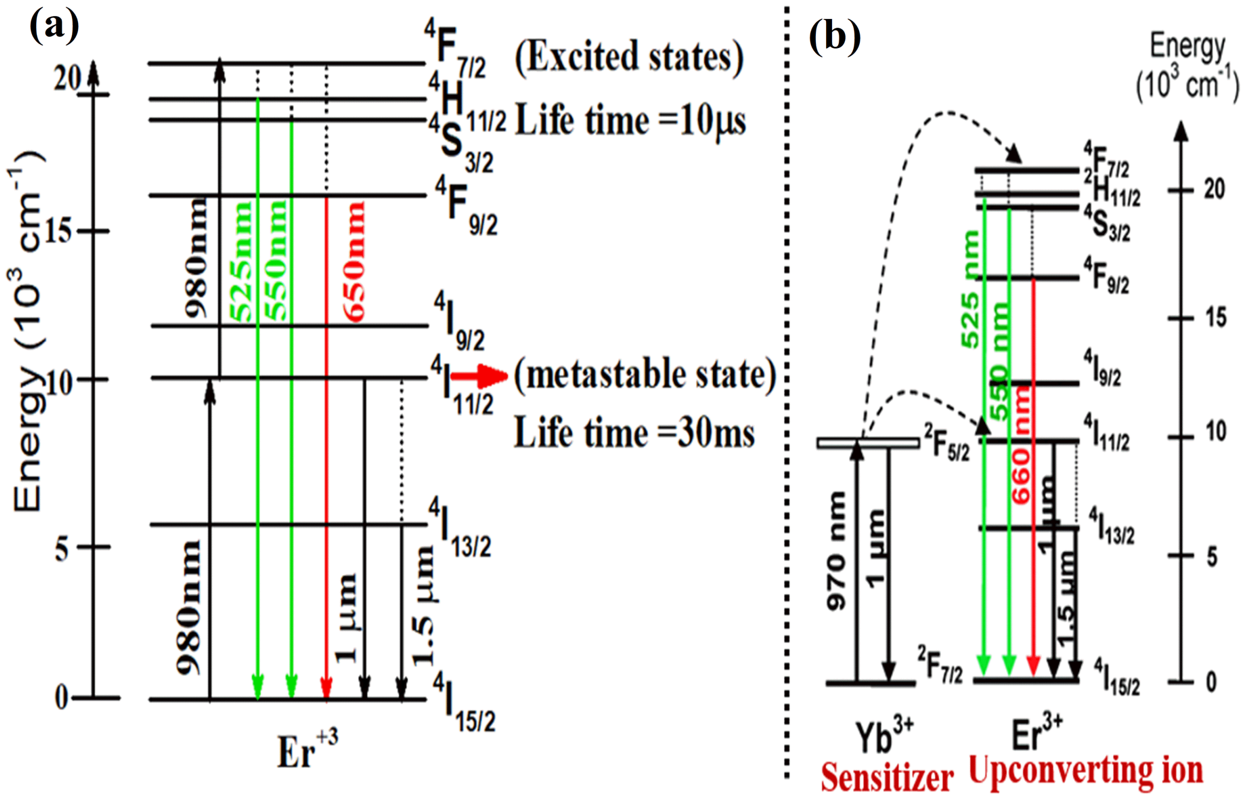

Figure 1.11: (a) Ucpconversion process in activator (Er^{+3}) only (b) Energy transfer mechanism between sensitizer (Er^{+3}) and activator (Yb^{+3}). Curved dashed, straight dashed and full arrows represent energy transfer, multi-phonon relaxation, and radiative emission process, respectively

The ETU between Yb^{+3} ions and Er^{+3} ions occurs according to the following transition:

$$({}^4I_{15/2}Er^{+3}) + ({}^2F_{5/2}Yb^{+3}) \longrightarrow ({}^4I_{11/2}Er^{+3}) + ({}^2F_{7/2}Yb^{+3}) \tag{1.1}$$

Consequently, as shown in Figure 1.11(a), the Yb^{+3} ion absorbs the first NIR photon of 980 nm laser to the (${}^2F_{5/2}$) Yb^{+3} excited state. The energy transfer from the (${}^2F_{5/2}$) Yb^{+3} excited state promotes $Er^{+3}$to its quasi-resonance metastable state${}^4I_{11/2}$. A second NIR photon absorption re-excites the Yb^{+3} back to the (${}^2F_{5/2}$) Yb^{+3} excited state and energy transfer further excites the Er^{+3} (${}^4I_{11/2}$) metastable state to a highly excited (${}^4F_{7/2}$) Er^{+3} state. This state then relaxes to (${}^2H_{11/2}$, ${}^4S_{3/2}$, and ${}^4F_{9/2}$) Er^{+3} states via the multi-phonon relaxations. Subsequent radiative transitions then occur to the ground state ${}^4I_{15/2}$ according to the transitions: ${}^2H_{11/2}\longrightarrow {}^4I_{15/2}$, ${}^4S_{3/2}\longrightarrow {}^4I_{15/2}$, and ${}^4F_{9/2} \longrightarrow {}^4I_{15/2}$, which give green (520 nm and 550 nm) and red (650 nm) emissions; respectively, as shown in Figure 1.11(b)) [148]. These upconversion processes can operate at lower pump laser intensities because they possess real long-lived intermediate states (lifetimes on the microsecond scale). Therefore, inexpensive low-power lasers (typically $1 - 10^3 W.cm^{-2}$) can be used for their excitation [139, 147, 149].

1.1.2.3 Application of UCNPs in biosensing and bioimaging

Rare earth doped upconversion nanoparticles (UCNPs) have been successfully implemented in biological imaging at the cell level, and in the tissues of small animals like mice. UCNPs can also be used for single-particle imaging due to their UCNP's brightness even after long-time continuous laser illumination [150–152]. Also UCNPs have demonstrated optical temperature sensing in living cells with high temperature resolution of about 0.2-0.5K [15, 153–156].

1.1.2.4 Commonly used UCNPs

Upconversion nanoparticles of $\beta - NaYF_4 : Yb^{+3}, Er^{+3}$ and $\beta - NaGdF_4 : Yb^{+3}, Er^{+3}$ have been reported as one of the most efficient UCNPs with strong up-conversion luminescence (UCL). However, they work optimally in organic solvents such as cyclohexane and their UCL drops significantly when dispersed in water [157] (at least for small particle sizes). Specifically, the standard upconversion nanoparticles $NaYF_4 : Yb^{+3}, Er^{+3}$ quantum yield is 3% in bulk particles at 980 nm illumination. However, this quantum efficiency drops to 0.005% at 980 nm illumination for 10 nm particle size dispersed in hexane, and 0% at the same size (10 nm) when dispersed in water [158, 159]. Therefore, the commonly used $NaYF_4 : Yb^{+3}, Er^{+3}$ nanoparticles are not favorable in many bioimaging applications since water is present in most biological tissues.

Recently, water tolerant upconversion nanoparticles $YVO_4 : Er^{+3}, Yb^{+3}$ have been proposed. Their quantum efficiency is 1.3% at 980 nm illumination for 10 nm particle size [148]. The only disadvantage of $YVO_4 : Er^{+3}, Yb^{+3}$ nanoparticles is higher saturation laser power, However, even for illumination of only 550 $W.cm^{-2}$ the quantum yield is 0.1% for 10 nm particle size in water [148] which is still higher than the best quantum yield for $NaYF_4 : Yb^{+3}, Er^{+3}$ nanoparticles at the same size in hexane. So $YVO_4 : Er^{+3}, Yb^{+3}$ nanoparticles are considered to be the best solution for water-based bio-application compared to the commonly used $NaYF_4 : Yb^{+3}, Er^{+3}$ nanoparticles.

It is known that the efficiency of upconversion nanoparticles can be significantly influenced by the quality of the host materials; therefore, it is important to select host crystals that maintain excellent optical properties and chemical stability in water, even down to the single particle level such as YVO_4 particles [160, 161].

In section 4, I synthesized $YVO_4 : Er^{+3}, Yb^{+3}$ nanoparticles following the procedure in [148, 162], with an estimated size range of 30-40 nm for high contrast imaging in biological models. These nanoparticles were injected into fire ants in order to observe the upconversion luminescence emission efficiency of $YVO_4 : Er^{+3}, Yb^{+3}$ nanoparticles inside an ant's body using a relatively low excitation intensity of 10 $kW.cm^{-2}$at 980 nm in a homemade wide-field setup. I was able to clearly detect the upconversion luminescence emission of $YVO_4 : Er^{+3}, Yb^{+3}$ nanoparticles from inside the body of the ants. This is attributed to the low autofluoresence background, non-photobleaching, and non-blinking observed when using $YVO_4 : Er^{+3}, Yb^{+3}$ nanoparticles.

1.1.2.5 Upconversion nanoparticles in Core/shell structure

Typically, UCNPs doped with lanthanide ions, use Ytterbium (Yb^{+3}) as a sensitizer due its infrared large absorption cross section to ensure high upconversion efficiency of upconverting ions such as Ln^{+3} (Ln=Er,Tm,Ho,etc.) [29, 163]. Unfortunately, the conventional UCNPs-sensitizer (Yb^{+3}) has only one absorption band centered at 980 nm wavelength which largely overlaps with the absorption band of water molecules that are dominant in biological samples as shown in Figure 1.12. Therefore, triggering the upconversion process in UCNPs with 980 nm laser excitation would significantly cause overheating issues that might result in cell death, tissue damage, and inaccurate thermal reading during temperature sensing [164].

Interestingly, Neodymium (Nd^{+3}) has shown high efficiency energy transfer to (Yb^{+3}) in addition to a large absorption cross section at 808 nm where the water absorption is too low compared to the water absorption at 980 nm [165] . However, the introduction of (Nd^{+3})as new sensitizer directly into UCNPs nanoparticles quenches their upconversion luminescence dramatically due to the deleterious energy transfer (ET) between the new sensitizer (Nd^{+3}) and the activator (Er^{+3}), respectively [29].

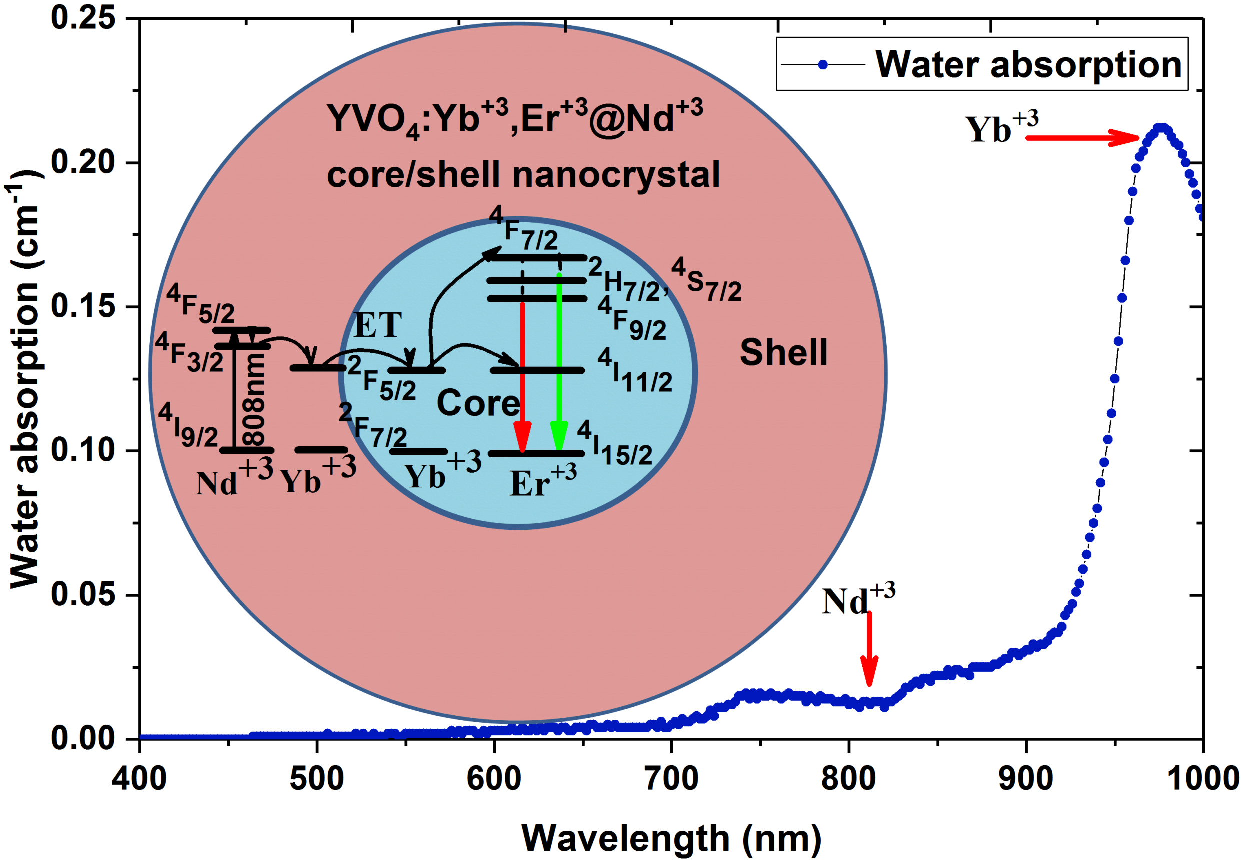

Figure 1.12: An absorption spectrum of distilled water (DI water) taken over the visible and the near-infrared (NIR) range. The blue arrows indicate the lower and higher water absorption bands, where the alternative excitation bands should be extended to avoid biological tissues overheating by introducing Nd^{+3}as a new sensitizer into the UCNPs instead of the conventional sensitizer (Yb^{+3}) of the UCNPs. Inset: Schematic design and energy transfer processes between Nd^{+3} , Yb^{+3}, and Er^{+3} of a core/shell nanoparticles (photon upconversion) under 808 nm laser excitation. Reprinted with permission from [167].

To overcome this issue, an engineering core/shell structure is necessary where the new sensitizer (Nd^{+3}) is doped with the (Yb^{+3}) in the shell and the activator (Er^{+3}) is doped with (Yb^{+3})in the core to avoid such ET processes [166] as shown in Figure 1.12 [167]. The upconversion process in the new core/shell combination occurs when the new sensitizer (Nd^{+3})ion absorbs NIR photons and transfers energy to the nearby Ytterbium (Yb^{+3}) ion; and then Yb^{+3} ion transfers the NIR photons to the activator (Er^{+3}) ion, where the UC process is expected to take place. Specifically, the most commonly used $NaYF_4 : Yb^{+3}, Er^{+3}@Nd^{+3}$ UCNPs were synthesized in a core/shell structure and showed to be the best UCNPs generation for biological imaging and thermometry. However, these UCNPs suffer from very low quantum efficiency when dispersed in water, especially at small particle sizes as reported in [29, 153, 164]. Recently, $YVO_4 : Yb^{+3}, Er^{+3}$ UCNPs have shown relatively good quantum efficiency at the single-particle level when dispersed in water [148] as well as high contrast imaging in biological models [28].

In section 5, I introduced Nd^{+3} into $YVO_4 : Yb^{+3}, Er^{+3}$ UCNPs in a core/shell structure, which provide efficient luminescent markers at a biocompatible illumination wavelength for optical temperature sensing in living organisms. we synthesized water tolerant $YVO_4 : Yb^{+3}, Er^{+3}@Nd^{+3}$ core/shell nanoparticles (average size 20 nm) with strong UC luminescence at a biocompatible excitation wavelength for optical temperature sensing where overheating in water is minimized.

In section 6, as an application of FNDs and UCNPs, I investigated their use as nano-thermometer inside bovine embryos. The motivation for using both FNDs and UCNPs to measure temperature is to avoid the question of sensor confusion by the local cellular environment. Specifically, by simultaneously measuring temperature using two different modalities having different physics, it is possible to greatly improve the measurement confidence, thereby directly addressing the recent controversy surrounding temperature measurements in living organisms.

2. ENGINEERING SEEDED GROWTH OF FLUORESCENT NANODIAMONDS

2.1 Introduction

Commercial nanodiamonds are fabricated by two main techniques: 1) crushing larger diamonds [168]. 2) detonation of explosives [169]. In addition, nanodiamonds are fabricated by non-detonation shock wave techniques such as laser ablation [170] and ultrasound [171]. There is also research in direct growth of nanodiamonds via chemical vapor deposition (CVD) [172], and in flowing plasma [173], plus numerous other techniques. However none of the existing nanodiamond fabrication techniques produces material that is close to the quality of bulk diamond, and this often leads to photostability problems for sizes less than 10 nm, and sensitivity problems for NV centers [57].

Recently, in an attempt to overcome the limitations of ultrasmall nanodiamonds direct growth starting from organic precursors has been performed at high-pressure high-temperature (HPHT) > 900^oC, [174, 175] using techniques developed a long time ago [176]. So far FNDs with NV and SiV color centers have been grown by these techniques. In addition, researchers have also been attempting to grow high-quality nanodiamonds around diamondoid seed molecules for more than a decade using chemical vapor deposition (CVD) techniques. The motivation is that a diamondoid molecule is already like an ultrasmall diamond without defects, so that growing around a diamondoid seed molecule should give much higher quality nanodiamonds. Such seeded growth has successfully been applied to enhance nucleation of nanodiamonds for the growth of superior nanocrystal CVD diamond films [177–179]. Recently, the growth temperature has been reduced to well below the diamondoid decomposition temperature [178] in the hopes of improving yield (fraction of diamondoids producing diamonds). However, the yield is still extremely small (i.e. isolated nanodiamonds separated by microns compared to self-assembled seed layers with sub-nanometer separations).

Other work has shown that easily cracked isobutene molecules can serve as a source of reactive carbon in the synthesis of larger diamondoids from smaller ones [180], which presumably is a key intermediate step in the growth of nanodiamonds. This same work attempted seeded nanodiamond growth via CVD at a temperature below the seed decomposition temperature and observed enhanced nanodiamond films, but again with a relatively small yield. Finally, larger diamondoids have also been grown from smaller ones in xenon plasma, again with a rapidly decreasing yield as diamondoid order increases [181].

In addition to higher quality nanodiamonds, the diamondoid molecule seeding approach has the potential to deterministically produce color centers so that every nanodiamond, no matter how small, can have one or more bright fluorescent emitter [134]. This overcomes the limitation of all existing fabrication techniques including growth and post-implantation which are inherently probabilistic in nature. Thus, instead of treating color center creation in nanodiamonds as a crystal growth or processing problem, it can be approached as a chemistry problem for seed molecule synthesis. This approach is illustrated in Figure 2.1. Here, the first step is to synthesize a molecule that will act as a precursor (or seed) for specific color centers [134]. A diamond will be grown around this molecule in a non-destructive way so that the resulting nanodiamond (or micro-diamond) can have a completely independent chemical and isotopic composition from the seed molecule, yet still be a single crystal.

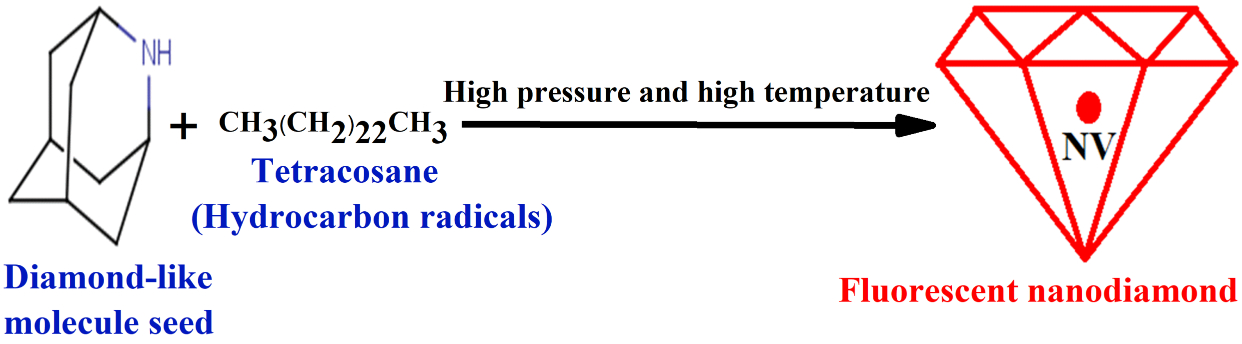

Figure 2.1: An illustration of the concept of seeded growth of fluorescent nanodiamonds. A diamond-like organic molecule seed is used to produce fluorescentnanodiamonds. Carbon radicals (such as tetracosane) are then created by cracking a hydrocarbon that decomposes at a much lower temperature than the diamondoid seed molecule. The final product of the growth gives nanodiamond with desired color center.

This technique could be extended to other color centers. For example, a diamondoid seed with a single silicon atom could in principle form a 2 nm SiV nanodiamond which reproduces the properties of the meteor diamonds (i.e. a photostable fluorescent diamond that is smaller than many protein based dyes) [127]. Also, more complex color centers may be possible. For example, one of the best diamond emitters consists of a nickel atom surrounded by 4 nitrogen atoms (NE8 center) [182]. It has strong narrowband emission in the tissue transparency window. This color center is not favored by probabilistic growth, but could in principle be grown with high yield by using the appropriate seed molecule. Seeded growth of nanodianonds approach has produced small and high quality nanodiamonds [134]. However, more experiments are required to produce the same quality of nanodiamonds grown from different seeds that are expected to give completely different color centers. In this chapter, I performed different experiments to confirm success of the seeded growth approach. In particular, I observed two different color centers in nanodiamonds grown from two different diamond-like organic seed molecules. Furthermore, I observed no nanodiamonds in the absence of diamond-like seed in a control experiment. These result confirm a successful nanodiamond seeded growth approach.

2.2 Experimental apparatus and methods

2.2.1 Diamond anvil cell (DAC)

One of the most common apparatus to produce diamond is diamond anvil cell (DAC). DAC consist of piston-cylinder diamond anvil cell, diamond anvils, screws to apply force, gasket, and small cylindrical seats for diamond anvils. In this work, we designed a home-built accessible piston-cylinder diamond anvil cell as shown in Figure 2.2(a). This DAC was made of Inconel 718 alloy material which is proven to work at high temperature (around 900^oC). To insure accurate alignment of the diamond anvils, the tolerance between piston and cell pore should be less than 25 microns. Force is applied in this DAC using six screws made of Inconel 718 alloy to generate a high pressure depending on the area of diamond anvil culet. The anvil culet is the flattened tip of the diamond anvil which experiences the greatest applied pressure.

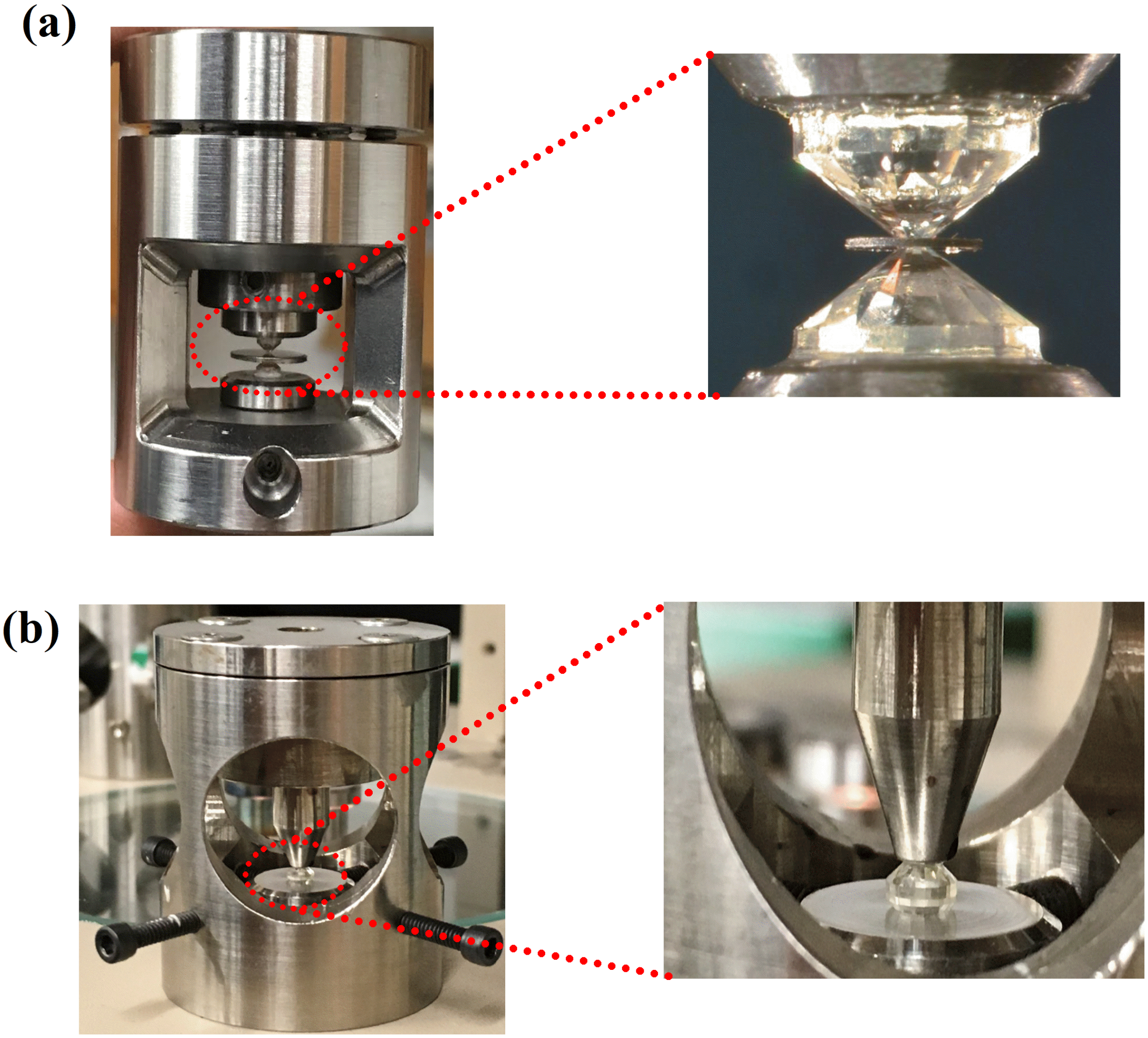

Figure 2.2: (a) Open design diamond anvil cell for high pressure and high temperature nanodiamonds growth. (a,inset) a zoomed image of gasket placed between two diamond anvils. The diamond anvils sit on top of a cylindrical seat. (b) A jig that is used to align and glue the pair of diamond anvils on their seats.

The diamond anvils sit on small cylindrical seats made of the same material as the DAC as shown in Figure 2.2(a, inset). These seats have a 1 mm conical hole with small angles (25-30 degree) to allow optical access to the sample and improve imaging and light collecting. To align the diamond anvils on top of the seats, we also designed a home-made jig to align and glue the anvils on their seats as shown in Figure 2.2(b).

2.2.2 Gasket

Gasket is one of the most important parts of the diamond anvil cell. It is a metallic foil (Inconel, rhenium, etc.) that sits between the two diamond anvils and keeps the sample contained when it is compressed between the anvils to give high pressure as illustrated in Figure 2.2(a,inset). For this experiment, gasket was made of inconel 718 alloy material with thickness (250μm). The gasket was pre-indented to a thickness equal to 1/9 of the diamond culet diameter before drilling a sample chamber hole. For gasket pre-indentation, we place it between the two diamond anvils after a careful alignment of the diamonds anvils in the DAC to make sure the culets are exactly opposing. Then, an appropriate pressure was applied during pre-indentation process to reach the desired thickness of the gasket. The pre-indentation pressure should be very close to the pressure that will be applied during growth to avoid unwanted deforming of the sample chamber under high pressure.

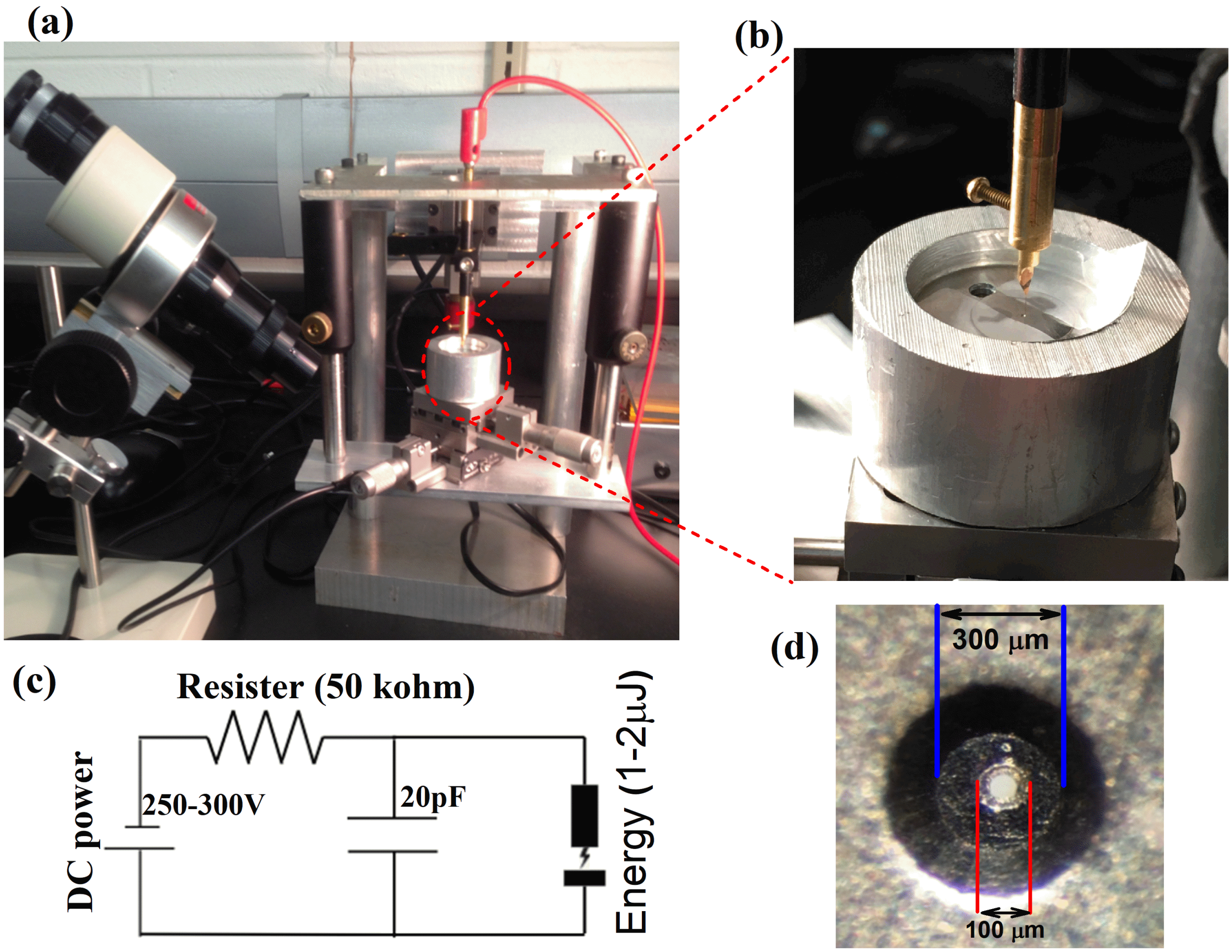

Figure 2.3: (a) A home-built micro- electrical discharge machine (EDM) which consist of drilling wire tool, dielectric fluid cup, x-y translation stage, and a small microscope for monitoring gasket drilling. (b) A magnified image of the dielectric fluid cup where the gasket can be placed for drilling sample chamber. (c) A small electrical circuit to derive the EDM. (d) An optical image of a pre-indented and drilled gasket.

Next, after gasket pre-indentation, a sample chamber hole need to be drilled in the middle of the gasket. The hole should be 1/3 of the diamond anvil culet (300 μm). So, to drill such a small hole, there are several drilling methods including laser cutting and electrical discharge machine (EDM). For our experiments, we designed a home-built micro-electrical discharge machine (EDM) as shown in Figure 2.3(a). We also made a small circuit to run the micro-EDM as shown in Figure 2.3(b). This circuit consist of a DC power supply that gives (200-250V), capacitor (20μF), and resister (50khom). The discharge energy that of this micro-EDM is few micro joule. Using this micro-EDM a 100 microns size hole was drilled using a 100 μm tungsten wire as shown in Figure 2.3(c). After drilling process, the gasket was then washed thoroughly using (acetone/methanol) in 30min sonication to remove remaining materials before sample loading.

2.2.3 High temperature furnace

In HPHT nanodiamonds growth, high pressure is provided by diamond anvil cells, however high temperature will be produced by a furnace. For this purpose, we designed a home-made furnace operating at high temperature up to 1000^oC as shown in Figure 2.4(a). This oven is made of cylindrical stainless-steel cup. We made an aluminum oxide layer inside the furnace for high temperature isolation. A tungsten wire was then wrapped between two thermally conductive boron nitrite layers where the diamond anvil cell will be inserted for nanodiamonds growth experiments. The furnace is connected to a variac power supply to provide an appropriate power for heating. For monitoring temperature inside the furnace during growth, a thermo-coupler attached directly to the diamond anvil cell inside the furnace as illustrated in Figure 2.4(b). The temperature displays on a K-type digital thermometer with precision equal to $\pm 0.1^oC$.

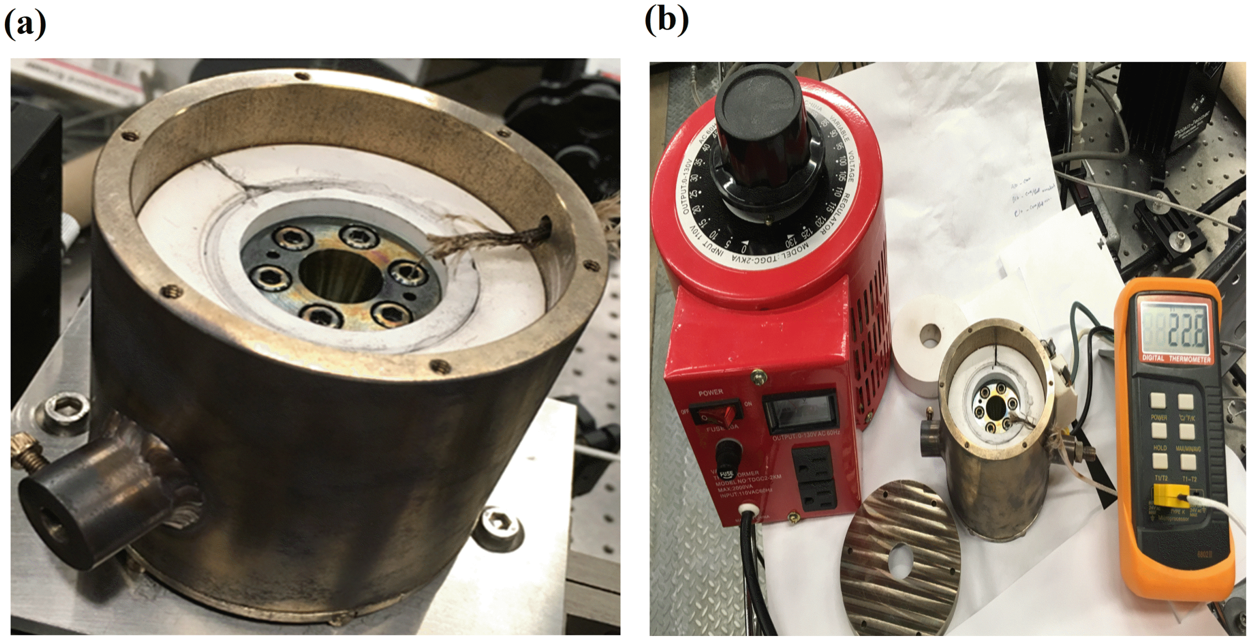

Figure 2.4: (a) A home-made high temperature furnace used for nanodiamonds growth. This furnace provides temperature up to 1000^oC. (b) A variac power supply connected to the furnace to provide the needed heat and digital thermometer for temperature monitoring inside the DAC during growth.

2.2.4 Optical setup for pressure and nanodiamonds growth monitoring

Several years before 1972, monitoring pressure inside diamond anvil cells was one of the big challenges due lack of precise and small pressure sensors [183]. Because the interior of diamond anvil cell is optically accessible, the pressure-dependent fluorescences of many materials was considered as a pressure sensor. In 1972, a ruby crystal ($Al_2O_3 : Cr^{+3}$) was found to have a sharp and strong fluorescence emission that linearly depends on the pressure [184]. The ruby crystal can be conveniently excited by a green laser (532nm) that promotes Cr^{+3} from the ground state to an excited state from which it decays non-radiatively to a metastable state, and then emits a sharp and strong fluorescent light at 694.20nm as shown in Figure 2.5(a). After this great invention, it was easy to precisely monitor the applied pressure inside a diamond anvil cell using optical excitation. In our experiments, we use a very small chip of ruby crystal which fill just only a small fraction of the sample chamber volume and provide a rapid and accurate pressure monitoring. Figure 2.5(b and c) show ruby fluorescence at ambient pressure plus the change of ruby crystal fluorescence as a function of applied pressure inside the diamond anvil cell.

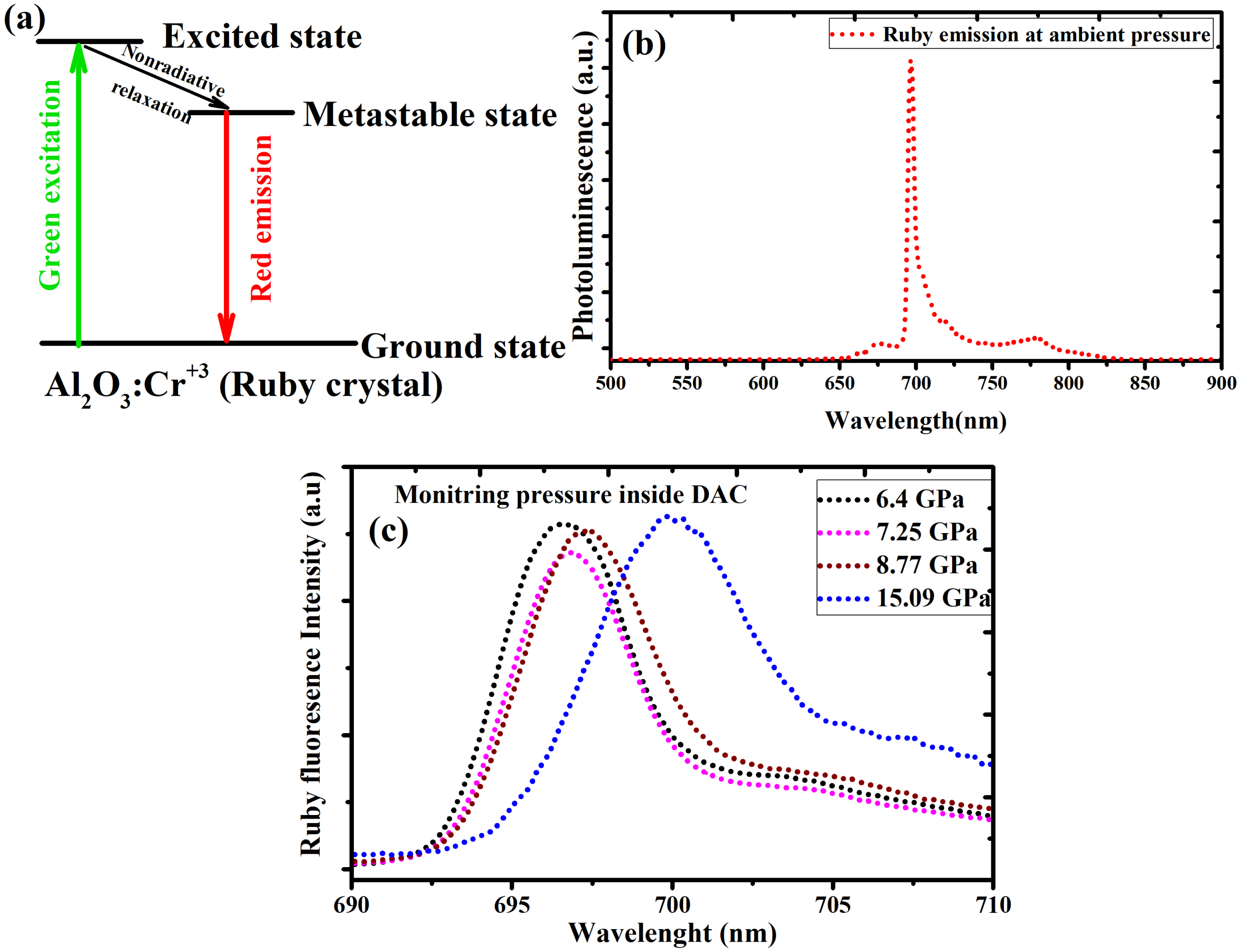

Figure 2.5: (a) An illustration of optical pumping and emission and the electronic structure of ruby crystal ($Al_2O_3 : Cr^{+3}$) showing the ground ,metastable, and excited states. (b) Optical emission of ruby crystal peaked at 694.20 nm under ambient pressure. (c) Optical emission spectra of ruby crystal changes as a function of applied pressure inside diamond anvil cell.

To optically monitor pressure and nanodiamond growth inside the diamond anvils cell, we designed a custom built optical microscope setup. This optical setup is equipped with a long working distance microscope objective (Mitutoyo 10x, working distance = 4.5mm), 4f imaging system, CCD camera for live imaging, and spectrometer as shown in Figure 2.6(a and b). Ruby fluorescence and the Raman emission of nanodiamond precursor materials were collected and analyzed using a home-made spectrometer. The spectrometer consist of visible-near infrared (NIR) grating and 4f imaging system, and a pinhole (100μm) imaged through 4f imaging system onto a CCD camera (Trius camera model SX-674).

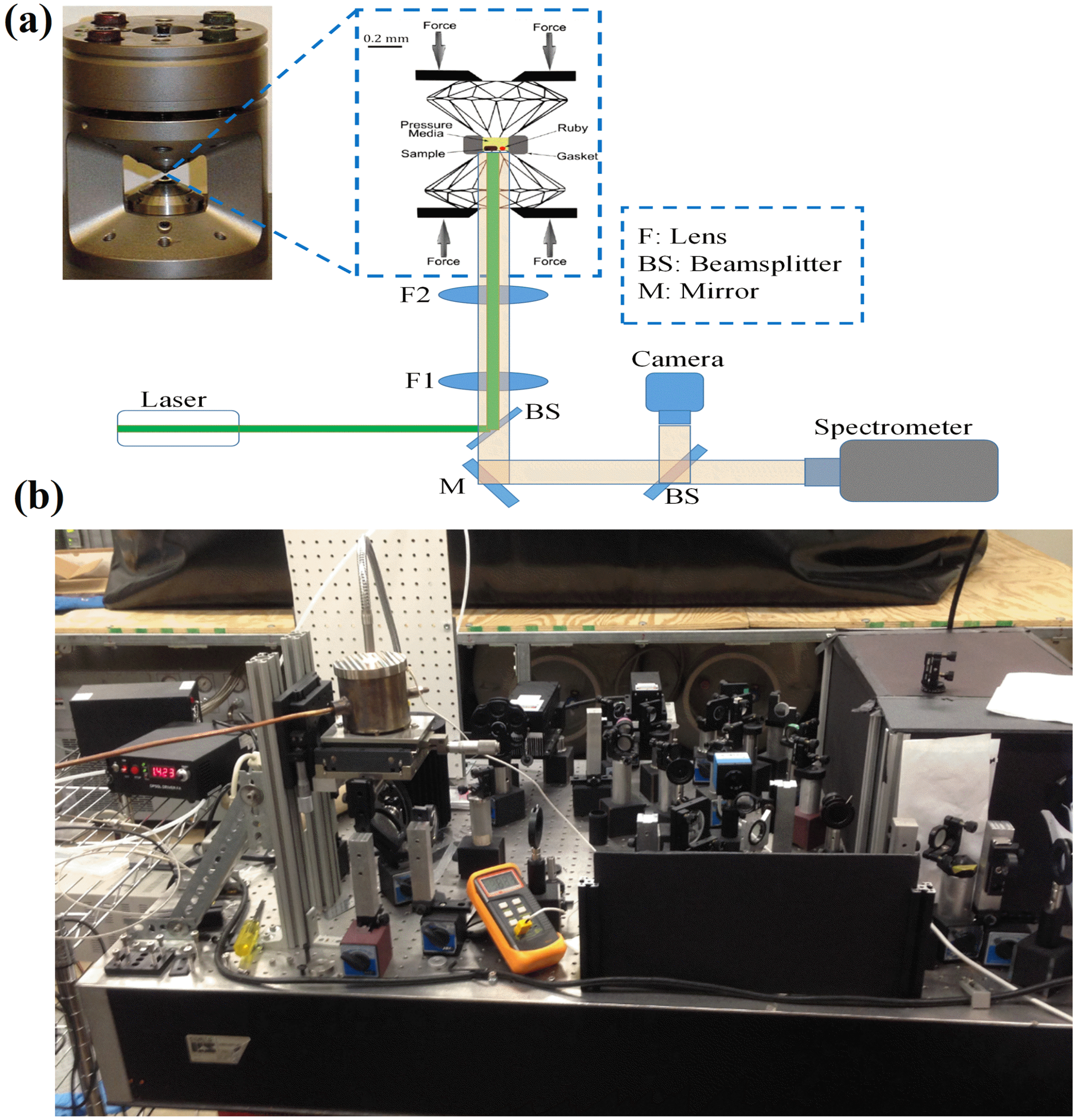

Figure 2.6: (a) A home-built optical microscope consist of 4f imaging system, lasers, monitoring CCD camera, and spectrometer. (b) An optical image of the optical setup showing all lasers and optical elements.

2.2.5 Sample preparation

In order to prepare growth materials for seeded nanodiamond growth experiments, hydrocarbons materials such as heptamethylnonane $((CH_3)_3CCH_2CH(CH_3)CH_2C(CH_3)_2CH_2C(CH_3)_3$, Sigma Aldrich > 98%) and tetracosane $((CH_3(CH_2)_{22}CH_3)$, Sigma Aldrich > 98%) were purchased to serve as a carbon source that cracks at low temperature to supply the carbon needed to grow diamond around the diamond-like organic seed molecules. In this work, several seed molecules were either purchased or synthesized in our lab or collaborators'lab. These include adamantine (Sigma Aldrich > 98%), 2-Azaadamantane hydrochloride (AURUM Pharmatech LLC >90%), Tetrakis(trimethylsilyl)silane (Sigma Aldrich > 98%), 5,7-dimethyl-1,3-diazaadamantane and 1-azaadamantan-4-one-2,2-13C_2

After many experimental trails we found a very good recipe to mix all the growth material and to suppress the formation of graphite and diamond-like carbon during growth. This is important because these unwanted by-products generate intense fluorescence that makes it impossible to monitor growth at critical stages.

The mixture recipe consists mainly of the organic seed molecule (20μl) + Heptamethylnonane (200μl) + Tetracosane(2ml) + Tetramethylhydrazine(10μl). In addition, to dissolve the organic seed molecule, either chlorobenzene or dichloromethane is initially used first. Second, the mixture of hydrocarbons (heptamethylnonane and tetracosane) is combined with the organic seed molecule solution. The mixture is then heated up to the melting point of tetracosane to insure thorough mixing. Next, the tetramethylhydrazine was introduced into the mixture, whose purpose was to prevent graphite formation during growth as mentioned above. Finally, we cool the mixture to room temperature so as to have solid material that can be easily loaded into the sample chamber of the diamond anvil cell.

2.3 Results and discussion

We conducted five experiments to verify that the nanodiamond seeded growth approach is feasible. Different nanodiamond growth experiments at different conditions are presented in Table

2.1.

Experiments	**Hydrocarbon radicals**	**Seed**
Experiment 1	Heptamethylnonane and tetracosane	2-Azaadamantane hydrochloride
Experiment 2	Heptamethylnonane and tetracosane	5,7-dimethyl-1,3-diazaadamantane
Experiment 3	Heptamethylnonane and tetracosane	2-Azaadamantane hydrochloride
Experiment 4	Heptamethylnonane and tetracosane	No seed (control)
Experiment 5	Heptamethylnonane and tetracosane	poly(1-vinyladamantane)

Table 2.1: A summary of five samples (hydrocarbon radicals and seeds) prepared for nanodiamond seeded growth experiments

2.3.1 Experiment 1

In the first experiment, after building new diamond growth apparatus in our laboratory, it was very important to verify that we can produce nanodiamonds at high pressure and high temperature. For this purpose, we mixed 2-Azaadamantane hydrochloride as a seed with hydrocarbons radicals (heptamethylnonane and tetracosane) following our recipe mentioned above in the sample preparation section. There was no tetramethylhydrazine in the growth mixture in this experiment. The sample was then transferred into a 100μm sample chamber (gasket) placed between two diamond anvils in the diamond anvil cell and pressed under high pressure up to 20 GPa. The sample was heated to high temperature up to 550^oC in the heating furnace for three hours under a continuous flow of a forming gas (98 % Ar and 2% H_2) to prevent diamond anvils graphitization. Next, the sample was then extracted from the diamond anvil cell after growth by a needle with a 2μm tip (American Probe Technologies, Inc.). To insure a successful transfer of nanodiamonds from growth chamber, we dip the tip of the extraction needle into 200μl of an isopropanol/ethanol solution, repeating several times until the growth chamber is emptied. For TEM and optical characterization a few drops of the nanodiamond solution was placed on a lacy carbon TEM grid and quartz slides respectively.

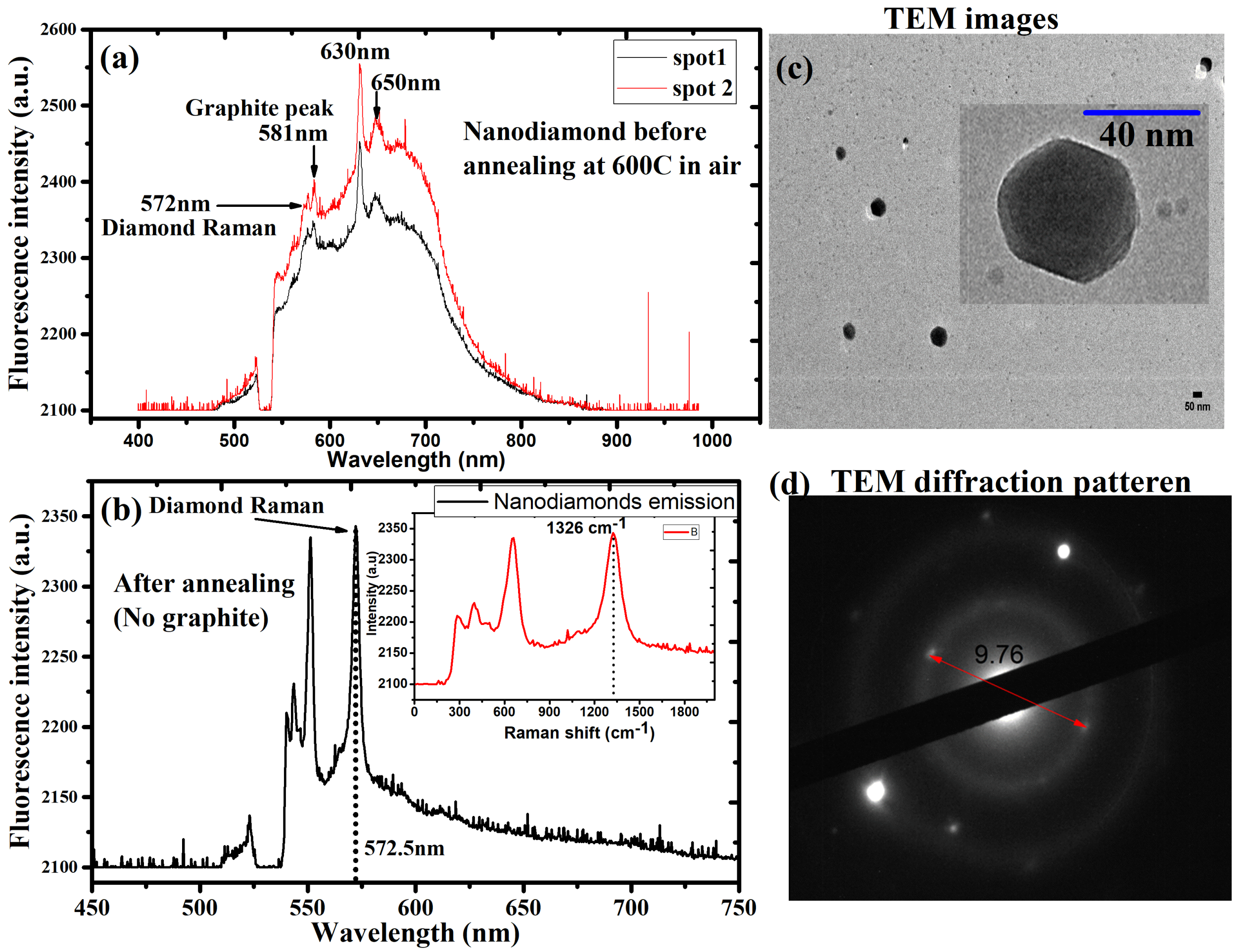

Figure 2.7: (a) An optical spectrum of grown nanodiamonds before post cleaning or annealing. It shows a dominant autofluresence background plus a small nanodiamonds Raman peak at 572nm, clear D and G peaks at 575nm and 581nm respectively, and 630nm peak that has been reported as unknown defect in nanodiamonds with bad surfaces. (b) An optical spectrum of the same nanodiamonds after annealing in air at $700^{o}C$ to remove graphite and other impurities. It shows a clear nanodiamonds Raman peak at 572.5nm and the right Raman shift of diamonds at $1326cm^{-1}$ as illustrated in (b.inset). (c) low and high magnification TEM images of produced nanodiamonds which reveal well dispersed and round shape nanodiamonds crystals. (d) TEM diffraction pattern of individual nanodiamonds which shows the correct diamond (111) lattice plane spacing ($2.06^{o}A$).

Optical characterization revealed an optical spectrum as shown in Figure 2.7(a) with several peaks. One corresponds to the Raman peak of nanodiamonds at 572.5nm, another to the D-peak at 575nm, another to the graphite peak at 581nm, and also a strong peak at 630nm that has been reported as unknown defect in nanodiamond grown with bad surfaces [185]. It was hard to distinguish the Raman peak of the nanodiamond due to autofluorescence background from graphite and diamond-like carbon. To remove these contaminants, the sample was annealed to 600^oC in air for 7mins. Afterward the optical spectrum shows a clear nanodiamond Raman peak at 572.5nm, Figure 2.7(b), which corresponds to a Raman shift of 1326 cm^{-1} as shown in Figure 2.7(b,inset). TEM imaging was then performed to verify the presence of nanodimonds in the product from this first growth run. Low and high magnification of well crystalline and round shape nanodimonds were seen with (40nm average size) as presented in Figure 2.7(c). These nanodiamonds showed a crystal lattice spacing (2.06 ^oA) which matches diamond (111) lattice plane spacing reported in [194]as shown in figure 2.7(d). Here it should be noted that, in these first experiment, it was not clear if the nanodimonds were grown from the organic seed or not because the growth temperature was relatively high (550^oC). Although pure adamantane was shown not to decompose at this temperature, the nitrogen-containing adamantane derivative used in this growth.

2.3.2 Experiment 2

After verifying that our diamond growth apparatus produces nanodiamonds, it is time to lower the growth temperature significantly so as to enhance the chances of producing nanodiamonds via seeded growth. In experiment 2, we used the same growth mixture as in experiment 1. Basically, using 2-Azaadamantane hydrochloride organic seed which is expected to produce nitrogen-vacancy (NV center) in diamond after irradiation. The nanodiamond growth temperature was dropped below 400^oC which is well below adamantane decomposition temperature (550^oC)[140]. This time, we introduced tetramethylhydrazine in the growth mixture to prevent graphite and diamond-like carbon formation by converting all sp2 to sp3 through a hybridization process (or possibly just producing graphitic carbon nitride which is white and does not fluoresce like graphite). The sample was then loaded into a sample chamber in the diamond anvil cell and growth carried out at pressure equal to 10 GPa and temperature ranging from 380-400^oC for 24hours. By monitoring the sample during growth, it was clear that there was no graphite autofluorescence background as we encountered during experiment 1 that prevented optical monitoring during critical growth phases. The sample was then extracted after growth as described above in experiment 1.

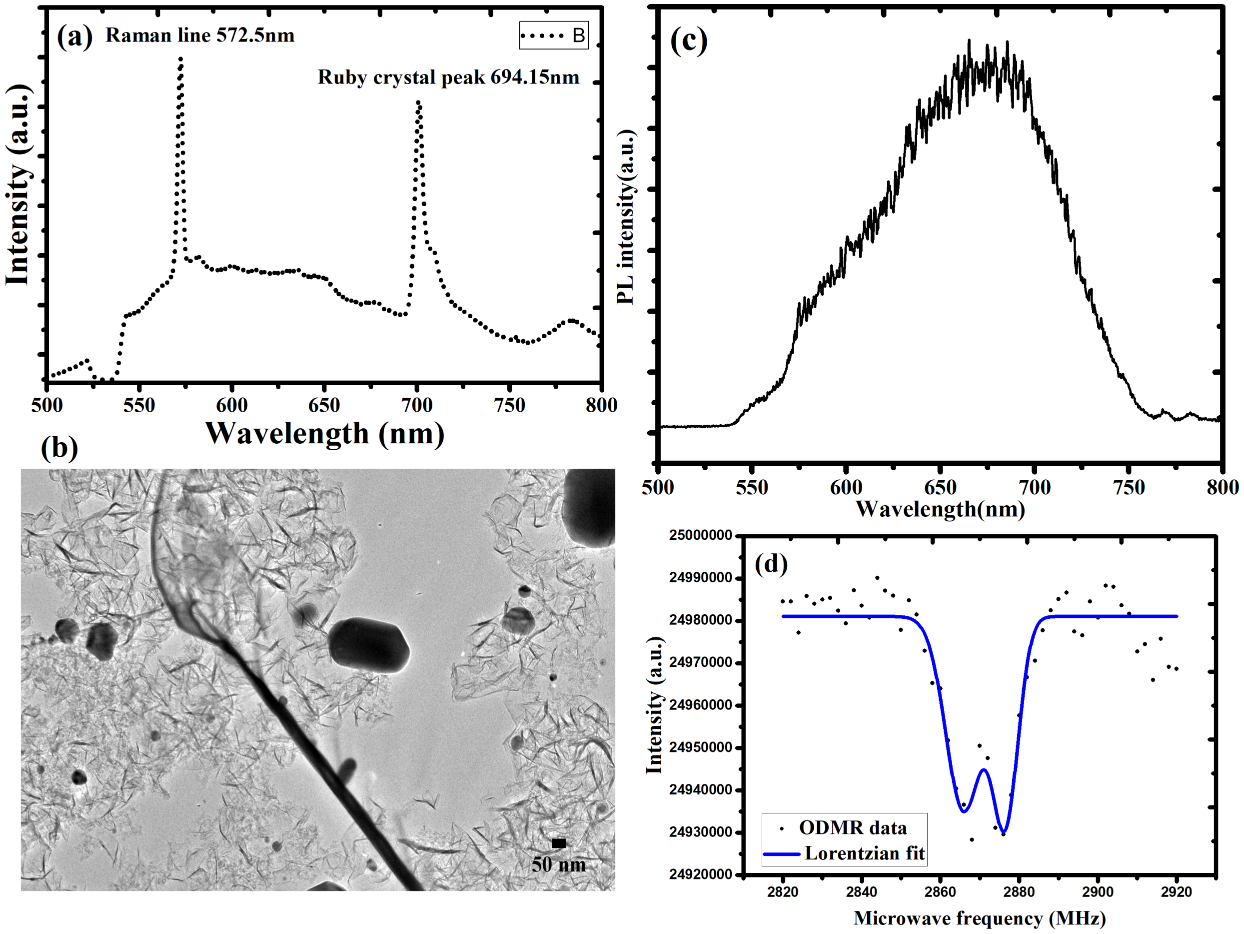

Figure 2.8: (a) An optical spectrum of grown nanodiamonds reveals a clear and strong nanodiamonds Raman peak at 572nm and ruby crystal peak at 694.20nm which is used to monitor applied pressure inside the diamond anvil cell.(b) low magnification TEM image of produced nanodiamonds which reveal well dispersed and round shape nanodiamonds crystals. (c) An optical emission spectrum of the NV center after irradiation certain areas of the grown nanodiamonds. (d) An ODMR spectra of the same irradiated nanodiamonds.

Interestingly, optical characterization of sample grown in experiment 2 showed a clear Raman peak at 572.5nm plus ruby crystal emission peak at 694.2nm, with no unwanted graphite (G) or diamond-like carbon (D) peaks, as shown in Figure 2.8(a). Furthermore, a TEM image shows many nanodiamonds with size range varying from 10nm to 100nm, as shown Figure 2.8(b). Note that these diamonds were only seen after heating the TEM grid to 800^oC for 10mins in vacuum using TEM heater stage. Before heating the nanodiamonds were buried underneath residual growth materials.

To create vacancies in the nanodiamonds, electron irradiation followed by high temperature annealing are needed. For this purpose, we chose and irradiated a small area on the TEM grid, containing several nanodiamonds. The irradiation was conducted in a JEOL 2010 TEM at an energy of 200 keV at a high temperature of 830^oC in vacuum for 1hour. The high irradiation temperature allowed a very high electron dose to be used without producing graphitization as would have been the case for room temperature irradiation at high dose. Due to the high irradiation temperature, post annealing was not performed.

After irradiation, the TEM grid was placed in our homemade laser scanning confocal microscope and the irradiated region was located in the optical image. The fluorescence spectra from this region is shown in Figure 2.8(c). The observed optical spectrum is similar to that expected for the NV center but without the characteristic zero-phonon (ZPL) peak. Therefore, it was necessary to perform ODMR to verify the creation of NVs. This is shown in Figure 2.8(d). Here, the signature ODMR spectrum of the NV center is seen in the irradiated spots on the grid.

Unfortunately this does not prove that the seeding process worked as there was considerable nitrogen in the growth mix and diamonds are known to efficiently incorporate even trace amounts of nitrogen during standard HPHT growth. Therefore, it was very important to perform another experiment to produce a color center from different seed that would only be seen if the seed molecule survived and was completely incorporated into the nanodiamond. Thais will be discussed in experiment 3.

2.3.3 Experiment 3

In this experiment, we used an interesting organic molecule that has two nitrogen atoms. Specifically, this seed can produce nanodiamonds with H3 color center if seeded growth worked or produces NV center otherwise. So, we introduced 5,7-dimethyl-1,3-diazaadamantane as a new seed to the growth mixture following our growth mix recipe as discussed in the sample preparation section.

Sample was then transferred into the diamond anvil cells and nearly the same growth conditions were used as in experiment 2. Specifically, the growth was conducted at temperature of 380-400^oC and pressure of 10 GPa for 24h. After growth was completed, the sample was then extracted following the same extraction procedure as in experiments 1 and 2. Again, for optical and TEM characterizations, a few drops of nanodiamonds solution were placed on a quartz slide and TEM grid, respectively.

After growth, Figure 2.9(a) shows a clear nanodiamond Raman peak and ruby emission peak at 572.5nm and 694.20nm respectively. Low and high magnification TEM images of nanodiamonds produced from experiment 3 are presented in Figure 2.9(b). The average size of the large nanodiamonds in high magnification TEM image was 50nm. However, there are seen to be different sizes of nanodiamonds (10-50nm) in the low magnification TEM image.

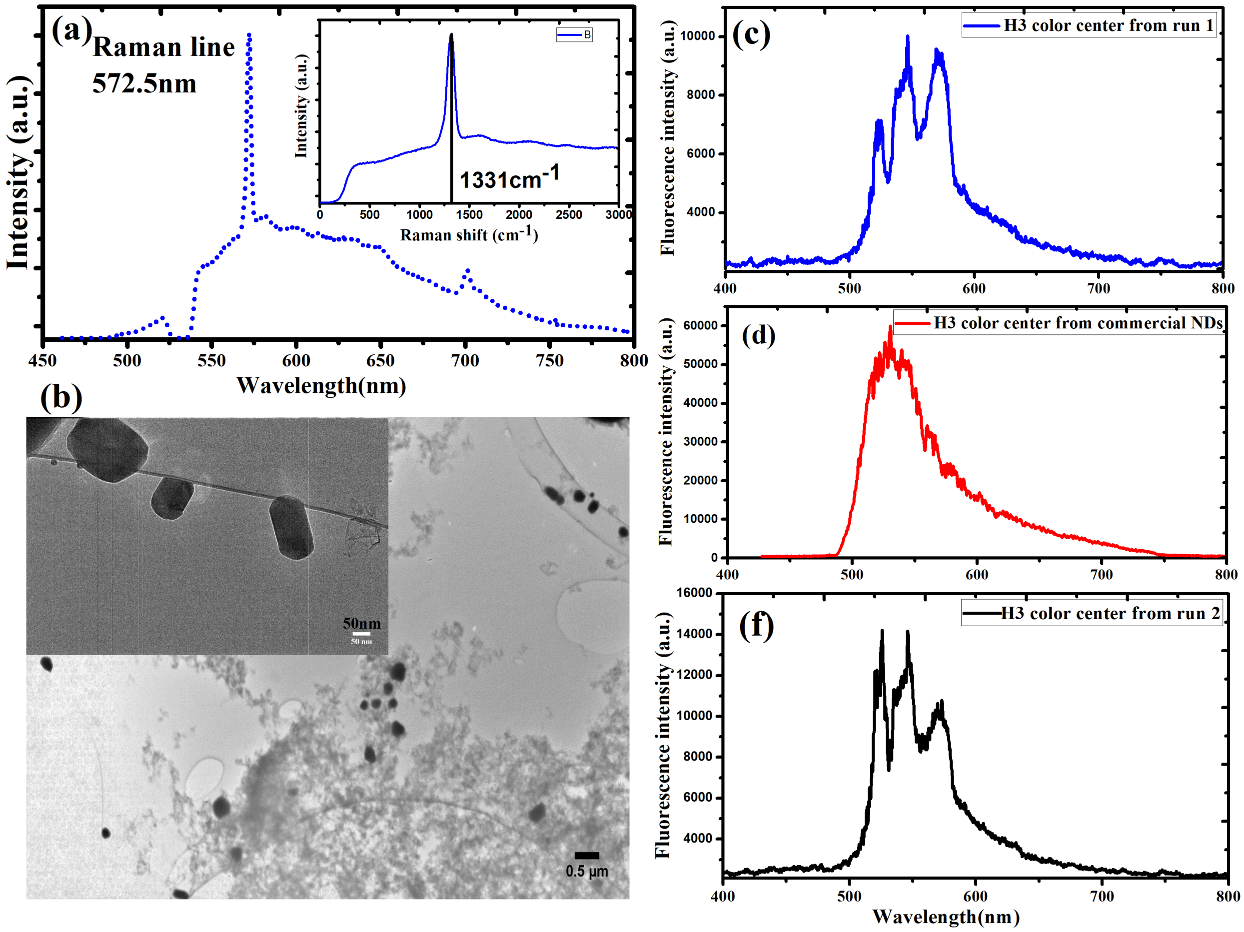

Figure 2.9: (a) An optical spectrum of grown nanodiamonds reveals a clear and strong nanodiamonds Raman peak at 572nm and ruby crystal peak at 694.20nm which is used to monitor applied pressure inside the diamond anvil cell .(b)low and high magnification TEM images of produced nanodiamonds which reveal well dispersed and round shape nanodiamonds crystals. (c and f) Optical emission spectra of H3 color center in nanodianonds created after irradiation certain areas of the grown nanodiamonds to created vacancies around two nitrogen atoms. These spectra of H3 color centere are in a good agreement with emission spectra of commercial nanodiamonds containing H3 color center as shown in (d).

Again it is necessary to create vacancies in the grown nanodiamonds in order to produce either the H3 or NV color centers. Therefore, we again irradiated nanodiamond crystals in some specific, randomly chosen areas on the TEM grid. The irradiation was performed again in a JEOL 2010 TEM at an energy of 200 keV at high temperature 830^{o}C in vacuum for 1hour. After irradiation, we scanned the irradiated areas using a confocal laser scanning microscope using equipped with a blue laser (471nm) which is known to excite H3 color center in diamond. Figure 2.9(c and f) illustrated an optical emission spectra which is similar to the emission spectra of commercial nanodiamonds containing H3 color center as shown in Figure 2.9(d).

Although the correspondence to the H3 spectrum is not exact, the important thing to note here is that we didn't observe the NV center optical emission spectrum. This has two possible implications: 1) the seed molecule did not decompose and diamond was grown around it, and 2) even though the concentration of nitrogen in the growth mix was orders of magnitude higher than for typical HPHT growth, little or none of it was incorporated into the diamond. This later suggest that the grown diamond is very high purity. However, to be sure there is seeded growth we still need to perform a control experiment with and without the diamond-like seed to insure that nanodiamonds can grow only when there is a seed molecule present. This control experiment will be discussed in experiment 4.

2.3.4 Experiment 4 (control)

Here we conducted a control experiment without seed molecules. As mentioned above, it is very important to confirm that we don't get nanodiamonds from the hydrocarbon growth mix in the absence of seed molecules. In this experiment we followed the same growth procedure as we did in experiments 2 and 3. Briefly, we mixed hydrocarbons that crack at low temperatures to give radicals (heptamethylnonane and tetracosane) with tetramethylhydrazine as shown in Figure 2.10(a) following our mixing ratios previously discussed in sample preparation section. The sample was then loaded into a sample chamber in the diamond anvil cell prior to growth experiment. This experiment was carried out at pressure equal to 10 GPa and temperature equal to 380-400^oC for 24h which is as close as possible to the previous seeded growth run. The temperature and pressure were then returned to ambient conditions and the sample was extracted following extraction method discussed above in the previous experiments. Prior to TEM imaging of the sample, a droplet of the sample solution was placed on a TEM grid. Importantly, we observed no nanodiamonds on high and low magnification TEM images as shown in Figure 2.10(b and c) respectively. In only one of the TEM grid squares, did we observed only one nanodiamond crystal as illustrated in Figure 2.10(d) which showed the correct diamond (111) lattice plane spacing (2.06^oA) in the diffraction image as shown in Figure 2.10(f). The presence of only one nanodiamond crystal can be attributed to a possible contamination present in the growth mix. The results from this experiment and experiments 2 and 3 strongly support our claim that our nanodiamonds are grown from seed molecules.

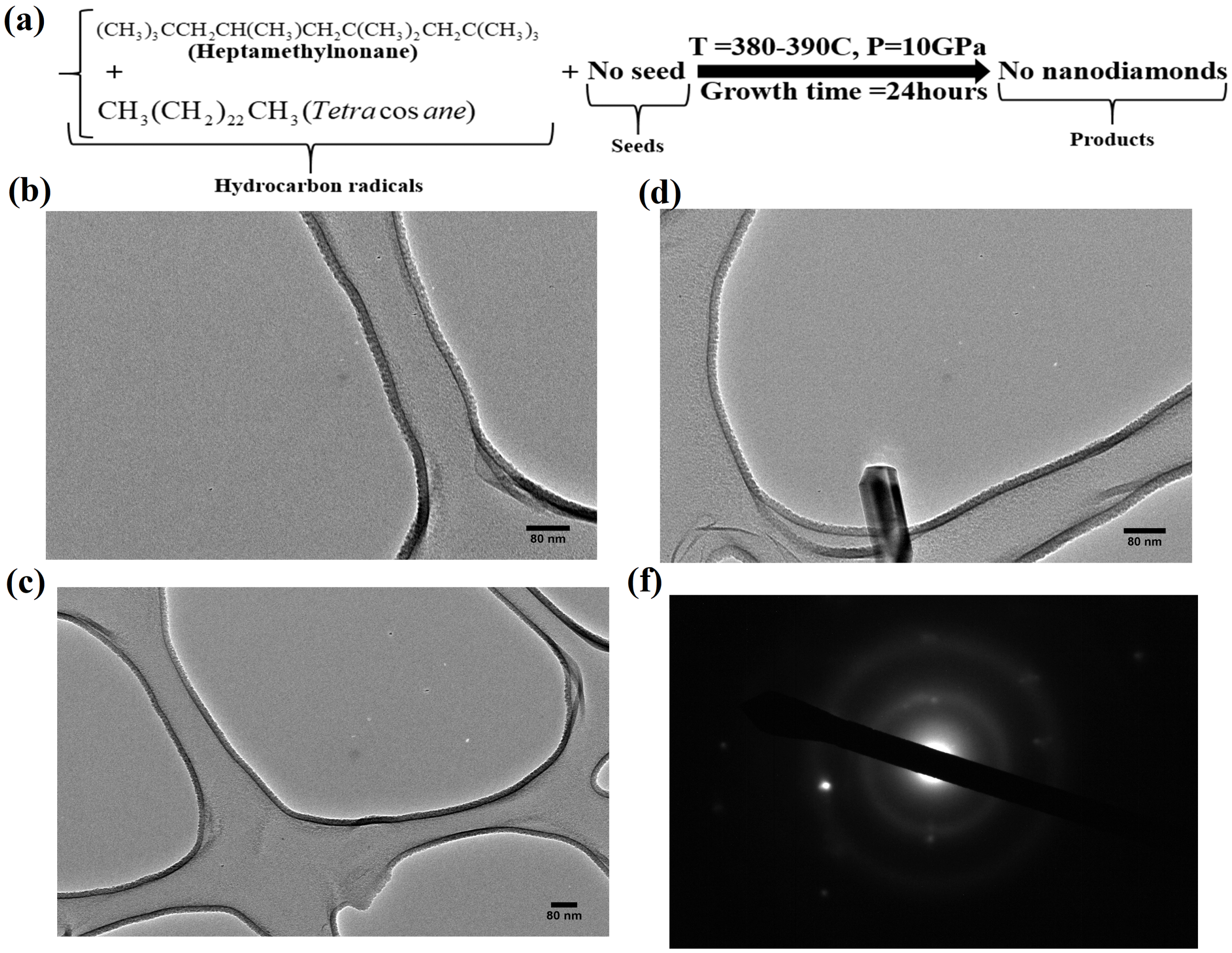

Figure 2.10: (a) an illustration of control experiment growth procedure. (a and c) low and high magnification images show no evidence of grown nanodiamonds without diamond like seed. (d) TEM image shows the only one nanodiamond crystal found in the control sample which might be due to a cross contamination form old diamonds growth runs. (f) TEM diffraction image that shows the right diffraction pattern of diamond crystal.

2.3.5 Experiment 5

In this experiment, we produced nanodiamonds from a specially synthesized organic seed consisting of a long chain of adamantane molecules poly(1-vinyladamantane). Due to the low decomposition temperature of this seed (estimated at 300^oC) the growth temperature was dropped to (250-270^oC). The rest of the growth mixture followed our mixing ratios discussed in the sample preparation section. This experiment was carried out using a diamond anvil cell at pressure equal to 10GPa and very low temperature below 270^oC for 24h.

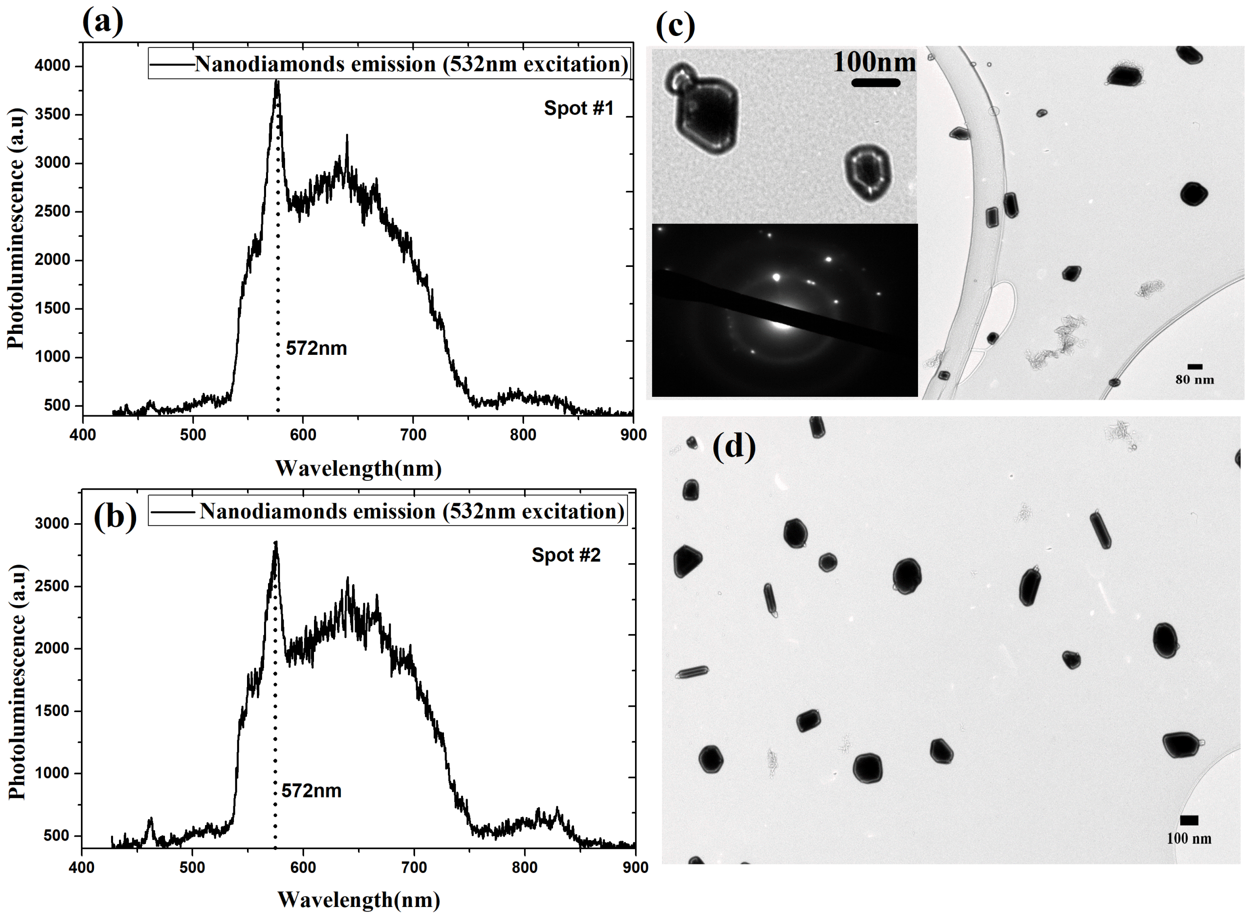

Figure 2.11: (a and b) Optical spectra of grown nanodiamonds from experiment 5 reveal a clear and strong nanodiamonds Raman peak at 572nm from two spots in the optical scan of the nanodiamonds sample. (c) Low and high magnification TEM images of produced nanodiamonds which reveal well dispersed and round shape nanodiamonds crystals. These crystals reveled clear diffraction patterns which shows the correct diamond (111) lattice plane spacing (2.06A) as shown in (c,inset). (d) The diamond like seed used in experiments 5 produced a lot of nanodiamonds covering the whole TEM grid.

After extracting the sample, an optical and TEM characterizations of the nanodiamonds were performed using a confocal laser scanning microscope and transmission electron microscope (TEM). Figure 2.11(a and b) demonstrate two optical spectra showing a clear nanodiamonds Raman peak at 572.5nm. These spectra were recorded from two different spots selected after imaging the nanodiamond sample using scanning green (532nm) laser excitation. Next, we performed TEM images of nanodiamond sample on a TEM grid. Figure 2.11(c) shows low and high magnification images of nanodiamonds with average size (100nm). We confirmed nanodiamonds by performing diffraction which shows the diamond (111) lattice plane spacing ($2.08^{o}A$) as seen in Figure 2.11(c, inset). Furthermore, this experiment illustrated a very high yield of nanodiamonds grown from the new seed, compared to the other, simpler seeds used in experiment 2 and 3 as shown in Figure 2.11(d). This may be due to a higher yield (of seed molecules that become diamonds) for the adamantane polymer, but we have yet to quantify the yield.

2.4 Conclusion

In this chapter, we conducted controlled diamond growth around diamond-like seed molecules at much lower temperatures than typical HPHT nanodiamond growth. We performed different experiments to confirm success of the seeded growth approach. In particular, we observed two different color centers in nanodiamonds grown from two different diamond-like organic seed molecules. Furthermore, we observed no nanodiamonds in the absence of diamond-like seed in a control experiment. These results strongly support our claim that our nanodiamond seeded growth approach is successfully working. This success will open the door for many interesting applications using ultrasmall nanodiamonds with stable fluorescence.

3. FLUORESCENT NANODIAMONDS FOR LUMINESCENT THERMOMETRY IN THE BIOLOGICAL TRANSPARENCY WINDOW

3.1 Introduction

Nanoscale luminescent thermometry is a promising approach to measure local temperature variations in living organisms [186]. These include quantum dots (QDs) [7, 8], upconversion nanoparticles (UCNPs) [15], organic dyes [9, 10], fluorescent polymers [11], and thermal imaging [13]. Most of these fluorescent nanothermometers are sensitive enough to detect a sub-kelvin rise in temperature in living cells [7–11, 13–15]. However, many of the existing nanothermometers are limited by photostability [7–10], toxicity [7–10, 16], low quantum efficiency [15, 167], and chemical environment sensitivity [11].

Optical temperature sensing with color centers in fluorescent nanodiamonds (FNDs) are promising approaches to overcome the drawbacks of current methods owing to their remarkable optical properties [83–85]. The nitrogen-vacancy (NV) color center was the first color center in diamonds used to measure temperature. The NV center uses a magnetic spin transition whose resonance frequency is sensitive to thermally-induced lattice expansion. The NV color center has shown high sensitivity, which can detect temperature variations down to 1.8 mk/$\sqrt{Hz}$ in pure-diamond crystal and 200 mk/$\sqrt{Hz}$ in nanodiamonds with spatial resolution of 200 nm [14].

However, the optical pumping (blue and green) wavelengths of many interesting color centers in diamonds, including the nitrogen-vacancy, have been reported to cause heating and serious photodamage to biological tissues even with relatively low power intensity, as low as $2kW/cm^2$ [135]. Furthermore, the green excitation of the NV center induces autofluorescence in biological tissues, which overlaps with the unique fluorescence of the NV center as shown in Figure 3.1, resulting in a significant sensitivity reduction in deep tissue-imaging and bio-sensing [16, 17].

To overcome these limitations, fluorescent nanodiamonds with color centers that can be excited within the biological transparency window range (640-1350 nm) are needed as shown in Figure

3.1, where overheating and photodamage in biological tissues are greatly minimized [135]. Recent reports, using micron-sized diamonds, have shown that the excitation bands of NV^- centers in diamonds can be extended to the resonant wavelength of 638 nm (zero phonon line), where efficient temperature measurements can be achieved [99]. In addition, temperature measurement within the biological transparency window by the silicon vacancy (SiV) defect in diamonds has been recently reported [92]. Here the temperature sensitivity reached 360 mk/$\sqrt{Hz}$ in bulk diamond and 521 mk/$\sqrt{Hz}$ in 200 nm nanodiamonds at room temperature [92]. Like NV, the SiV measures temperature using a narrow optical transition that is sensitive to thermal lattice expansion. In addition, the SiV color center has potential for ultra-high resolution thermometry, as stable SiV fluorescence has been seen in ultra-small (1.2 nm) nanodiamonds [127].

Another color center operating within the biological transparency window, based on nickel (Ni) has been proposed as a fluorescent marker [187]. The nickel color center in diamonds consists of a substitutional Ni site in the diamond lattice, which possesses a strong photoluminescence (PL) doublet around 883/885nm [129, 130], which is attributed to ground state splitting caused by the spin orbital interaction. The optical properties of Ni-related centers in diamonds have been investigated in detail at both low and room temperatures [187, 188].

Here we show that the optical spectrum of the Ni complex is very sensitive to temperature near room temperature, and is therefore a good candidate for nano thermometry. We also show that it is possible to excite the NV center with a more biocompatible wavelength (660 nm) where autofluorescence background, overheating, and photodamage are greatly minimized [135]. Since the NV and Ni measure temperature by different physical mechanisms, their simultaneous use can avoid confusion by other cell processes, as these would impact each temperature sensor differently [94].

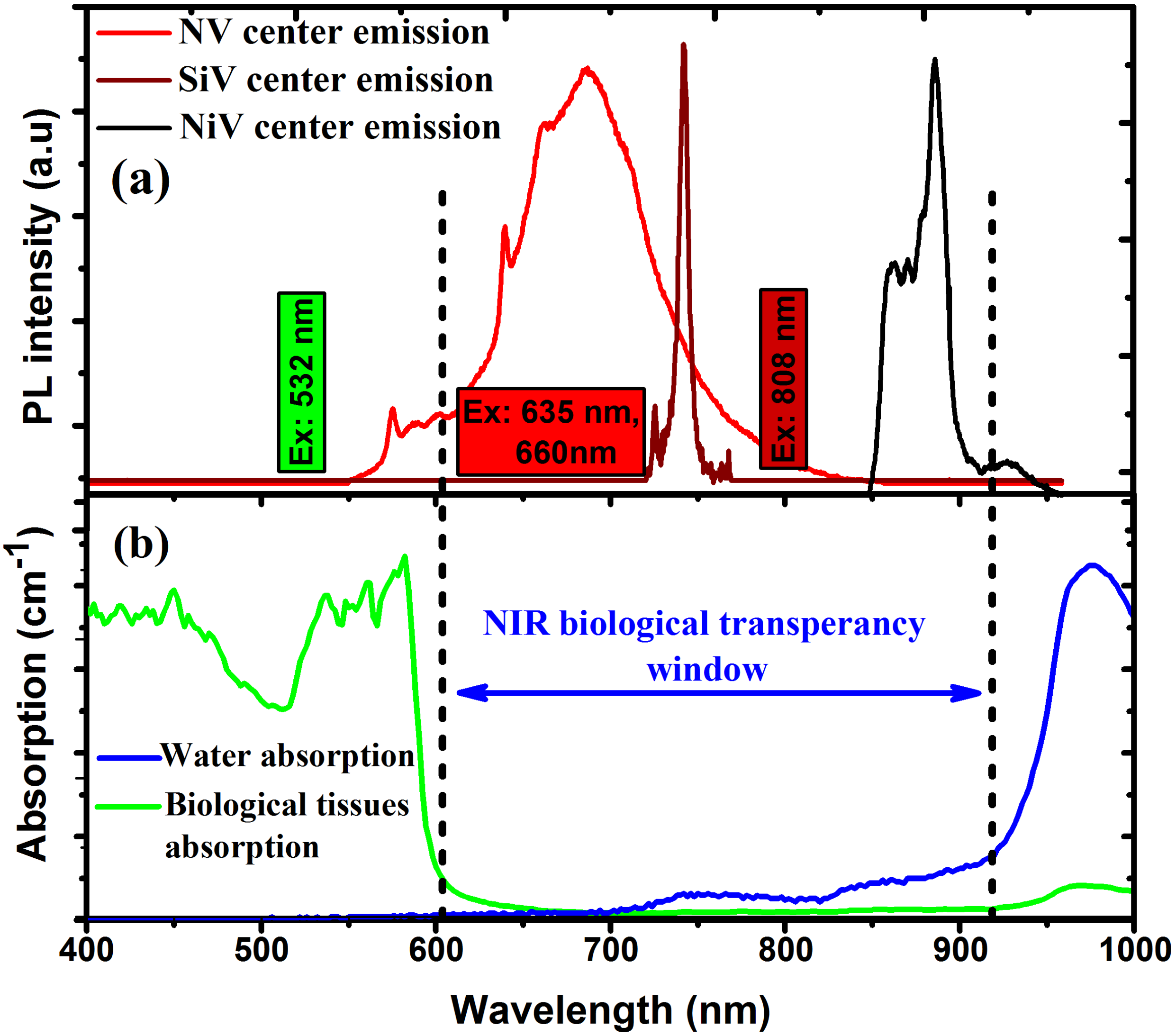

Figure 3.1: (a) Superimposed photoluminescence of fluorescent nanodiamonds (FNDs) color centers namely; nitrogen-vacancy, silicon-vacancy(SiV), and nickel-vacancy (NiV) under 660 nm (CW) illuminations. The fluorescence of all color centers in FNDs and the excitation wavelengths (660nm and 800nm) are located in the NIR biological transparency window. (b) Absorption spectra of distilled water (DI water) and biological tissue taken over the visible and the near-infrared (NIR) range.

3.2 Results and Discussion

High pressure and High temperature (HPHT) fluorescent nanodiamonds (FNDs) with an average size of 100 nm were used in this experiment. Prior to use in our study, TEM images and particle size distribution characterizations of the FNDs were performed. A droplet of 1 mg/mL of

FNDs suspended in water was placed onto a TEM grid and dried prior to imaging. Figure 3.2(a) shows a high resolution TEM image revealing highly dispersed nanodiamonds with 100 nm average size. The average size of FNDs was further confirmed by dynamic light scattering (DLS), as shown in Figure 3.2(b).

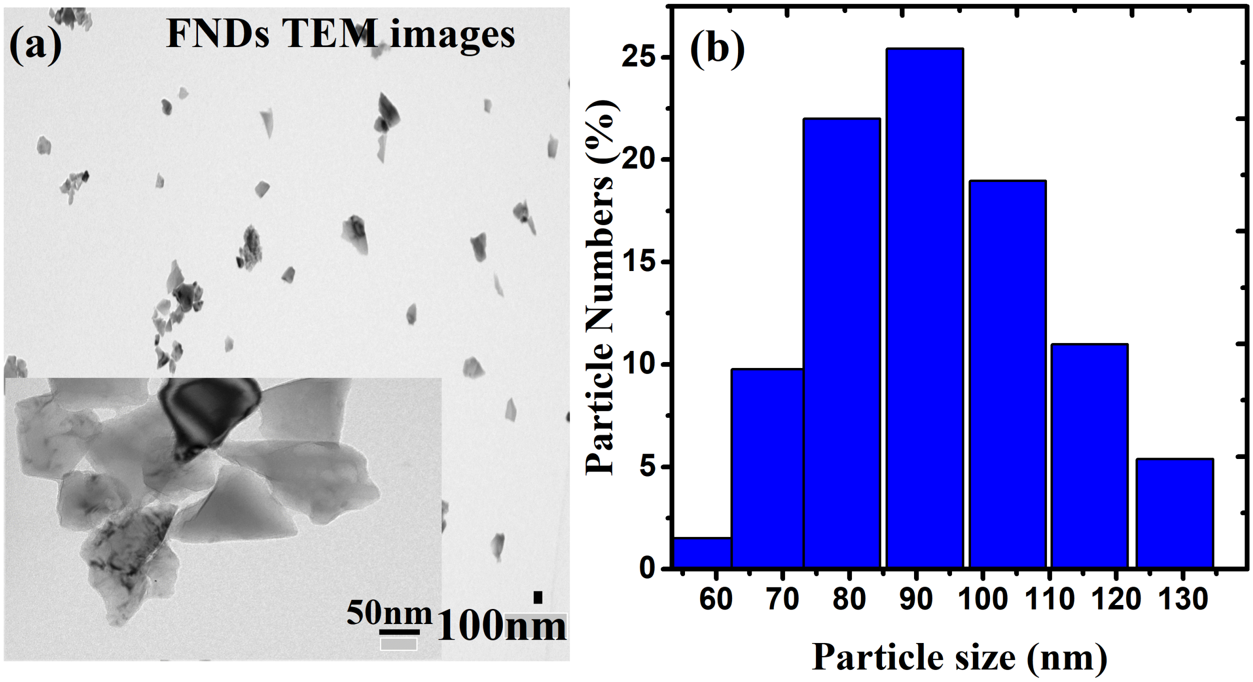

Figure 3.2: (a) High magnification TEM image of the fluorescent nanodiamonds (FNDs) dispersed in water and dropped onto a microgrid. The TEM images show well dispersed and nonagglomerated FNDs with average size (100nm) (b) Average size distribution of the FNDs recorded by DLS.

To analyze the fluorescence of color centers present in the nanodiamonds, we designed a homebuilt multi-color confocal scanning microscope equipped with several continuous wave (CW) laser diodes (532 nm, 635 nm, 660 nm, 808 nm and 980 nm). The excitation lasers were focused through a long working distance NIR microscope objective with NA = 0.8 (Olympus) with magnification of 100x. The fluorescence of nanodiamond color centers was filtered out of reflected lasers by several optical notch filters for each illumination wavelengths and analyzed by a photon counter and homebuilt spectrophotometer.

We investigated the photoluminescence spectra of a thin layer of fluorescent NV-containing nanodiamond crystals which was prepared as followed: a droplet of (1 mg/mL) of the FNDs mixed with Poly vinyl alcohol (PVA) at (1:1 w/w) ratio was spin-coated on a piece of quartz to make a thin layer of individual crystals to avoid undesired agglomerated emitters. The sample was then attached to a microwave board, which was attached to a compact heater for the temperature-dependent measurements and placed on the confocal microscope. The sample was examined under excitation by three laser diodes (532, 660 nm, and 808 nm) with the same power intensity (900 W/cm^2). Under green (532 nm) illumination, FNDs showed a clear nitrogen-vacancy photoluminescence with neutral nitrogen-vacancy (NV^0) and negatively charged nitrogen-vacancy (NV^-) zero-phonon lines peaked at 575 nm, and 638 nm, respectively; as shown in Figure 3.3(a). Interestingly, with red excitation at 660 nm, the fluorescence spectra of the FNDs still displayed the unique emission of NV color centers, as shown in Figure 3.3(b). This lack of bleaching of NV centers in these nanodiamonds under 660 nm wavelength is believed to be due to nitrogen doping (N), which can increase NV^- population by donating electrons to NV^0 in nanodiamonds [189, 190], because the activation energy (EA = 1.70 eV) of N is lower than the acceptor level of the NV center labeled NV^-, as shown in Figure 3.3(b,inset) [191, 192]. A further demonstration of this result using bulk diamonds samples will be discussed later in this study.

One drawback of 660 nm excitation of the NV center fluorescence is 10x weaker absorption than at 532 nm green light; however, based on the biological tissue absorption curve shown in Figure 3.1(b) the tissue damage threshold should be at least 30x less. In our experiments we used 660 nm excitation at a power intensity of 900 W/cm^2 , 8 times lower than the biological tissue damage threshold (7.1 kW/cm^2) [135, 193], as shown in Figure 3.3(d).

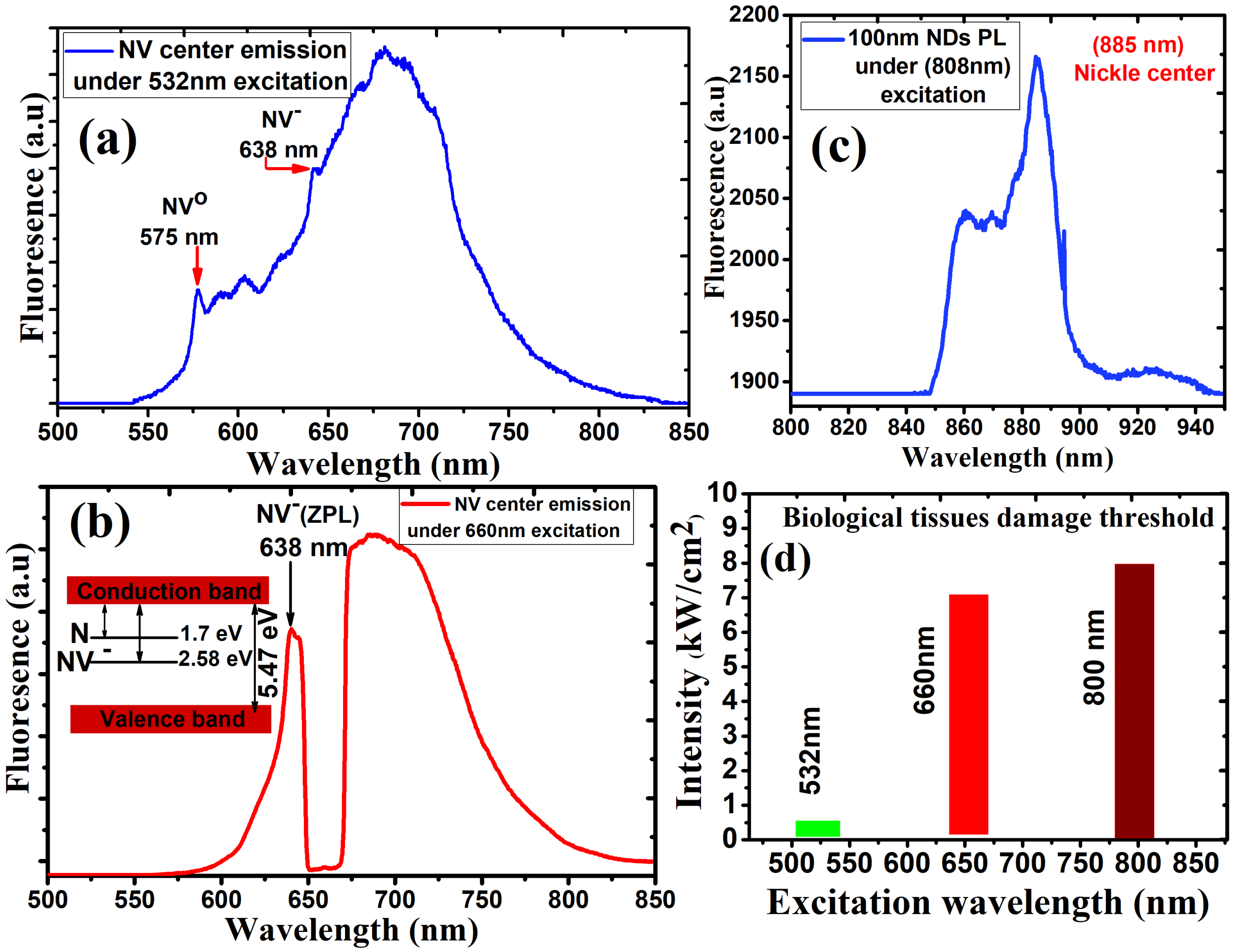

Figure 3.3: (a) Photoluminescence of NV color centers in fluorescent nanodiamonds (FNDs) under 532 nm green excitation. The Fluorescence spectrum shows the zero-phonon line (ZPL) of the (NV^0) and (NV^-) zero-phonon lines peaked at 575 nm, and 638 nm, respectively.(b)The Fluorescence spectrum of NV center under 660 nm red excitation(red excitation was filtered from the fluorescence spectrum by 660 nm notch filter). The NV center emission spectrum shows the zero-phonon line (ZPL) of the (NV^-) zero-phonon line peaked at 638 nm. (b,inset) Donor energy levels nitrogen donors and acceptor level of the NV- center with respect to conduction-band edge of diamond. (c) Fluorescence spectrum of nickel color center in FNDs under 808 nm (CW) excitation wavelength. (d) Biological tissues damage threshold under continuous illumination wavelengths (532nm, 660, and 808nm) projected to the biological tissues absorption spectrum.

Next, we performed Optically Detected Magnetic Resonance (ODMR) with FNDs containing NV centers with deep red 660 nm laser excitation. Briefly, phonon assisted optical absorption followed by spin selective decay polarizes the NV center into the $m_s = 0$ spin sublevel (80% populated). When a resonant microwave field induces a magnetic transition between the $m_s = 0$

spin sublevel and the $m_s = \pm 1$ levels, a significant decrease of NV fluorescence results, which is called optically-detected magnetic spin resonance (ODMR) [39, 50]. ODMR in NV centers in nanodiamonds serves as a quantum sensor to read out important physical quantities of a nanoscale system such us temperature, electric field, and magnetic field. Figure 3.4(a) shows the ODMR spectrum of our FNDs with green (532 nm) laser excitation with contrast of 6.7% and Figure 3.4(b) shows the ODMR obtained with red (660 nm) excitation with contrast of 2.4%.

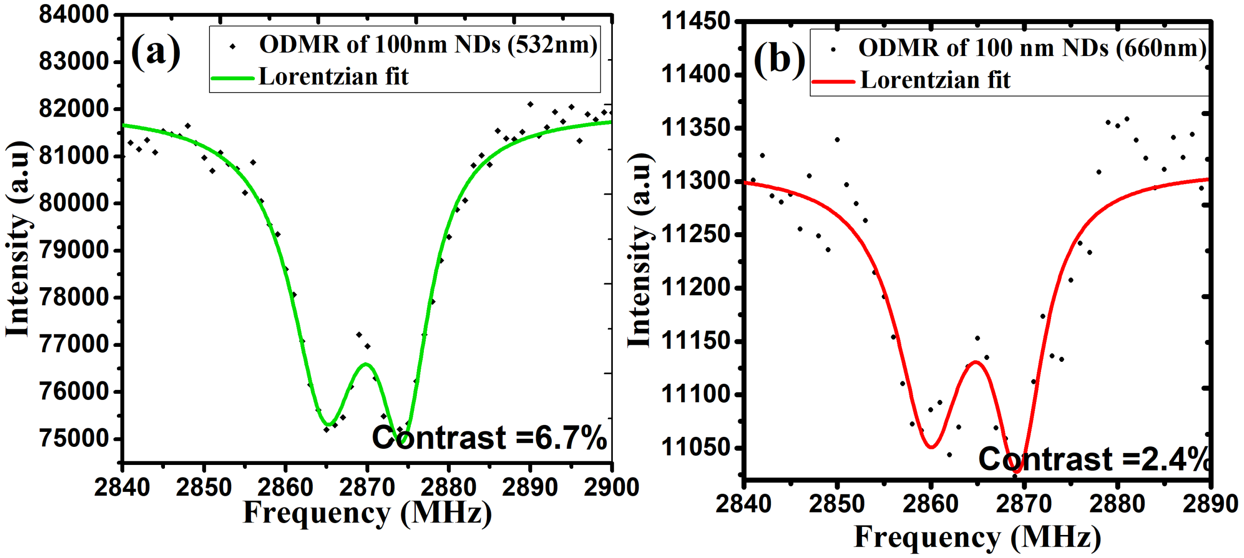

Figure 3.4: (a) ODMR spectrum of NV center in fluorescent nanodiamonds (FNDs) under green excitation (532nm) at laser intensity ($900W/cm^2$) with contrast =6.7%. (b) ODMR spectrum of NV in FNDs center under red excitation (660nm) at the same laser intensity with contrast =2.4%.

To illustrate the role of nitrogen in NV stability under red illumination [192], we carried out ODMR experiments using two bulk samples; 1b type and 2a type. Figure 3.5(a and c) show ODMR in the 1b sample under 532 nm and 660 nm laser excitation with contrasts of 7% and 3%, respectively, which is in a good agreement with the FNDs data in Figure 3.4(a and b). In contrast, the 2a sample showed ODMR with 5% contrast upon green, 532 nm, illumination, but none with red illumination, as shown in Figure 3.5(b and d).

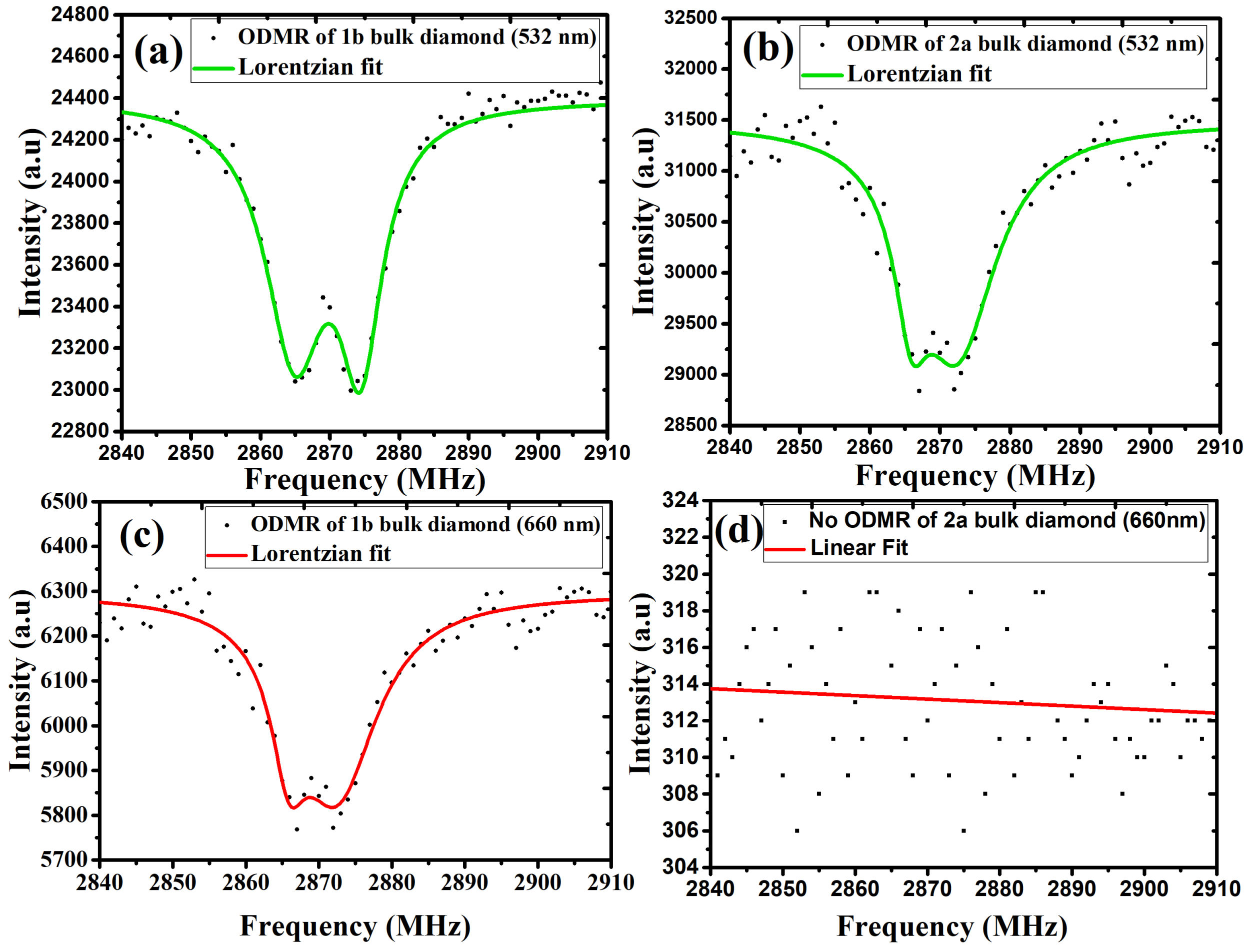

Figure 3.5: A proof of principle ODMR experiment of 1b bulck diamond (with very high nitrogen content) and 2a bulk diamond. (a and c) ODMR spectra of 1b bulk diamond under green and red excitations with contrast equal to 5.35%,and 2.9% respectively. This result is in a good agreement with the ODMR observed in FNDs in Fig.3 because very high content of nitrogen is expected to have some electrons in the conduction band which can stabilize the NV-under red excitation. (b and d) ODMR spectrum of 2a bulk diamond only at green excitation with contrast equal to 7%.

Now we demonstrate nanoscale temperature sensing with biocompatible deep red 660 nm illumination of NVs in nanodiamonds using ODMR in NV nanodiamonds. Figure 3.6(a) illustrates that temperature changes as a function of ODMR spectral shifts over a 24 ^oC to 40 ^oC temperature range. As the temperature of the nanodiamonds increases, the spectrum of the ODMR is shifted toward lower microwave frequencies. Fitting the experimental data shown in Figure 3.6(b) to a linear equation with slope dM/dT=-72kHz/C shows linear dependence between the frequency shift of the ODMR spectra and temperature, which provides a good calibration for temperature measurements using FNDs. These results show good agreement with previous studies [45, 99]. The sensitivity of the NV center nano-thermometer in this study is 350mK/$\sqrt{Hz}$.

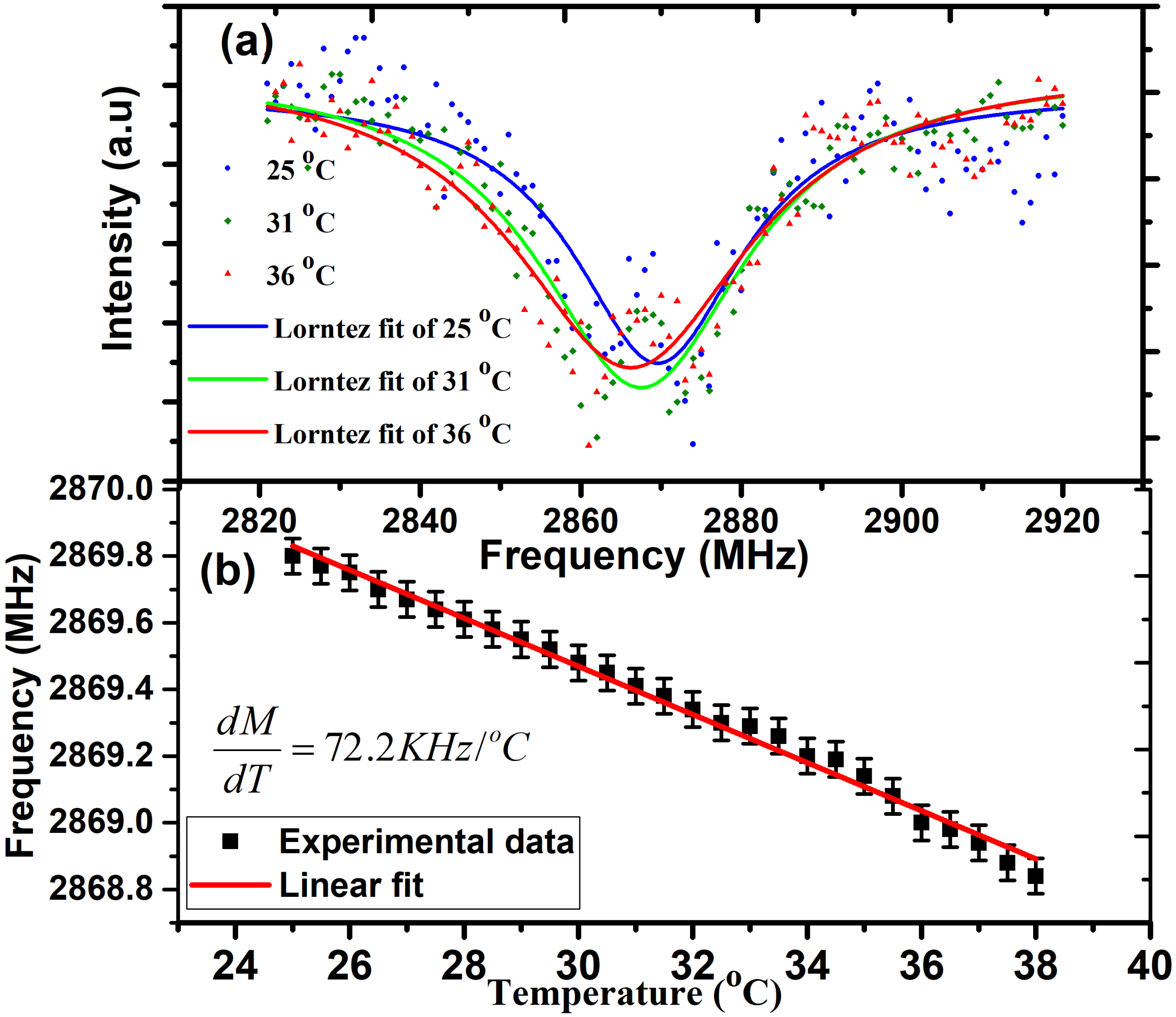

Figure 3.6: (a) Luminescence emission spectra of NV color center in nanodiamonds under 660nm illumination as a function of the microwave frequency at different temperatures; (25°C blue), (31°C green), and (25°C red).recorded over a small temperature range (25°C-40°C) . (b) Linear fitting of the central frequency of the ODMR spectrum of NV centers in FNDs as a function of ambient temperatures.

Next, we demonstrate nanoscale temperature sensing with biocompatible 808 nm laser illumination of Ni color centers in nanodiamonds. The photoluminescence (PL) of the nickel color center is shown in Figure 3.3(c). The unique PL of the Ni center can be attributed to ground-state splitting caused by the spin orbital interaction [129, 188]. As shown in Figure 3.7(b), the peak fluorescence intensity decreases significantly with increasing temperature, but the area is constant. Similar behavior is seen for NV and SiV but is not so pronounced at room temperature [194, 195]. The temperature dependence of the change of Ni photoluminescence is consistent with $aT + bT^2$ dependence. The sensitivity of the Ni color center nano-thermometer in this study is 181 mK/$\sqrt{Hz}$.

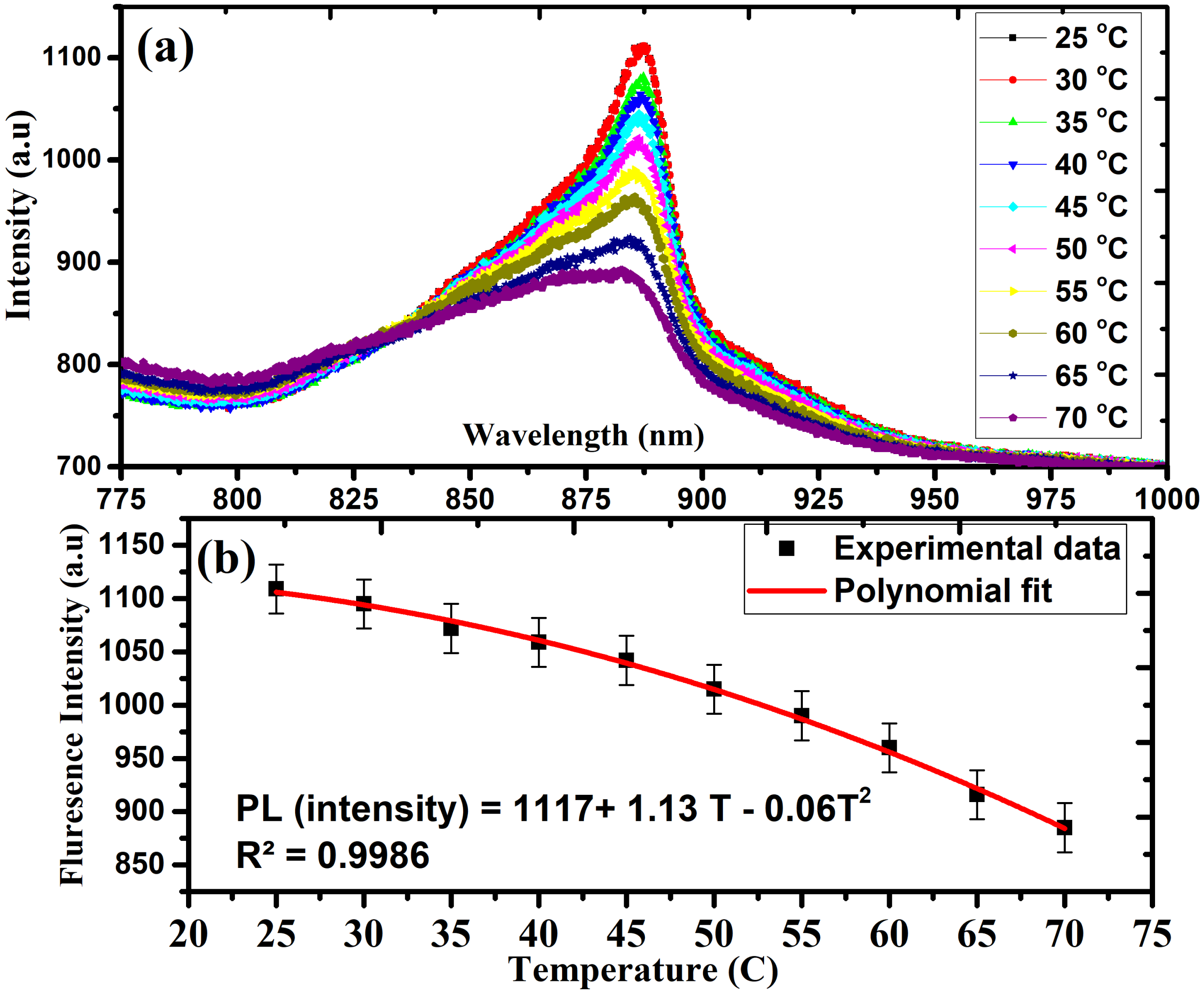

Figure 3.7: (a) Photoluminescence emission spectra of nickel color center (NiV) in nanodiamonds under 808nm illumination as a function of the ambient temperatures. (b) Intensity of photoluminescence of NiV color center in nanodiamonds measured as a function of the ambient temperature (filled circles) and its best polynomial fit (solid line).

3.3 Conclusion

In this work we report temperature sensing with NV and Ni diamond color centers excited in the biological transparency window in FNDs crystals. For NV we show good ODMR signal at laser intensity well below the biological tissues damage threshold. Importantly, optical temperature sensing using NV and Ni color centers can be performed simultaneously using different physical mechanisms. This is a promising approach to avoid sensor confusion and provide accurate temperature measurements within living biological systems.

4. HIGH EFFICIENCY UPCONVERSION NANOPHOSPHORS FOR HIGH-CONTRAST BIOIMAGING*

4.1 Introduction

In recent years, increasing attention has been focused on research and applications of fluorescent markers in biomedical imaging [3, 141]. Conventional fluorophores such as quantum dots (QDs) and organic dyes exhibit high luminescence efficiency and hence are excellent fluorescent bio-probes. However, the fluorescence of theses fluorescent markers overlaps with biological tissue auto-fluorescence resulting in a significant background that reduces sensitivity in deep tissue imaging [196]. Upconversion fluorescence can solve the auto-fluorescence problem because their emission is to the blue of the pump laser and is easily filtered out from the red-shifted autofluorescence. Yet upconversion dyes and quantum dots require high infrared intensities (typically $10^7 - 10^{11}$ $W.cm^{-2}$), requiring expensive pulsed lasers which can damage biological tissue [16, 159]. Furthermore, most of the upconversion dyes and quantum dots are limited by toxicity, photobleaching and blinking [197–199].

To overcome these drawbacks, upconversion nanoparticles doped with lanthanide ions Ln^{+3} (Ln=Er,Tm,Ho,etc.) are used [29, 163]. The most efficient upconversion process in rare-earth doped nanomaterials is energy transfer upconversion (ETU) in which sensitizer ions with large absorption cross-sections at near-infrared (NIR) wavelengths sequentially transfer absorbed energy to emitter ion [140, 145, 146]. This will be discussed in detail in the Results and Discussion section. These upconversion processes can operate at lower pump laser intensities because they possess real long-lived intermediate states (lifetimes on the microsecond scale). Therefore, inexpensive low-power lasers (typically $1 - 10^3$ $W.cm^{-2}$) can be used for their excitation [139, 147, 149].

---

*Reprinted with permission from High efficiency upconversion nanophosphors for high-contrast bioimaging by Masfer H Alkahtani, Fahad S Alghannam, Carlos Sanchez, Carmen L Gomes, Hong Liang, Philip R Hemmer, 2016. Nanotechnology, vol. 27, pp. 485501, Copyright [2016] by IOP Publishing, and High resolution fluorescence bio-imaging upconversion nanoparticles in insects by Masfer Alkahtani, Yunyun Chen, Julie J Pedraza, Jorge M Gonzalez, Dilworth Y Parkinson, Philip R Hemmer, Hong Liang, 2017. Optics Express, vol. 25, pp. 1030-1039, Copyright [2017] by the Optical Society of America

Rare earth doped upconversion nanoparticles (UCNPs) have been successfully implemented in biological imaging at the cell level, and in the tissues of small animals like mice. UCNPs can also be used for single-particle imaging due to their UCNPs's brightness even after long-time continuous laser illumination [150–152].

Upconversion nanoparticles of $\beta - NaYF_4 : Yb^{+3}, Er^{+3}$ and $\beta - NaGdF_4 : Yb^{+3}, Er^{+3}$ have been reported as one of the most efficient UCNPs with strong up-conversion luminescence (UCL). However, they work optimally in organic solvents such as cyclohexane and their UCL drops significantly when dispersed in water [157] (at least for small particle sizes). Specifically, the standard upconversion nanoparticles $NaYF_4 : Yb^{+3}, Er^{+3}$ quantum yield is 3% in bulk particles at 980 nm illumination. However, this quantum efficiency drops to 0.005% at 980 nm illumination for 10 nm particle size dispersed in hexane, and 0% at the same size (10 nm) when dispersed in water [158, 159]. Therefore, the commonly used $NaYF_4 : Yb^{+3}, Er^{+3}$ nanoparticles are not favorable in many bioimaging applications since water is present in most biological tissues.

Recently, water tolerant upconversion nanoparticles $YVO_4 : Er^{+3}, Yb^{+3}$ have been proposed. Their quantum efficiency is 1.3% at 980 nm illumination for 10 nm particle size. The only disadvantage of $YVO_4 : Er^{+3}, Yb^{+3}$ nanoparticles is higher saturation laser power, However, even for illumination of only 550 $W.cm^{-2}$ the quantum yield is 0.1% for 10 nm particle size in water [148] which is still higher than the best quantum yield for $NaYF_4 : Yb^{+3}, Er^{+3}$ nanoparticles at the same size in hexane. So $YVO_4 : Er^{+3}, Yb^{+3}$ nanoparticles are considered to be the best solution for water-based bio-application compared to the commonly used $NaYF_4 : Yb^{+3}, Er^{+3}$ nanoparticles.

It is known that the efficiency of upconversion nanoparticles can be significantly influenced by the quality of the host materials; therefore, it is important to select host crystals that maintain excellent optical properties and chemical stability in water, even down to the single particle level such as YVO_4 particles [160, 161].

In this work, we synthesized $YVO_4 : Er^{+3}, Yb^{+3}$ nanoparticles following the procedure in, [148, 162] which recently demonstrated high upconversion efficiency in water down to the single-particle level with an estimated size range of 30-40 nm. These nanoparticles were injected into fire ants in order to observe the upconversion luminescence emission efficiency of $YVO_4 : Er^{+3}, Yb^{+3}$ nanoparticles inside an ant's body using a relatively low excitation intensity of 10 $kW.cm^{-2}$ at 980 nm in a homemade wide-field setup. Fire ants are ideal biological model in this study due to the increasing number of fire ants in southern states due to climate change [200]. Furthermore, fire ants have brought enormous inconvenience to household and present threat to people out doors [201]. To date, we have not been able to find alternative to control them. Imaging small and stable upconversion nanoparticles in fire ants would be the first step to study and understand their habits in order to find effective methods to control them and improve pest management techniques. Moreover, the widespread use of nanoparticles in our daily life causes toxicity. These nanoparticles would enter our food chain trough small insects such as fire ants which consistently seek small particles as a potential food source as part of a highly simplified food chain [202]. The ability of imaging upconversion nanoparticles in fire ants would open up alternative approaches for future investigation of nanoparticles transport to the food chain. In addition, fire ants are not considered animals and are readily available at no cost. For high resolution a small sampling research, fire ants serve as an alternative to mammalian models. In this section, I was able to clearly detect the upconversion luminescence emission of $YVO_4 : Er^{+3}, Yb^{+3}$ nanoparticles from inside the body of the ants. This is attributed to the low autofluoresence background, non-photobleaching, and non-blinking observed when using $YVO_4 : Er^{+3}, Yb^{+3}$ nanoparticles.

4.2 Experimental details

4.2.1 Nanocrystals synthesis

Recently, $YVO_4 : Er^{+3}, Yb^{+3}$ nanoparticles were synthesized as described by [148, 162]. In this work, we successfully reproduced highly crystalline and uniform $YVO_4 : Er^{+3}, Yb^{+3}$ using the following procedures. A 10 mL solution of 0.78 mole/L $Y(NO)_3)_3.4H_2O$, 0.002 mole/L $Er(NO)_3)_3.5H_2O$, and 0.2 mole/L $Yb(NO)_3)_3.5H_2O$ was prepared and slowly added dropwise using a peristaltic pump to a 10 mL solution of 0.1 mole/L orthovanadate Na3VO4 solution under constant stirring with a few drops of 1 M NaOH to maintain the pH above 11 for 30 minutes at room temperature. A white colored precipitate appeared during the mixing corresponding to the formation of $YVO_4 : Er^{+3}, Yb^{+3}$ nanoparticles. The solution was purified with a dialysis kit (Biovision dialyzer MWCO 3.5 kDa) against pure water overnight and sonicated for 10 minutes using a 450 W Branson sonicator. The solution was stabilized by a polymer, poly(acrylic acid) (PAA) with a molar ratio of vanadate particles to PAA of 1:0.05 in order to avoid agglomeration. A silica sol-gel matrix was prepared to maintain the particle size during the annealing treatment at high temperature by mixing TEOS ($Si(OC_2H_5)_4$), ethanol, and water (pH 1.25) in a 1:5:3.8 molar ratio under constant stirring for 1 hour at 60^oC. Also, Pluronic PE6800 copolymer was dissolved in ethanol at 40.4 g/L to stabilize the nanocrystals against thermal-induced aggregation during the high temperature treatment. The $YVO_4 : Er^{+3}, Yb^{+3}$ nanoparticles were incorporated into silica sol and the Pluronic PE6800 copolymer according to the molar ratio V/Si/PE6800 = 1:5:0.05. The final solution was dried at 90^oC in a Thermo Scientific vacuum oven at 30 inch of mercury (10^5 pascals) pressure for 4 hours. The resulting powder was ground using a pestle and mortar and then processed through a high temperature treatment consisting of calcination for 1 hour at 500^oC followed by annealing for 10 minutes at 1000^oC. For the recovery process after the annealing, the annealed particles were dissolved in 3% hydrofluoric acid in excess to remove the silica matrix from particles for 3 hours in the molar ratio Si/HF = 1:9. The hydrofluoric and dissolved silica were removed by 3 centrifuge runs at 5500g and subsequent washing with pure water. A few drops of sodium hydroxide were added to the precipitated particles solution to keep the pH at 11-13. Moreover, in order to reach the desired size similar to that before heat treatment, the particles were sonicated for 5 minutes and stabilized with PAA at the molar ratio V/PAA = 1:0.05. Finally, $YVO_4 : Er^{+3}, Yb^{+3}$ nanoparticles were synthesized and stored at room temperature.

4.2.2 Biological samples preparation

4.2.2.1 Ants injected with UCNPs

Red imported fire ants (Solenopsis invicta) were used in this study. Ant colonies were reared under controlled temperature (25 ± 2 ^oC) and humidity (45 ± 2%), and kept under an 8 hour alternating light cycle. Colonies were housed in plastic containers and given water, sugar, and vegetables ad libitum. Fire ants chosen for injection were based on relative size. Larger ants (4.5 to 6 mm long and 1 to 2 mm wide) were randomly selected from the colony and then separated into individual containers. Ants were then administered CO_2 gas for about 30 seconds for sedation. A hypodermic needle and micropipette were then used to inject 3 μL of $YVO_4 : Er^{+3}, Yb^{+3}$ nanoparticle colloidal solution into the abdomen of each ant. After injection, the ants were returned to the individual containers for 24 hours before being fixed with $Kahle's$ solution. The $Kahle's$ solution was prepared by mixing (6 mL formaldehyde, 15 mL 95% ethanol, 2 mL glacial acetic acid, 60 mL distilled water) as discussed in [203]. All ants remained suspended in fixative solution prior to imaging.

4.2.2.2 Ants fed with UCNPs

From a colony of agriculturally damaging southern fire ants (Solenopsis xyloni) kept at room temperature (25^oC) and in a 12:12 h Light:Dark cycle, in the Entomology Laboratory, at California State University, Fresno, CA, individuals were extracted for experimentation. Isolated southern fire ants were fed with a 10% honey-water + UCNPs solution and then placed in polystyrene boxes with sides covered with fluon to avoid their scape. After feeding with UCNPs and proior to experiment, the ants were returned to the individual containers for 24 hours before being fixed with Kahle's solution. The Kahle's solution was prepared by mixing (6 mL formaldehyde, 15 mL 95% ethanol, 2 mL glacial acetic acid, 60 mL distilled water) as discussed in [203]. All ants remained suspended in fixative solution.

4.2.3 Particle size measurements

A transparent colloidal solution of $YVO_4 : Er^{+3}, Yb^{+3}$ nanoparticles dispersed in water was placed in a dynamic light scattering system (Malvern Instruments with 50 mW, 660 nm red laser) to determine the particle size of $YVO_4 : Er^{+3}, Yb^{+3}$ nanoparticles.

4.2.4 Side illumination laser scanning microscopy setup

UCL and high-contrast images of fire ants injected with $YVO_4 : Er^{+3}, Yb^{+3}$ UCNPs were characterized by using a home-made side illumination laser scanning microscope equipped with a 10x, NIR microscope objective with NA=0.3 as shown in (figure 4.1). The fire ants which are injected with UCNPs, placed on quartz coverslip and excited with a 980 nm laser excitation with relatively low intensity 10 $kW.cm^{-2}$. After filtering, the excitation laser with long-pass (800 nm LP) filter, the up-conversion fluorescence was collected through the same microscope objective and analyzed with a homemade spectrometer equipped with a starlight camera (Trius camera model SX-674). Furthermore, high-contrast images were collected by a photon counter (Hamamatsu photon counter model number H7155-21).

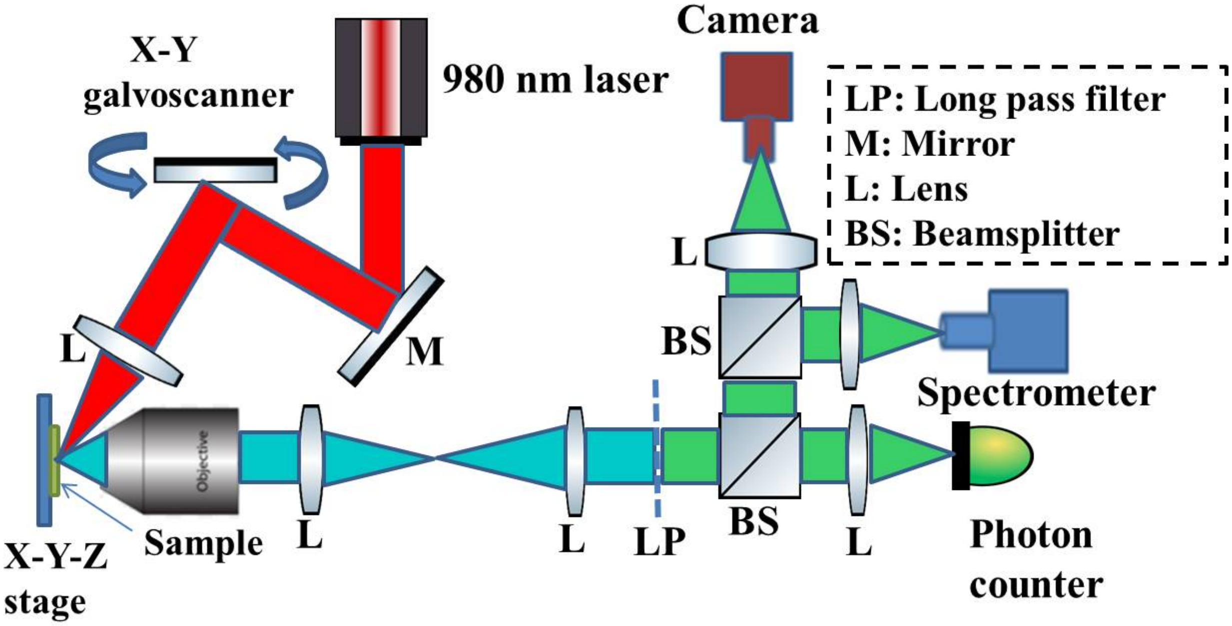

Figure 4.1: A homemade side illumination wide-field laser scanning microscope setup consisting of a 4f imaging system, a demaginification 4f system composed of a CCD camera, a photon counter, and a spectrometer. Red arrow indicates the optical path for laser illumination, and green arrows indicate for fluorescence emission.

4.3 Results and Discussion

4.3.1 Upconversion nanoparticles $YVO_4 : Er^{+3}, Yb^{+3}$ emission

Upconversion luminescence in lanthanides can be interpreted based on three main mechanisms: Excited State Absorption (ESA), Energy Transfer Upconversion (ETU), and Photon Avalanche (PA) [139]. Here, we only consider ETU. For this we use ytterbium ion (Yb^{+3}) as a sensitizer and choose the erbium ion (Er^{+3}) as the activator (reaccepter) for two reasons: (i) Er^{+3} ions can efficiently create upconversion fluorescence in the visible and near-infrared, but their absorption at the 980 nm excitation wavelength is relatively weak [147], and (ii) the Yb^{+3} ion has a very high absorption cross section at 980 nm, and can efficiently transfer its excitation to Er^{+3} ion [139] using the ETU process. The ETU between Yb^{+3} ions and Er^{+3} ions occurs according to the following transition:

$$({}^4I_{15/2}Er^{+3}) + ({}^2F_{5/2}Yb^{+3}) \longrightarrow ({}^4I_{11/2}Er^{+3}) + ({}^2F_{7/2}Yb^{+3}) \tag{4.1}$$

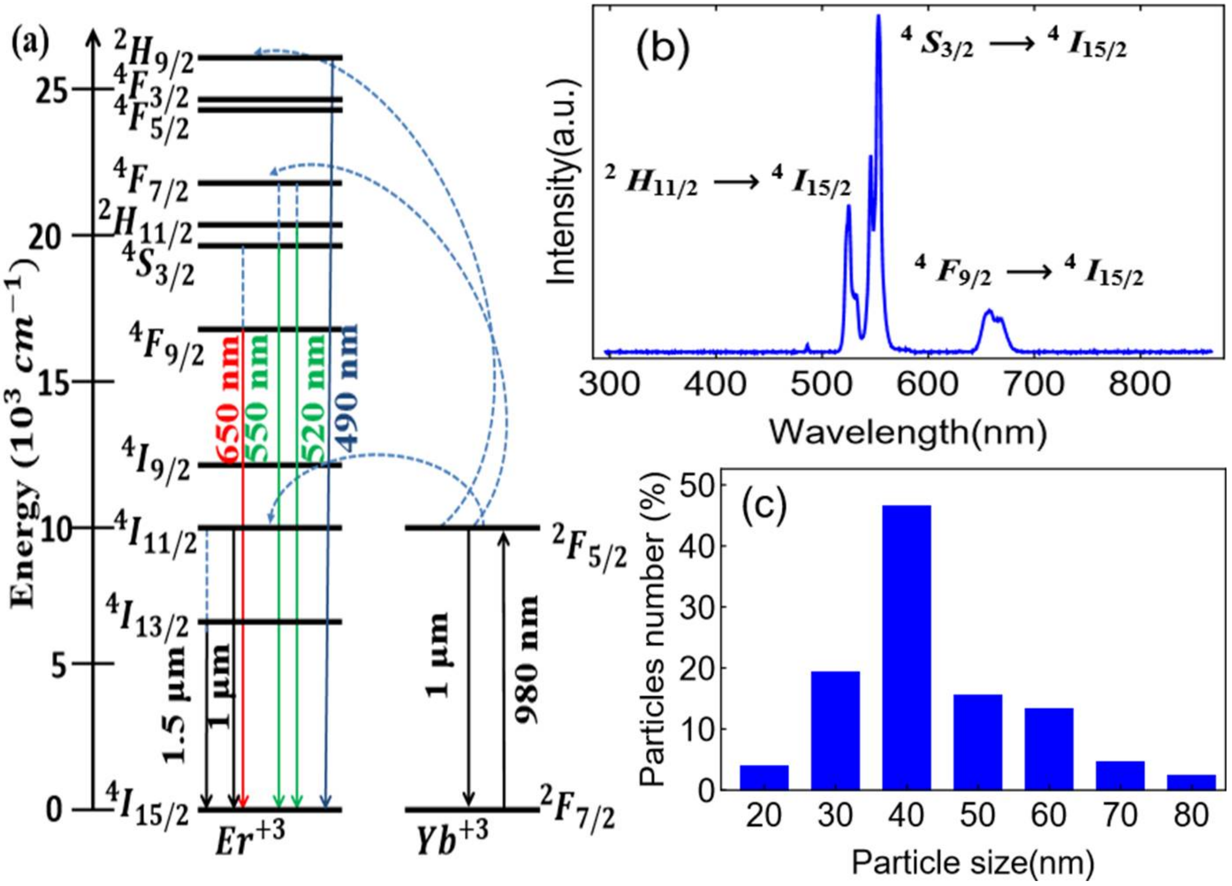

Figure 4.2: (a) Energy transfer mechanism between Er^{+3} and Yb^{+3}. Curved dashed, straight dashed and full arrows represent energy transfer, multi-phonon relaxation, and radiative emission process, respectively. (b) Luminescence emission spectrum of $YVO_4 : Er^{+3}, Yb^{+3}$ under 980 nm excitation. (c) Size distribution of the UCNPs measured by dynamic light scattering (DLS).

Consequently, as shown in Figure 4.2(a), the Yb^{+3} ion absorbs the first NIR photon of 980 nm laser to the (${}^2F_{5/2}$) Yb^{+3} excited state. The energy transfer from the (${}^2F_{5/2}$) Yb^{+3} excited state promotes $Er^{+3}$to its quasi-resonance metastable state${}^4I_{11/2}$. A second NIR photon absorption re-excites the Yb^{+3} back to the (${}^2F_{5/2}$) Yb^{+3} excited state and energy transfer further excites the

Er^{+3} ($^4I_{11/2}$) metastable state to a highly excited ($^4F_{7/2}$) Er^{+3} state. This state then relaxes to ($^2H_{11/2}$, $^4S_{3/2}$, and $^4F_{9/2}$) Er^{+3} states via the multi-phonon relaxations. Subsequent radiative transitions then occur to the ground state $^4I_{15/2}$ according to the transitions: $^2H_{11/2}\longrightarrow {}^4I_{15/2}$, $^4S_{3/2}\longrightarrow {}^4I_{15/2}$, and $^4F_{9/2} \longrightarrow {}^4I_{15/2}$, which give green (520 nm and 550 nm) and red (650 nm) emissions; respectively, as shown in Figure 4.2(b) [148].

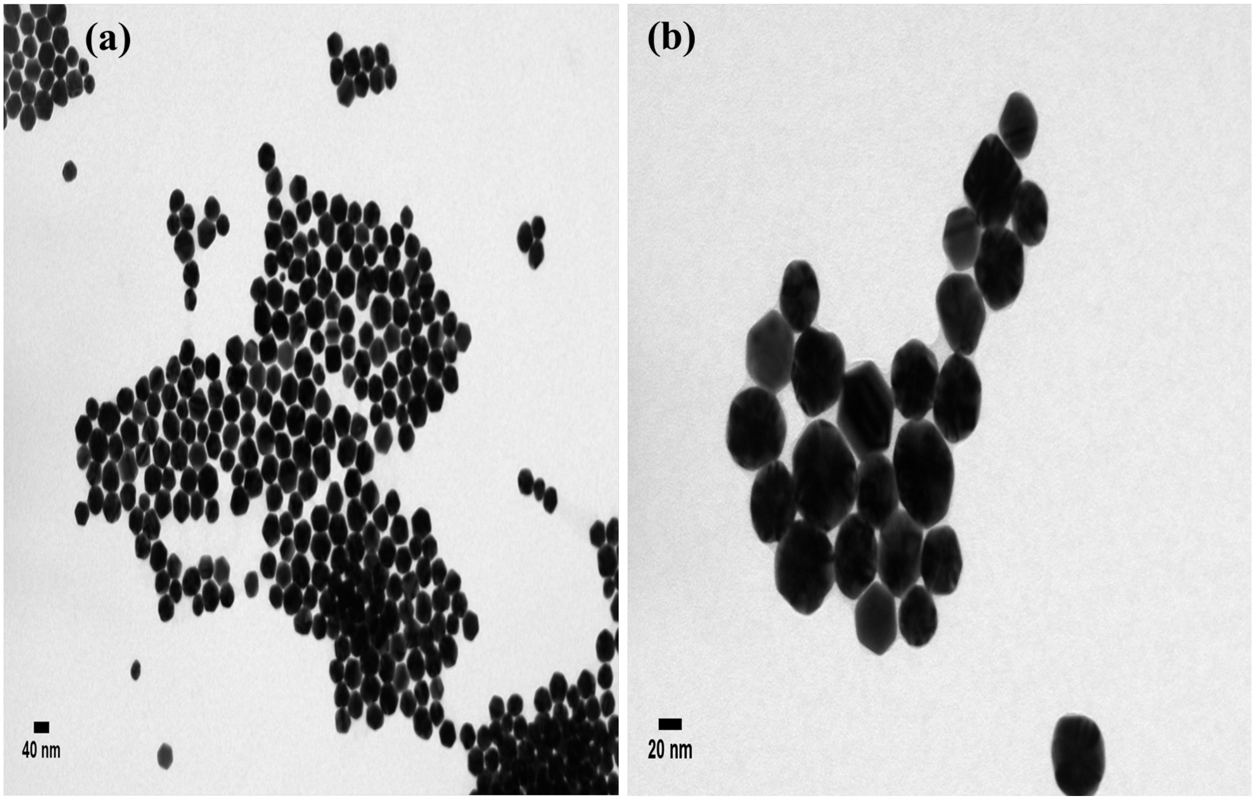

Figure 4.3: TEM images of $YVO_4 : Er^{+3}, Yb^{+3}$ nanoparticles dispersed in water and dried on a micro grid.

4.3.2 Upconversion nanoparticles $YVO_4 : Er^{+3}, Yb^{+3}$ size measurement and TEM images

Particles size is important in bio-fluorescent probes, especially for cellular level applications. It is very challenging to fabricate ultra-small nanoparticles due to Oswald ripening, which is the transfer of nanoparticles over time from smaller, less stable particles to larger ones [204] during high-temperature annealing in the synthesis processes. Indeed, we were able to overcome this challenge, building on the results of reference [148], as explained in the synthesis procedure section. Figure 4.2(c) shows that the average size of the stable colloidal solution of $YVO_4 : 2\%Er^{+3}, 20\%Yb^{+3}$ peaks at 40 nm with standard deviation of 18 nm. Furthermore, in order to visualize the morphology of our nanoparticles, we performed TEM images of the UCNPs. Low-magnification TEM images of the nanoparticles dispersed in water are shown in Figure 4.3(a) and have 40nm average size which agrees with the DLS particle size measurement as shown in Figure 4.2(c). High resolution TEM images indicated that $YVO_4 : Er^{+3}, Yb^{+3}$ nanoparticles are crystallized very well and expected to have strong luminescence properties as shown in Figure 4.3(b).

4.3.3 High-contrast 2D scanning images of fire ants injected with $YVO_4 : Er^{+3}, Yb^{+3}$ nanoparticles

After injecting fire ants with $YVO_4 : Er^{+3}, Yb^{+3}$ UCNPs, the ants were investigated by a home-made side illumination laser scanning microscopy equipped with a photon counter under a continuous wave CW 980 nm laser with relatively low intensity $10kW.cm^{-2}$. We performed 2D scanning over the entire body of two ants injected with $YVO_4 : Er^{+3}, Yb^{+3}$ UCNPs. Our aim was to investigate the possibility of obtaining high-contrast images with upconversion nanoparticles inside the body of small insects. Figure 4.4(a) and 4.4(b) show high-contrast images (red color) without autofluorescence of the ant's body under 980 nm laser illumination. In contrast, scanning the ants with green illumination, seen as light blue in the Figure 4.4(a) and 4.4(b), produced high autofluorescence of the ants due to biological tissue's high absorption at the visible wavelengths [205] and subsequent reemission at longer wavelengths. Furthermore, the fluorescence spectrum was taken from each 980 nm laser illumination point in the 2D scan in order to emphasize that we saw only the UCNPs's up-conversion emission from IR excitation, and no autofluorescence. This is shown in (Figure 4.4(c) and 4.4(d)) where the $YVO_4 : Er^{+3}, Yb^{+3}$ UCNPs display a clear UCL consisting of two main emission bands: strong green luminescence emission spectra corresponding to ${}^2H_{11/2} \longrightarrow {}^4I_{15/2}$ and ${}^4S_{3/2} \longrightarrow {}^4I_{15/2}$ transitions and weak red luminescence emission spectrum corresponding to ${}^4F_{9/2} \longrightarrow {}^4I_{15/2}$ transition [148].

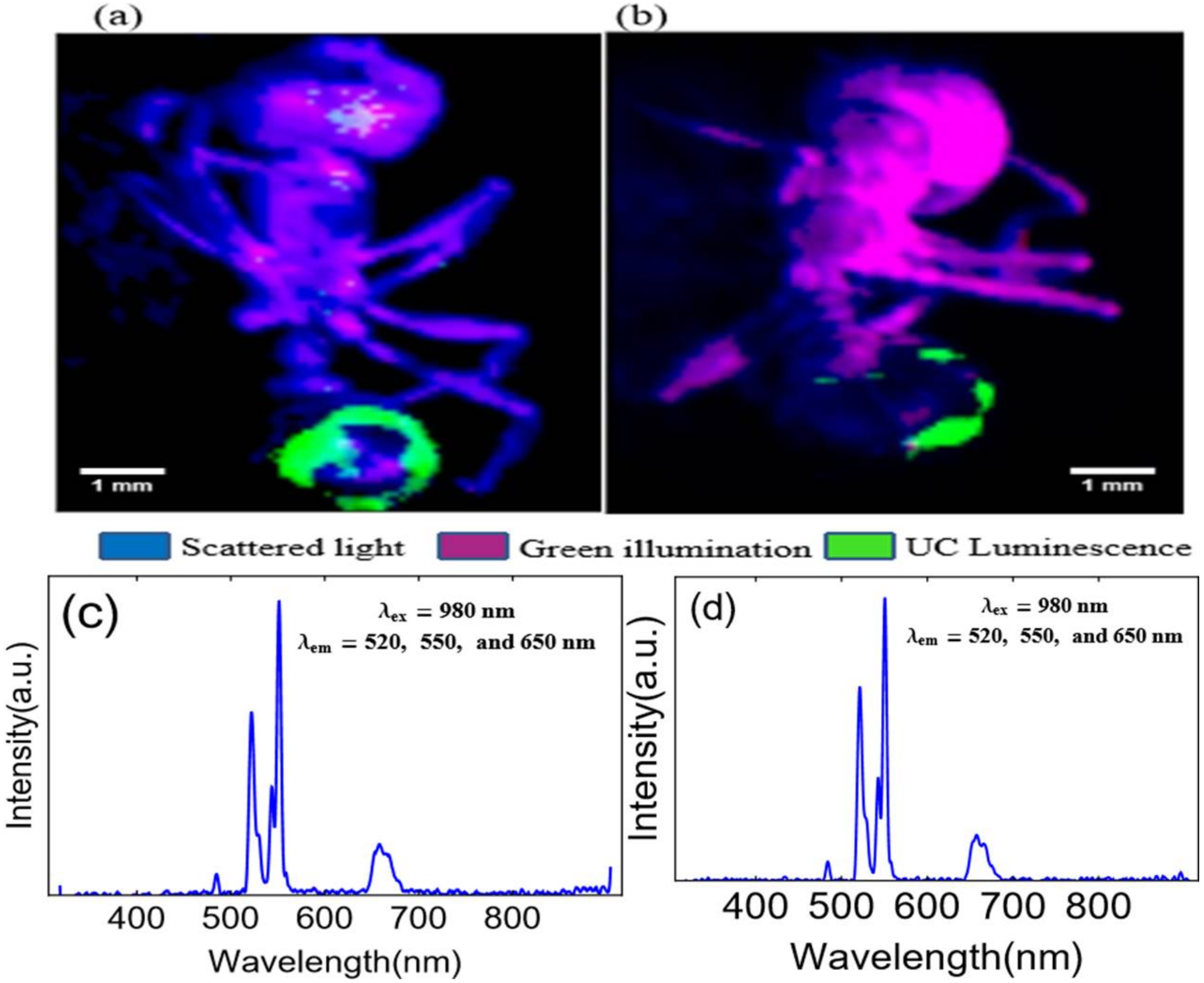

Figure 4.4: (a) and (b) Superimposed images of the whole-body of two different fire ants injected with of $YVO_4 : Er^{+3}, Yb^{+3}$ UCNPs and illuminated by white light (blue color), green laser (light blue color), and infrared at 980 nm (red color). These images were scanned by a 2D galvoscanner and emitted light collected by a photon counter. (c&d) Up-conversion luminescence emission spectra of the $YVO_4 : Er^{+3}, Yb^{+3}$ UCNPs found in red color positions (under 980 nm illumination) in the $ants$ images a and b, respectively.

4.3.4 Detection of $YVO_4 : Er^{+3}, Yb^{+3}$ UCNPs up-conversion luminescence by a colored CCD camera under green and NIR illuminations

In this section, we chose one of the fire ants injected with $YVO_4 : Er^{+3}, Yb^{+3}$ UCNPs to study the UCL and image contrast using a wide field (camera) detector. Similarly, fluorescence excited by both infrared and green illumination were viewed by the same UCL imaging system as shown in (Figure 4.1) in the Experimental Methods section. Figures 4.5(a) and 4.5(b) show clear and strong up-conversion luminescence by 980 nm laser with a high signal-to-noise ratio and lasting photostability even for long exposure times. As seen under 980 nm laser illumination, there is no background fluorescence. As discussed above, the clear signal under 980 illumination and lack of autofluorescence in the spectrum in (Figures 4.5(a) and 4.5(c)) are attributed to two main reasons: (i) low absorption by biological samples at the NIR laser wavelength and (ii) high photostability of $YVO_4 : Er^{+3}, Yb^{+3}$ UCNPs in water. In contrast, Figures 4.5(b) and 4.5(d) show low contrast images and a fluorescence spectrum dominated by strong background fluorescence from chemical compounds present in the ants, which could also be excited by the green illumination; additionally, biological samples have absorption and scattering at the visible wavelength spectrum [205].

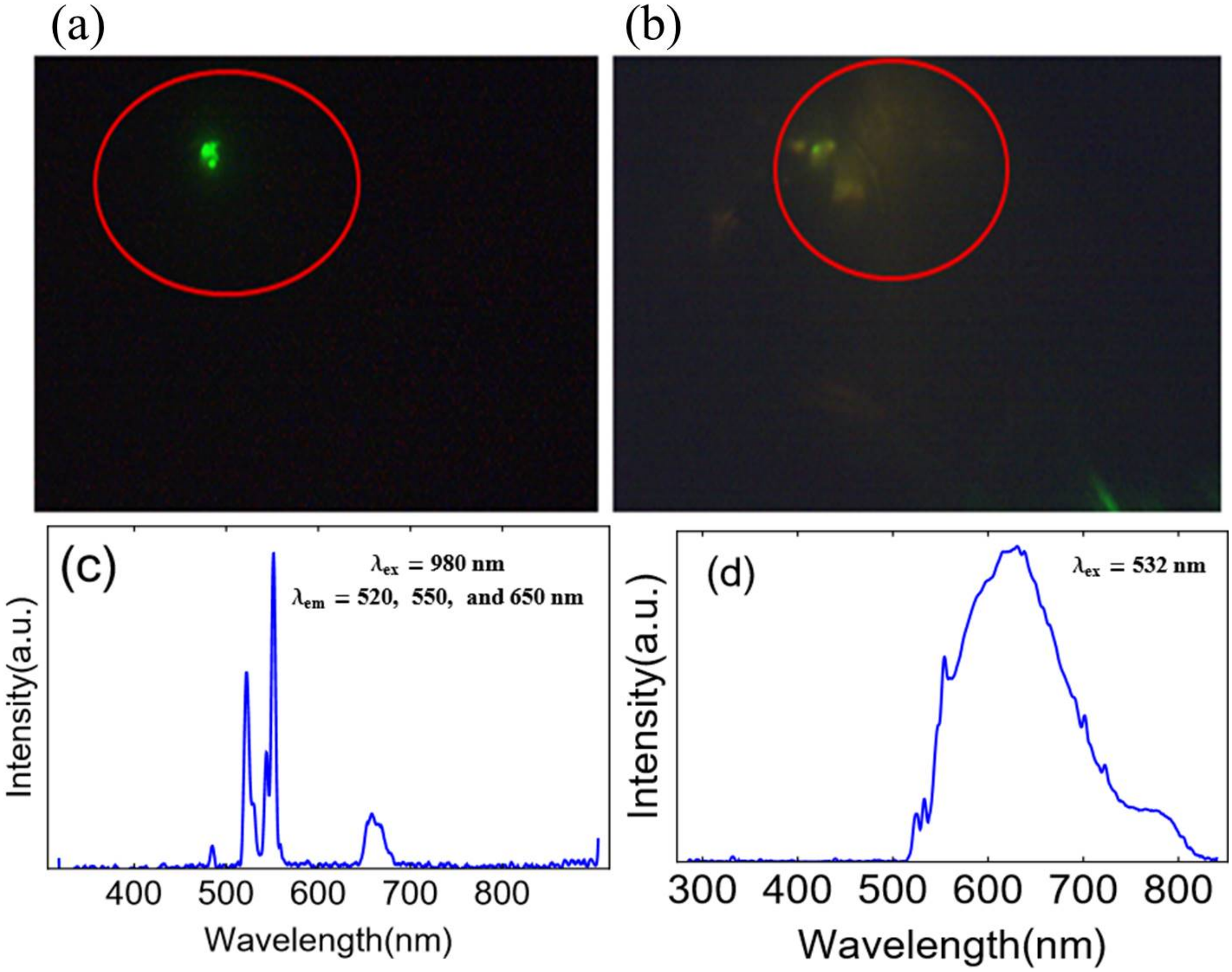

Figure 4.5: (a) and (b) comparison between up-conversion luminescence imaging contrast of the same fire ant injected by $YVO_4 : Er^{+3}, Yb^{+3}$ UCNPs under 980 nm and green (532 nm) lasers illumination. Figures 4.5(c) and 4.5(d) The corresponding up-conversion luminescence emission with high signal-to-noise ratio and low autofluorescence from the ant's body under 980 nm laser excitation and high autofluorescence spectra under 532 nm green illumination, respectively.

4.3.5 Strong and stable up-conversion luminescence of $YVO_4 : Er^{+3}, Yb^{+3}$ nanoparticles injected into fire ants under continuous NIR illumination

In this section, we investigated the photostability of $YVO_4 : Er^{+3}, Yb^{+3}$ UCNPs injected into the bodies of two ants under continuous 980 nm laser. Figure 6 shows high UCL with a high signal-to-noise ratio, lasting photostability, no bleaching, and no damage to the biological samples. These images were recorded by a color CCD camera (Trius camera model SX-674) in order to observe the green fluorescence emission directly during the illumination process. The inserts in Figures 4.6(c) and 4.6(d) illustrate the photo luminescence (PL) of the UCNPs in the green spots.

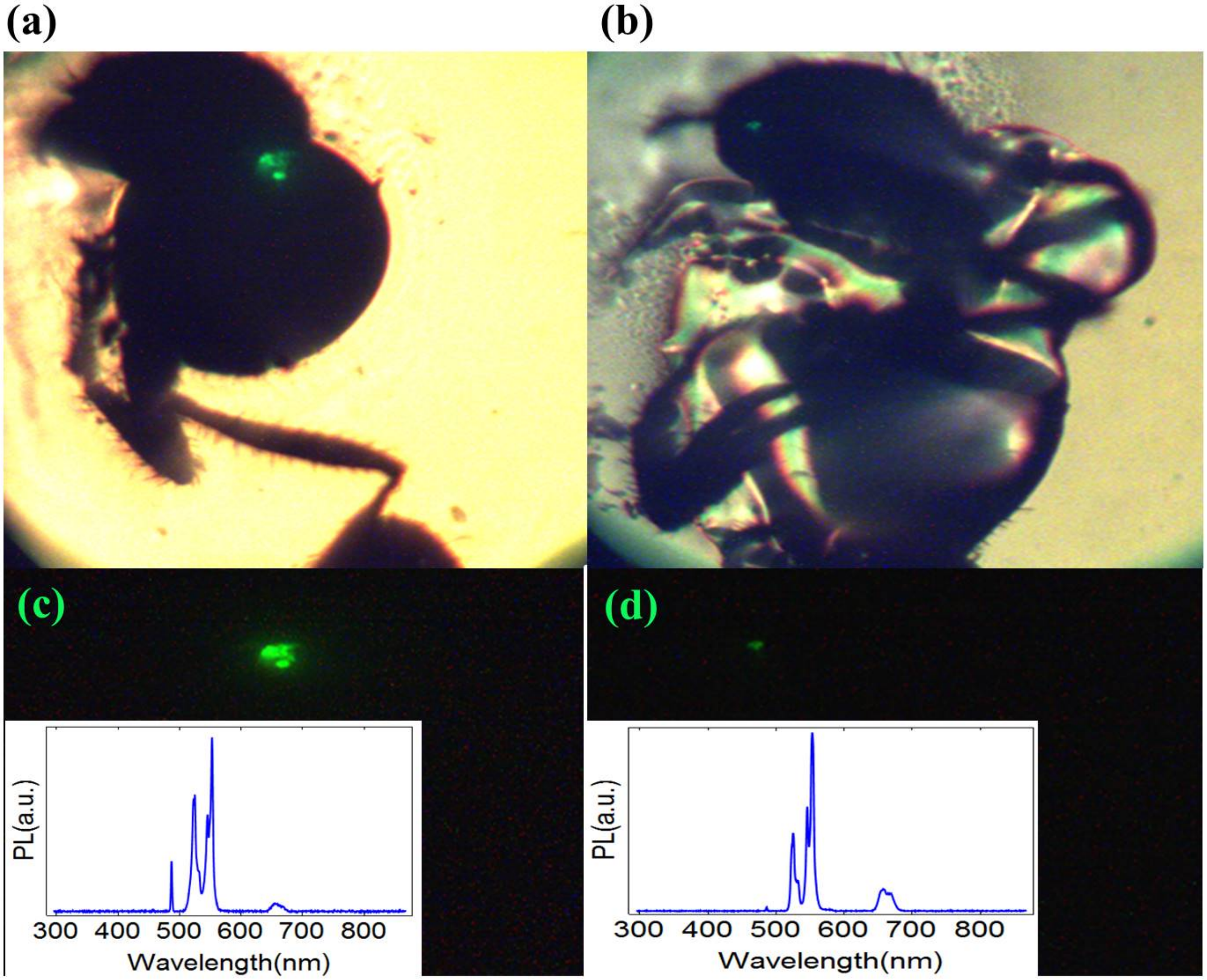

Figure 4.6: (a) and (b) up-conversion luminescence imaging of two different fire ants injected by $YVO_4 : Er^{+3}, Yb^{+3}$ UCNPs under 980 nm laser illumination and with white light back illumination in order to observe the UCL directly from the ants's bodies. Figures 4.6(c) and 4.6(d) The corresponding up-conversion fluorescence emission with high signal-to-noise ratios from the two different ants are shown in (a) and (b), respectively. The inserts present the photo luminescence (PL) of the UCNPs in the green spots which are shown in (c) and (d).

4.3.6 Optical imaging of fire ants fed with $YVO_4 : Er^{+3}, Yb^{+3}$ upconversion nanoparticles

The primary goal of this section is to obtain high-contrast images of $YVO_4 : Er^{+3}, Yb^{+3}$ upconversion nanoparticles as bio-probe inside fire ants using economical and homemade optical system. From a laboratory colony of southern fire ants (Solenopsis xyloni), several individuals were extracted, isolated and fed with $YVO_4 : Er^{+3}, Yb^{+3}$ upconversion nanoparticles as explained in detail in the Methods section. Optical images of the fire ants were carried out by using a homemade side illumination laser scanning microscope. The fire ant specimens were placed on a glass coverslip on top of 10x, NA=0.26 mitutoyo microscope objective, where they were excited with a 980nm laser illumination source filtered by a short-pass filter (800 SP). The laser intensity was 8 $kW.cm^{-2}$. High contrast images of $YVO_4 : Er^{+3}, Yb^{+3}$ upconversion nanoparticles (red spots) inside the mouth of fire ants as shown in Figures 4.7(a) and 4.7(b) where scanned by a 2D-galvoscanner at scan rate (100 Hz) over (5mmX5mm) area and recorded using a photon counter (Hamamatsu photon counter model number H7155-21). Noted that we conducted characterization as soon as we fed the ants such that most particles were expected to be in the head area especially in the ant's mouth and started to enter into the body. We have observed using tomography in our recent studies [206] that NPs entered mealworm and were quickly transferred through their guts. In this study we wanted to see if the laser system works on insects, fire ants which have hard shell and complicated geometry of their heads which behave as a lens and pose challenges for the laser beam to focus and penetrate into the body .So we didn't carry on extended study of particles transfer into ants. The evidence of nanoparticles (chemical state) inside the body was proven by the tomography images shown in Figure 8. Furthermore, the effects of NPs on ants would be done to observe how insects behave once they were fed with NPs. Since this work focuses on the feasibility of the laser system, our goal (desire) is to see the particles through their body shells, in particular their head shells that are hard and thicker than other part of the body. Furthermore,we performed a signal to noise ratio (SNR) measurements during scanning the fire ants samples with 980 nm laser , and then found the SNR ratio is about(250/k.counts signal from the nanoparticles to 10/ k.counts from the fire ant body). We can attribute this high contrast images to the excellent quality of well crystallized nanoparticles which reveal strong upconversion luminescence, non-photobleaching, and non-blinking in water-based biological samples such as fire ants. The laser intensity was 8 $kW.cm^{-2}$ which might be considered unsafe for biological samples including insect. However, we didn't see any damage to the ant samples. Our experiment was carried out rather quickly and ants didn't show any damages or burning on their bodies after scanning with this specific laser power. Figures 4.7(a,inset) and 4.7(b,inset) presents a strong and clear upconversion luminescence (UCL) spectra with high signal to noise ratio of $YVO_4 : Er^{+3}, Yb^{+3}$ UCNPs in which the emission bands reveal strong green luminescence emission and weak red emission spectra corresponding to the erbium (Er^{+3}) radiative transitions form ($^2H_{11/2}$,$^4S_{3/2}$,and $^4F_{9/2}$) excited states to $^4I_{15/2}$ ground state. Interestingly, the upconversion luminescence spectra appeared to be slightly different, even though they are accumulated from the same particles, the size of the ants are not identical. This change could be attributed to the upconversion nanoparticles's temperature sensitivity, where UCNPs have been used in optical temperature sensing [153,207]. Especially, temperature in biological sample can be measured by calculating the ratio of (520 nm and 550 nm emission peaks) of UCNPs doped with erbium and using Boltzmann distribution [155].$YVO_4 : Er^{+3}, Yb^{+3}$ UCNPs can be used to accomplish fast and cheap optical bio-imaging whose absolute accuracy can be directly validated with x-ray imaging when desired.

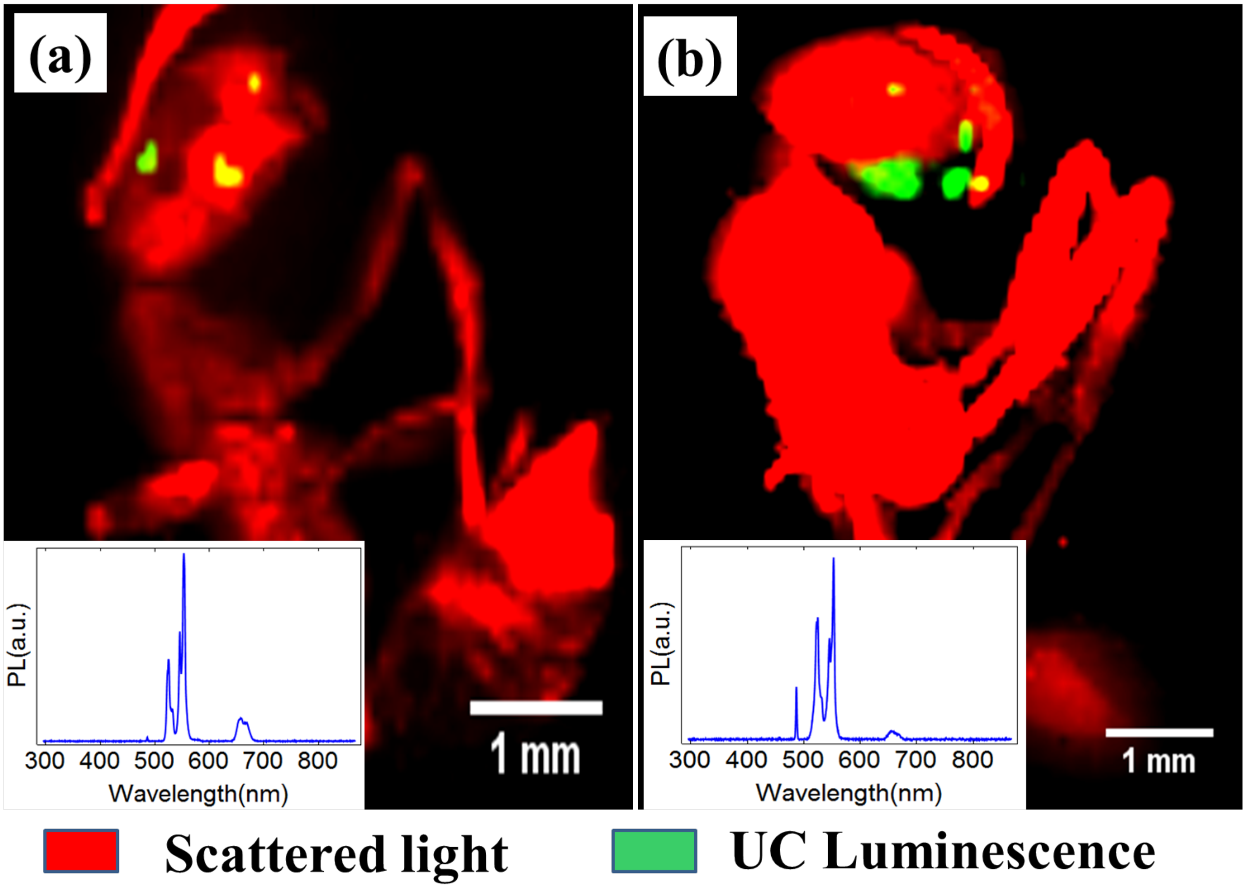

Figure 4.7: (a) and (b) Upconversion imaging of fire ants fed with $YVO_4 : Er^{+3}, Yb^{+3}$ nanoparticles. These high contrast images were scanned by a 2D galvoscanner and emitted light collected by a photon counter. The inset presents photo luminescence (PL) spectra of the UCNPs in the green spots.

4.3.7 Conformation of imaging $YVO_4 : Er^{+3}, Yb^{+3}$ upconversion nanoparticles inside fire ants using synchrotron radiation micro X-ray computed tomography (SR-μXCT)

After achieving high contrast images of the UCNPs inside fire ants using an optical system, it was necessary to confirm that the nanoparticles are actually inside the body of the fire ants. Two fires ants from the same colony of southern fire ants were extracted and scanned using synchrotron radiation micro X-ray computed tomography (SR-μXCT). Details about this technique have been reported in our previous work [202, 206]. The locations of the upconversion nanoparticles inside the fire ants's body were confirmed by performing three dimensional X-ray imaging. The distribution of lanthanide-doped yttrium($YVO_4 : Er^{+3}, Yb^{+3}$ nanoparticles) within buccal cavity and anterior end of the digestive tract of the ant were segmented and marked in red as shown in Figures 4.8(a) and 4.8(b).

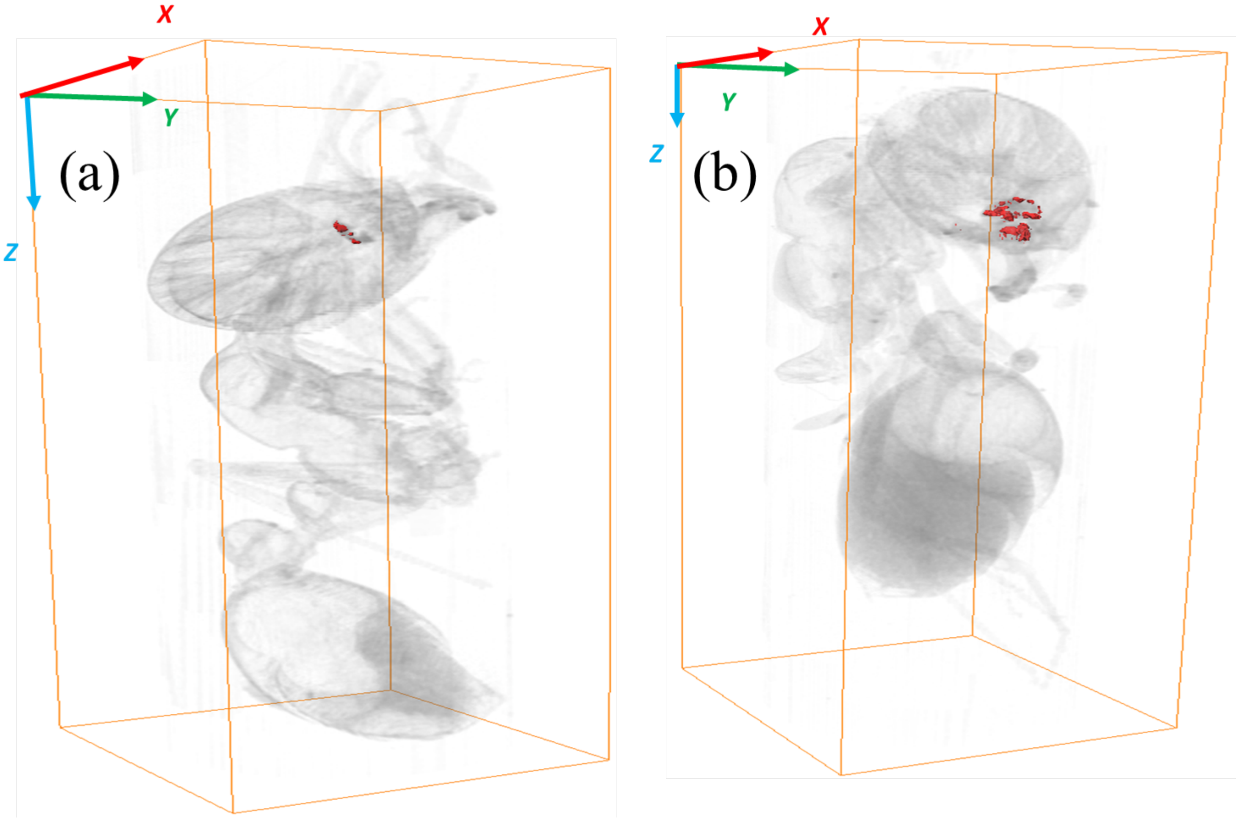

Figure 4.8: (a) and (b). Three dimensional X-ray imaging of UCNPs inside two fire ants. The UCNPs inside the ants's body ants's mouths are segmented and marked in red. The size of frame box is 1.15 x 1.09 x 3.08 mm.

4.4 Conclusion

In this work, high quality $YVO_4 : Er^{+3}, Yb^{+3}$ nanoparticles were used as a bio-fluorescent probe in fire ants. We imaged UCNPs inside the red imported fire ants (Solenopsis invicta) which have small and special body geometry that behaves as a spherical lens. Imaging a small and spherical body like an ant is a very difficult and challenging task using a confocal microscope. To overcome this problem, we designed a homemade wide field side illumination microscopy setup. As a result, we were able to see clear images as shown in (Figures 4.4 and 4.7). We detected a strong up-conversion luminescence (UCL) with high signal-to-noise ratio, and photostable UCL for a long exposure time without damaging the ants's bodies under NIR laser excitation. We succeed in distinguishably mapping the UCNPs nanoparticles inside the ant's body. In conclusion, we showed that $YVO_4 : Er^{+3}, Yb^{+3}$ nanoparticles are one of the best candidates for bio-imaging in small insect applications.

5. ENGINEERING WATER TOLERANT CORE/SHELL UPCONVERSION NANOPARTICLES FOR OPTICAL TEMPERATURE SENSING*

5.1 Introduction

Nanoscale luminescence thermometry based on thermally driven changes in fluorescence lifetimes or intensities in biological tissues has attracted great attention using nitrogen vacancy in diamond (NV) [14, 87], quantum dots (QDs) [208], gold nanoparticles (GNP) [209], and fluorescent organic dyes [9]. These fluorescent markers exhibit high luminescence efficiency; thermal sensitivity reaches millie-kelvin (mK) in living cells, especially for the NV color center in diamond [10, 14, 210, 211]. However, the application of NV center in diamond, QDs, organic dyes, and GNP fluorescent thermometers in biological models is limited by the biological tissue autofluorescence which overlaps with their fluorescence, resulting in a significant background that reduces sensitivity in deep tissue temperature sensing [196]. Furthermore, most of the organic dyes, quantum dots, and GNPs are limited by toxicity, photobleaching, blinking, and environmental sensitivity, especially for the GNPs [198, 199].

To address all the above drawbacks, upconversion nanoparticles (UCNPs) are of particular interest for optical temperature sensing [153–156]. Temperature sensing in UCNPs is usually based on the fluorescence intensity ratio (FIR) of two transitions from two (thermally-coupled) electronic energy levels to the ground state level at the thermal equilibrium [156]. The FIR method is independent of signal losses and any possible excitation intensity fluctuations that might affect accurate temperature measurements [154].

Typically, UCNPs doped with lanthanide ions, use Ytterbium (Yb^{+3}) as a sensitizer due its infrared large absorption cross section to ensure high upconversion efficiency of upconverting ions such as Ln^{+3} (Ln=Er,Tm,Ho,etc.) [29, 163]. The Upconversion process in UCNPs is a nonlinear photoexcitation process where the sensitizer ions absorb NIR photons and sequentially transfer ab-

---

[*] Reprinted with permission from Engineering water-tolerant core/shell upconversion nanoparticles for optical temperature sensing by Masfer H Alkahtani, Carmen L Gomes, and Philip R Hemmer, 2017. Optics Letter, vol. 42, pp. 2451-2454, Copyright [2017] by the Optical Society of America (OSA)

sorbed energy to the activators which promotes them to higher excited states and eventually leads to radiative emission in ultraviolet, visible, and NIR regions [212–214]. Unfortunately, the conventional UCNPs-sensitizer (Yb^{+3}) has only one absorption band centered at 980 nm wavelength which largely overlaps with the absorption band of water molecules that are dominant in biological samples as shown in Figure 5.1. Therefore, triggering the upconversion process in UCNPs with 980 nm laser excitation would significantly cause overheating issues that might result in cell death, tissue damage, and inaccurate thermal reading during temperature sensing [164]. Interestingly, Neodymium (Nd^{+3}) has shown high efficiency energy transfer to Yb^{+3} in addition to a large absorption cross section at 808 nm where the water absorption is too low compared to the water absorption at 980 nm as shown in Figure 5.1 [165]. However, the introduction of (Nd^{+3}) as new sensitizer directly into UCNPs nanoparticles quenches their upconversion luminescence dramatically due to the deleterious energy transfer (ET) between the new sensitizer Nd^{+3} and the activator Er^{+3}, respectively [29] .

To overcome this issue, an engineering core/shell structure is necessary where the new sensitizer Nd^{+3} is doped with the Yb^{+3} in the shell and the activator Er^{+3} is doped with Yb^{+3} in the core to avoid such ET processes [166]. The upconversion process in the new core/shell combination occurs when the new sensitizer Nd^{+3} ion absorbs NIR photons and transfers energy to the nearby Ytterbium Yb^{+3} ion; and then Yb^{+3} ion transfers the NIR photons to the activator (Er^{+3}) ion, where the UC process is expected to take place. Specifically, the most commonly used $NaYF_4 : Yb^{+3}, Er^{+3}@Nd^{+3}$ UCNPs were synthesized in a core/shell structure and showed to be the best UCNPs generation for biological imaging and thermometry. However, these UCNPs suffer from very low quantum efficiency when dispersed in water, especially at small particle sizes as reported in [29, 153, 164]. Recently, $YVO_4 : Er^{+3}, Yb^{+3}$ UCNPs have shown high efficiency upconversion luminescence at the single-particle level when dispersed in water [148] as well as high contrast imaging in biological models [28].

In this work, we introduce Nd^{+3} into $YVO_4 : Er^{+3}, Yb^{+3}$ nanoparticles in a core/shell structure, which provide efficient luminescent markers at a biocompatible illumination wavelength for optical temperature sensing in living organisms.

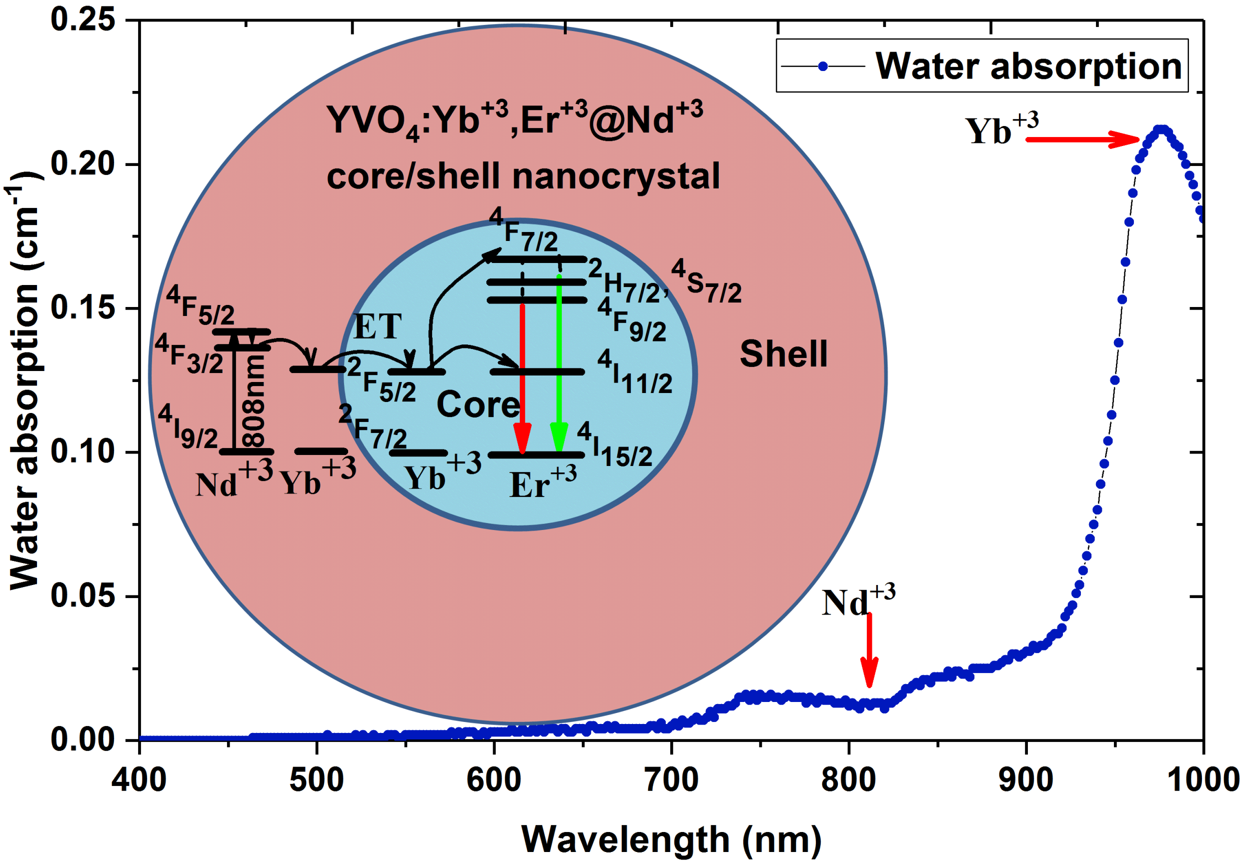

Figure 5.1: An absorption spectrum of distilled water (DI water) taken over the visible and the near-infrared (NIR) range. The red arrows indicate the lower and higher water absorption bands, where the alternative excitation bands should be extended to avoid biological tissues overheating by introducing Nd^{+3} as a new sensitizer into the UCNPs instead of the conventional sensitizer (Yb^{+3}) of the UCNPs. Inset: Schematic design and energy transfer processes between Nd^{+3} , Yb^{+3} , and Er^{+3} of a core/shell nanoparticles (photon upconversion) under 808 nm laser excitation.

5.2 Experimental methods

Experimentally, we chose YVO_4 as a host material because of its high upconversion eficiency and photostability in water as reported in [148, 162]. As a proof of principle in this experiment, we synthesized two samples following the original hydrothermal synthesis routes reported in [148, 161] as follows: In sample 1, we doped Nd^{+3} directly into $YVO_4 : Er^{+3}, Yb^{+3}$

at $20\%, 2\%, 0.5\%$ doping ratios of nanoparticles, respectively, where x=0.5% is the optimum concentration of Nd^{+3} in UCNPs as discussed in [215]. In Sample 2, we designed the core/shell nanoparticles by preparing the core nanoparticles $YVO_4 : Er^{+3}, Yb^{+3}$ (20%, 2%), and then Nd^{+3} was introduced by overgrowing a shell layer of $YVO_4 : Yb^{+3}, Nd^{+3}$ with at (Yb^{+3} 10%, Nd^{+3} 10%) doping ratio on the core NPs as shown in Figure5.1(inset).The concentrations of Yb^{+3} and Nd^{+3} in the shell layer were carefully chosen based on the optimal doping ratio reported in [29]. Finally, the core/shell $YVO_4 : Er^{+3}, Yb^{+3}@Nd^{+3}$ NPs were obtained. Figure 5.2(a), shows a high magnification TEM image of a droplet of (1 mg/mL) of $YVO_4 : Er^{+3}, Yb^{+3}@Nd^{+3}$ NPs core/shell nanoparticles dispersed in water and dried on TEM grid. The high resolution TEM image reveals high crystalline and non-agglomerated nanoparticles with (20 nm average size) which are expected to have strong upconversion luminescence. Also a high magnification TEM image of $YVO_4 : Er^{+3}, Yb^{+3}$ NPs core nanoparticles dispersed in water and dried on TEM grid was recorded as shown in Figure 5.2(c). The average size of the core/shell NPs was further confirmed by dynamic light scattering (DLS) as shown in Figure 5.2(b).The average size of the core nanoparticles was 17nm, and then increased to 20 nm in average, implying a shell thickness of (3-4nm).

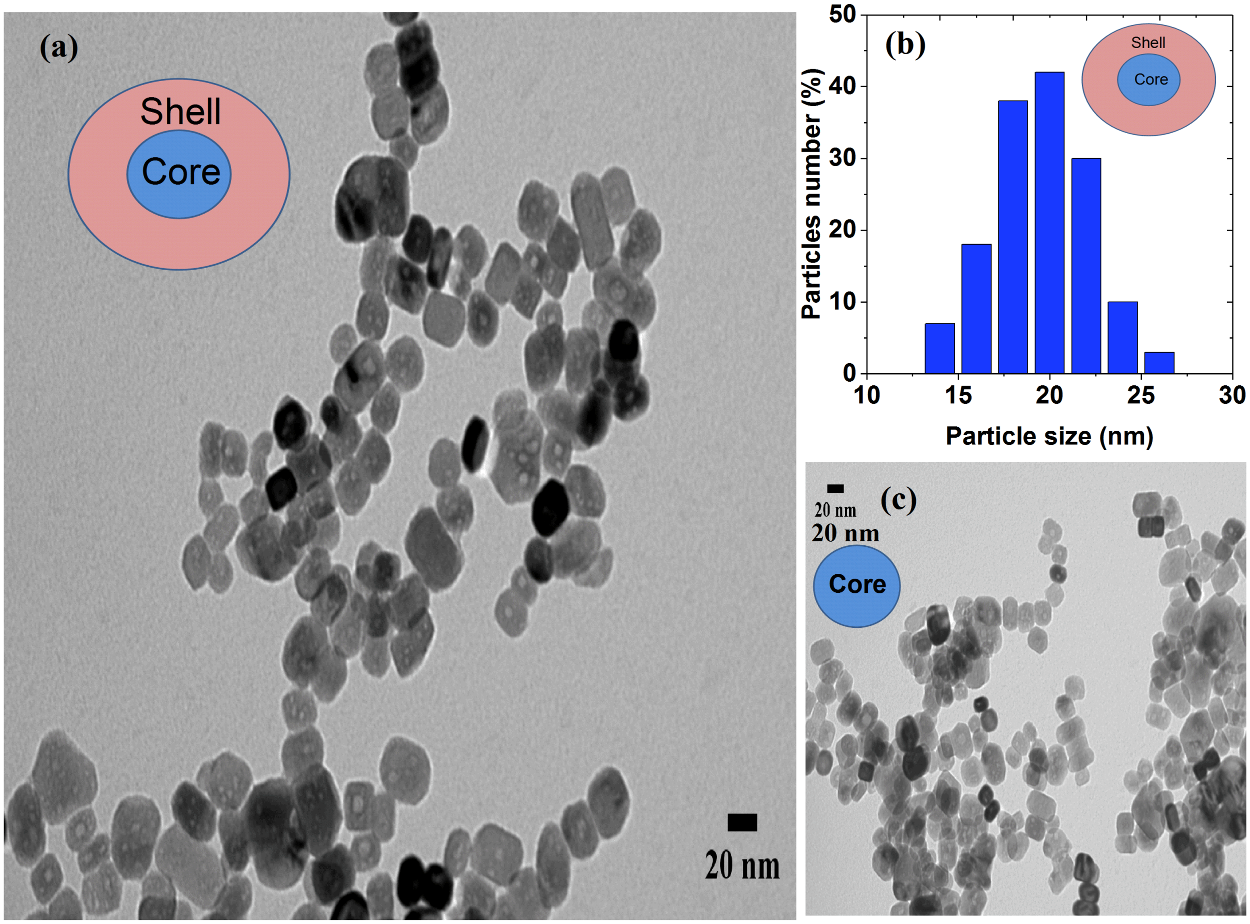

Figure 5.2: (a) A High magnification TEM image of the core/shell nanoparticles dispersed in water and dropped onto a microgrid. (b) Average size distribution of the core/shell nanoparticles recorded by DLS. (c) TEM image of the core nanoparticles dispersed in water and dried onto a microgrid.

5.3 Results and discussion

To verify the upconversion luminescence efficiency of the two samples, a thin layer of NPs of each sample was spin-coated on a piece of quartz to avoid undesired agglomerated emitters and then placed on a homemade confocal laser scanning microscope equipped with two laser diodes (808 nm and 980 nm), photon counter, and a spectrometer. Both samples were examined under two laser diodes (808 nm and 980 nm) excitations with the same power intensity (700 $mW.cm^{-2}$). The direct doping of Nd^{+3} into $YVO_4 : Er^{+3}, Yb^{+3}$ in sample 1 quenched the upconversion luminescence (UCL) of the UCNPs under 808 nm laser excitation due to the deleterious energy transfer between Nd^{+3} and Er^{+3} [29]; however, normal UCL was observed under 980 nm laser illumination as shown in Figure 5.3(a). Consequently, sample 1 has shown undesired results for this experiment and was then discarded from further analysis in this work. In contrast, Figure 5.3(b), shows that under both laser excitations, the core/shell $YVO_4 : Er^{+3}, Yb^{+3}@Nd^{+3}$ nanoparticles (sample 2) illustrates two strong green emissions at two bands (520 nm, and 550 nm), as well as weak red emission at 650 nm corresponding to these transitions ${}^2H_{11/2} \longrightarrow {}^4I_{15/2}$, ${}^4S_{3/2} \longrightarrow {}^4I_{15/2}$, and ${}^4F_{9/2} \longrightarrow {}^4I_{15/2}$ of the Er^{+3} ion. In addition, we performed power-dependent emission intensities measurements of the core/shell sample under either 808 nm or 980 nm laser excitations to verify the two-photon process in $YVO_4 : Er^{+3}, Yb^{+3}@Nd^{+3}$ core/shell NPs. Figure 5.3(b,inset), shows slope equal to 2 which indicates the two-photon upconversion process in both cases using 808 nm, and 980 nm excitation, respectively.

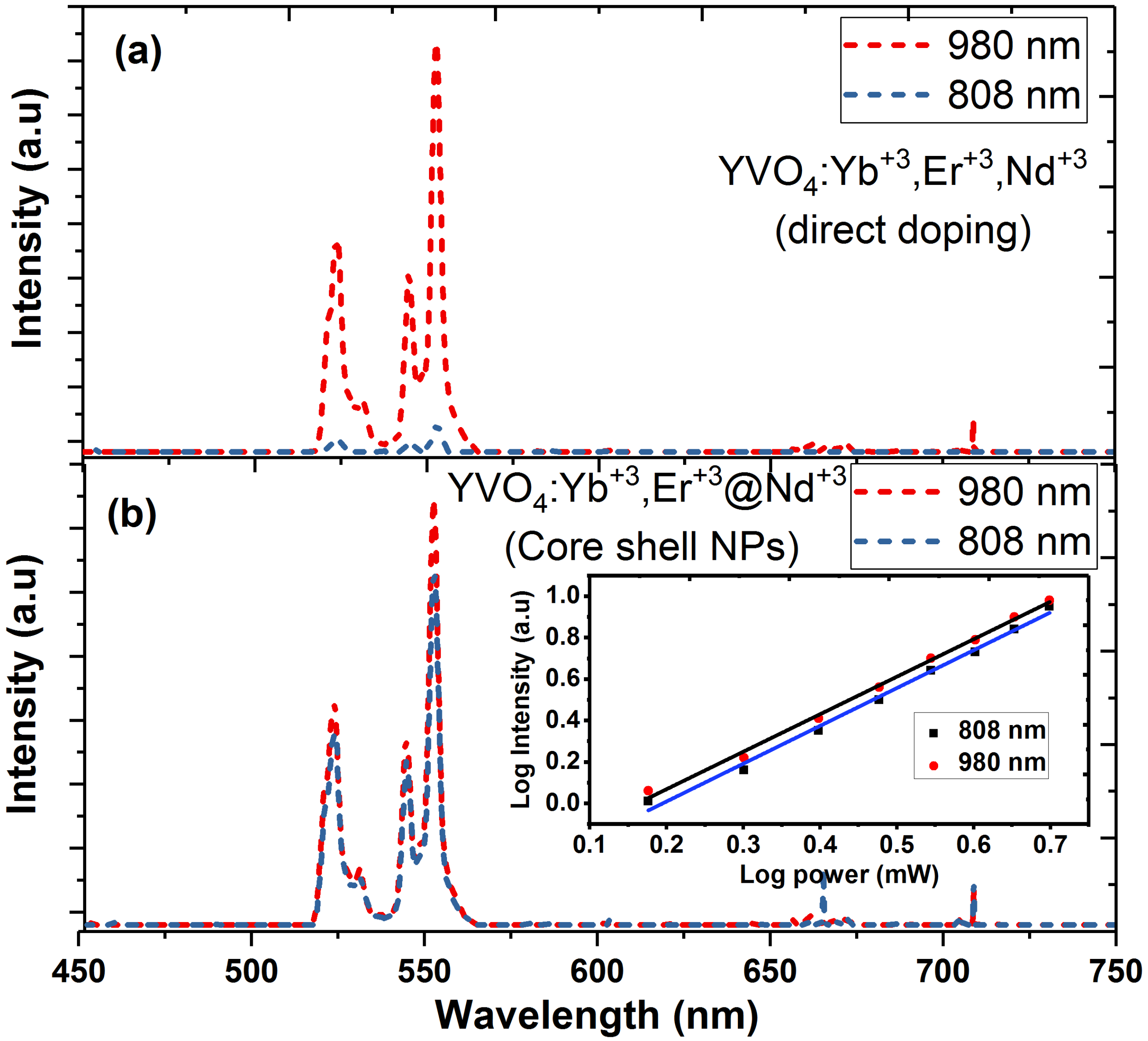

Figure 5.3: (a) upconversion luminescence emission spectra of $YVO_4 : Er^{+3}, Yb^{+3}, Nd^{+3}$ (direct doping) NPs under 808 nm and 980 nm wavelength illuminations. (b) Upconversion luminescence emission spectra of $YVO_4 : Er^{+3}, Yb^{+3}@Nd^{+3}$ core/shell NPs under 808 nm and 980 nm wavelength excitations. (b,inset), logarithmic scale of the core/shell NPs green luminescence dependence as a function of 808 nm and 980 nm excitation powers.

For further understanding of the upconversion process in the $YVO_4 : Er^{+3}, Yb^{+3}@Nd^{+3}$ core/shell NPs as shown in Figure 5.1(inset), in the shell the 808 nm laser promotes Nd^{+3} to its $^4F_{5/2}$ excited state, followed with non-radiative relaxation to $^4F_{3/2}$ state. The energy transfer populates $^2F_{5/2}$ state of nearby Yb^{+3}, and further energy transfer crosses the shell layer towards nearby Yb^{+3} in the core to populate its ${}^2F_{5/2}$ state to initiate the typical UC process in the Er^{+3}. In the core, the energy transfer from the ${}^2F_{5/2}$ excited state of Yb^{+3} promotes Er^{+3} to its ${}^4I_{11/2}$ metastable state. Sequentially, a second NIR photon absorption from the excited state of Yb^{+3} further excites the Er^{+3} to highly excited (${}^2H_{11/2}$, ${}^4S_{3/2}$, and ${}^4F_{9/2}$) Er^{+3} states via the multi-phonon relaxations. Consequently, two intensive green emissions and weak red emissions occur according to these transitions: ${}^2H_{11/2} \longrightarrow {}^4I_{15/2}$, ${}^4S_{3/2} \longrightarrow {}^4I_{15/2}$, and ${}^4F_{9/2} \longrightarrow {}^4I_{15/2}$, respectively.

The quantum yield (Q.Y) of $YVO_4 : Er^{+3}, Yb^{+3}@Nd^{+3}$ core/shell NPs (average size 20nm) as measured with respect to an infrared dye reference (IR-140) [24], is 0.91Âś0.02% under 808 nm laser excitation with power intensity (700 $mW.cm^{-2}$). The only disadvantage of $YVO_4 : Er^{+3}, Yb^{+3}@Nd^{+3}$ nanoparticles is higher saturation laser power. Compared to the best quantum yield for $NaYF_4 : Er^{+3}, Yb^{+3}$ core/shell nanoparticles (0.3%) at 30 nm size in hexane [158], $YVO_4 : Er^{+3}, Yb^{+3}@Nd^{+3}$ core/shell NPs exhibit higher Q.Y in water at small size level which makes these nanoparticles the best solution for water-based bio-applications.

Temperature dependence of upconversion emission in $YVO_4 : Er^{+3}, Yb^{+3}@Nd^{+3}$ core/shell nanoparticles was investigated over a 298 K to 315 K temperature range, as shown in Figure 5.4. Specifically, this temperature dependence can be interpreted using Boltzmann populations in two thermally coupled levels (${}^2H_{11/2}$,${}^4S_{3/2}$) in Erbium (Er^{+3}) ion. The fluorescence intensity ratio (FIR) of transitions from the ${}^2H_{11/2}$ and ${}^4S_{3/2}$ Erbium excited states to the ${}^4I_{15/2}$ Erbium ground state could be computed using equation (5.1), which is derived in detail in [216]:

$$FIR = \frac{I({}^4S_{3/2} \longrightarrow {}^4 I_{15/2})}{I({}^2H_{11/2} \longrightarrow {}^4 I_{15/2})} = \frac{g_2\sigma_2\omega_2}{g_1\sigma_1\omega_1} \exp(\frac{-\Delta E}{KT}) \tag{5.1}$$

where, g_1 and g_2 are the degeneracies of the Erbium Er^{+3} (${}^2H_{11/2}$, ${}^4S_{3/2}$) excited states, σ_1,σ_2 and ω_1,$\omega_2$are the emission cross-sections and the fluorescence frequencies of ${}^2H_{11/2}$,${}^4S_{3/2} \longrightarrow {}^4I_{15/2}$ transitions, respectively; T is the temperature, and k is the BoltzmannâĂŹs constant; ΔE is the energy gap of two thermally coupled energy levels. To simplify, equation (5.1) can be expressed as follows:

$$\ln(FIR) = \ln(C) - \frac{\Delta E}{KT} = \ln(C) - \frac{A}{T} \tag{5.2}$$

where C and A are empirical constants that need to be found experimentally.

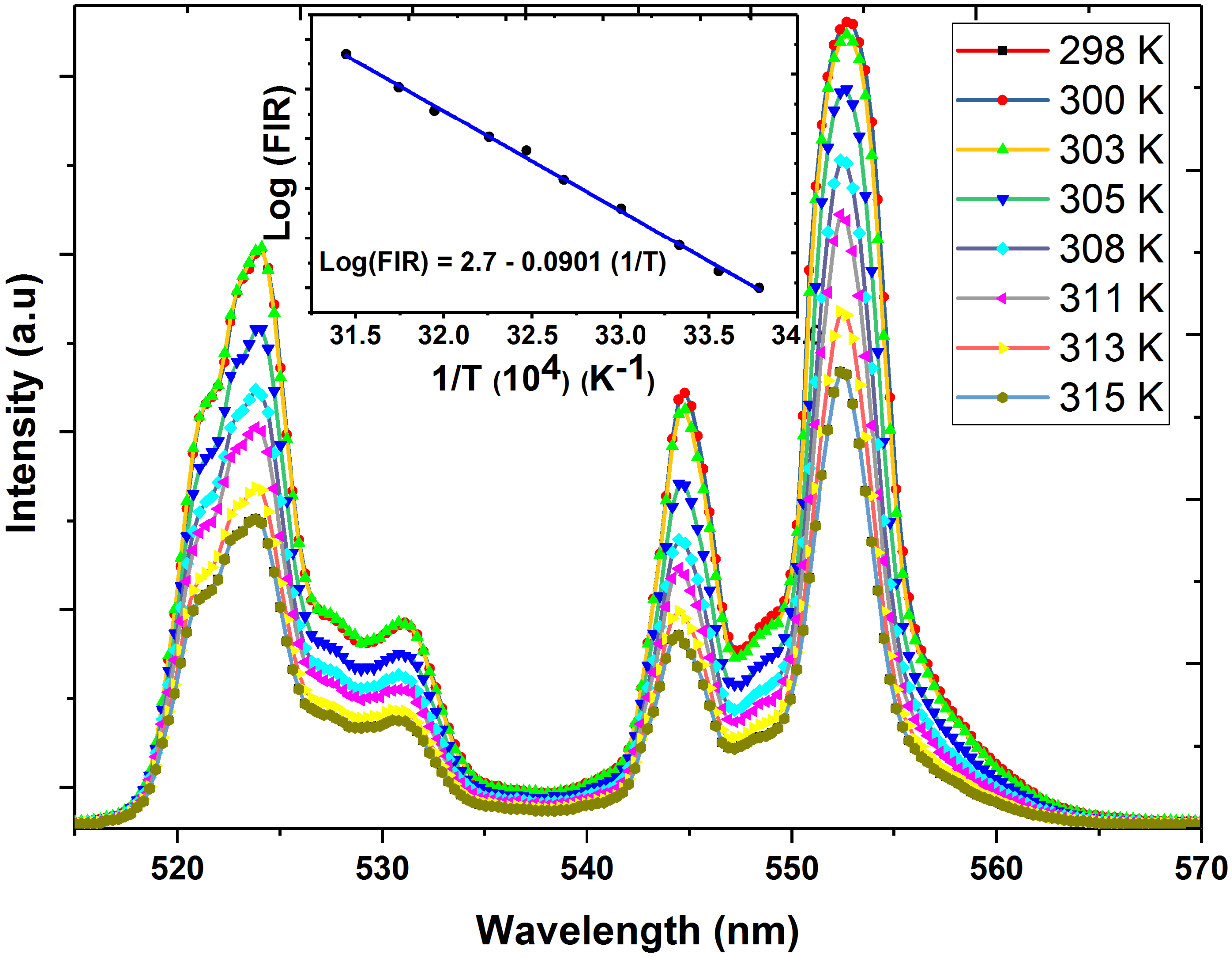

Figure 5.4: Upconversion luminescence emission spectrum of $YVO_4 : Er^{+3}, Yb^{+3}@Nd^{+3}$ core/shell NPs under 808 nm wavelength recorded over a small temperature range (298 K-315 K) . Inset: Linear fitting of the fluorescence intensity ratio (FIR) of the core/shell NPs dependence as a function of temperature.

Fitting the experimental data shown in Figure 5.4(inset) to equation (5.2) shows linear dependence between the FIR and temperature which reveals correlation between theory and experiment. Furthermore, results show good agreement with previous studies on optical temperature sensing using Er^{+3} UC luminescence [156]. It is very important to estimate the UCNPs sensitivity using the empirical parameters Ln(C) = 2.7 and A= 900 cm^{-1}. The relative sensor sensitivity (in $\%K^{-1}$) can be calculated using equation (5.3):

$$S_r = 100\% \left| \frac{1}{FIR} \frac{\partial FIR}{\partial T} \right| = 100\% (\frac{-\Delta E}{KT^2}) \tag{5.3}$$

The maximum relative sensitivity of the core/shell NPs was 1.01$\%$ K^{-1} at 308 K, which is in a good agreement with high relative sensitivity of UCNPs reported in [217].

Laser heating minimization in water was investigated in this experiment. 5ml of (5 mg/mL) of the $YVO_4 : Er^{+3}, Yb^{+3}@Nd^{+3}$ core/shell NPs dispersed in deionized water was placed in a small glass well (1cmX1cm) and examined on a confocal laser scanning microscope. Under continuous irradiation of two laser diodes (CW) (808 nm and 980 nm) with laser intensity 700 $mW.cm^{-2}$ for 20 min, laser irradiation dependent temperature rise was recorded. A temperature rise 6 ^oC was observed under 980 nm laser illumination for 20 min in contrast to 1.5 ^oC observed under 808 nm laser irradiation for the same period of time as shown in Figure 5.5. The extension of excitation bands of the core/shell UCNPs to shorter wavelengths minimized the laser-induced heating effect by diminishing the absorption by water.

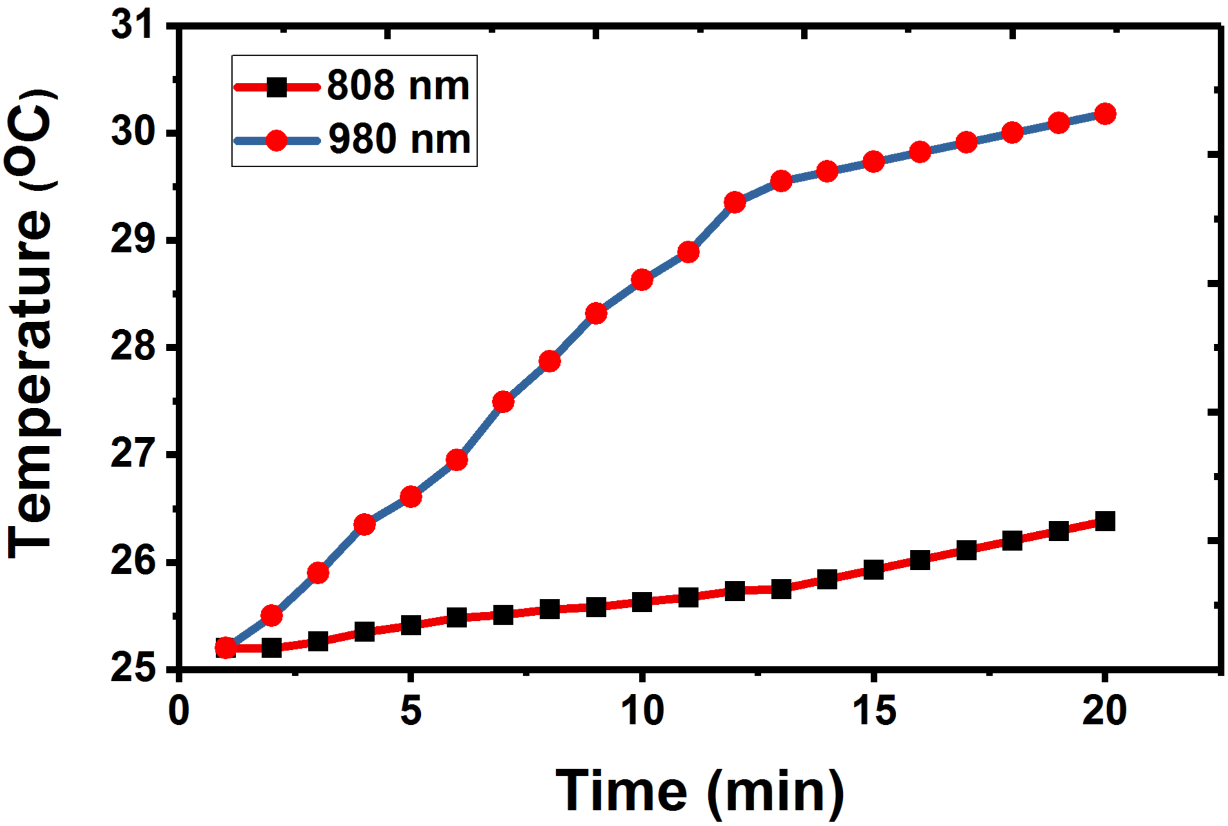

Figure 5.5: Comparison of temperature rise of (1 mg/mL) $YVO_4 : Er^{+3}, Yb^{+3}@Nd^{+3}$ core/shell NPs dispersed in 5 mL of distilled water under 808 nm and 980 nm laser irradiation at 700 $mW.cm^{-2}$ for 20 min.

5.4 Conclusion

In conclusion, we have developed water-based, biocompatible, high efficiency upconversion fluorescent markers $YVO_4 : Er^{+3}, Yb^{+3}@Nd^{+3}$ core/shell UCNPs. Implementing Nd^{+3} into the core/shell UCNPs combination has extended the NIR excitation band to a biocompatible excitation wavelength (808 nm) and also significantly minimized the overheating issues associated with typical 980 nm illumination wavelength. Optical temperature sensing with high thermal sensitivity $1.01\%K^{-1}$ was achieved using these UCNPs. Furthermore, laser heating minimization in water with the conventional UCNPs excitation (980 nm) wavelength and the new biocompatible illumination (808 nm) wavelength was evaluated. This report, although quite preliminary in many aspects, shows that $YVO_4 : Er^{+3}, Yb^{+3}@Nd^{+3}$ core/shell UCNPs have a great potential for biological applications.

6. APPLICATION OF FNDS AND UCNPS: NANOMETER SCALE LUMINESCENT THERMOMETRY IN BOVINE EMBRYOS*

6.1 Introduction

Temperature plays an important role in regulating the rate of metabolism in animals in general, and more specifically, in heterothermic animals such as insects, reptiles ,and fish [218–220]. Even in homothermic animals whose body temperature is maintained within narrow limits, changes in temperatures at the subcellular level may occur as a function of local metabolic activity. Such local changes in temperature may impact cellular functions such as enzymatic activities. To provide for high precision in thermal measurement with equivalent spatial resolution, many molecules and nanomaterials have been used as nanothermometers [14, 82]. Among these, fluorescent nanodiamonds (FNDs) are preferred due to their extraordinary photostability and biocompatibility, and upconversion nanoparticles (UCNPs) are preferred for photostability and their immunity to background bio-fluorescence [14, 27, 39, 82, 167].

So far, FNDs with the negatively charged nitrogen-vacancy (NV) centers have been used to measure the local temperature of living human cells with a precision of 200 mK/$\sqrt{Hz}$. and a spatial resolution of 200 nm [14]. The NV center measures temperature using a magnetic spin transition whose resonance frequency is sensitive to thermally-induced lattice expansion [54, 55]. It is also possible to use optical transitions for this purpose, for example the narrowband zero-phonon line of the silicon-vacancy (SiV) [221]. However, in high quality crystals, the NV spin transition can have a very long coherence time that translates to more sensitive thermometry, for example the NV in high quality bulk diamond has shown 1.8 mK temperature precision [14].

Upconversion nanoparticles (UCNPs) doped with lanthanide ions Ln^{+3} (Ln=Er,Tm,Ho,etc.) have demonstrated optical temperature sensing in living cells with high temperature resolution of about $0.5K$ [15, 153–156]. Here, temperature sensing is based on the relative thermal populations

---

*Reprinted with permission from Nanometer-scale luminescent thermometry in bovine embryos by Masfer Alkahtani, Linkun Jiang, Robert Brick, Philip Hemmer, Marlan Scully, 2017. Optics Letters, vol. 42, pp. 4812-4815, Copyright [2017] by the Optical Society of America (OSA) of two exited states which translates to a change in the fluorescence intensity ratio (FIR) of two transitions [156, 222]. The FIR method is an improvement over the alternative method of measuring the temperature dependent fluorescence on a single transition because it is independent of signal losses, excitation intensity fluctuations, etc. that might affect accurate temperature measurements [154]. Although the sensitivity of UCNPs is lower than FNDs, it is important to have two or more temperature sensors with different physics to address the recent controversy over large inaccuracies in local temperature measurements inside living cells reported in [94]. Additionally, the background-free fluorescence of UCNPs is important for relatively large specimens [27, 28].

Our study focused on newly fertilized bovine embryos prior to the first cell division as examples of large (1mm average diameter) cells of commercial value. In this work, we show proof-of-principle by injecting fixed bovine embryos with both FNDs and UCNPs and measured changes in local temperature inside the embryo induced by laser heating.

6.2 Experimental methods

Fluorescent nanodiamonds with average size (100 nm) were cleaned in nitric and sulfuric acids at ratio (1:1) and annealed at 550 ^oC for 10 mins in air to maximize the density of negativity charged carboxylic groups (at typical cellular pH) on their surface to avoid agglomeration in solution. For the UCNPs, we synthesized water-tolerant core-shell YVO4:Yb,Er@Nd upconversion nanoparticles with average size (25nm) for optical temperature sensing which is discussed in details in our previous work [167]. In short, we designed the core/shell nanoparticles by preparing the core nanoparticles $YVO_4 : Yb^{+3}, Er^{+3}$ (20%, 2%), and then Nd^{+3} was introduced by overgrowing a shell layer (3-4 nm) of $YVO_4 : Yb^{+3}, Nd^{+3}$ at (Yb^{+3} 10%, Nd^{+3}10%) doping ratio on the core NPs following a hydrothermal synthesis routes reported in [19, 20]. The main advantage of core/shell UCNPs design is to extend the NIR excitation band to a biocompatible excitation wavelength (808 nm) which significantly minimized the overheating issues associated with typical 980 nm illumination wavelength for UCNPs [29, 153, 164, 167].

High magnification transmission electron microscope (TEM) images were performed for FNDs and UCNPs as shown in Figure 6.1(a and c). The high magnification images reveal well crystallized UCNPs which are expected to exhibit high optical luminescence, and well dispersed FNDs and UCNPs. The average size of both nanoprobes were further confirmed using dynamic light scattering as shown in Figure 6.1(b and d).

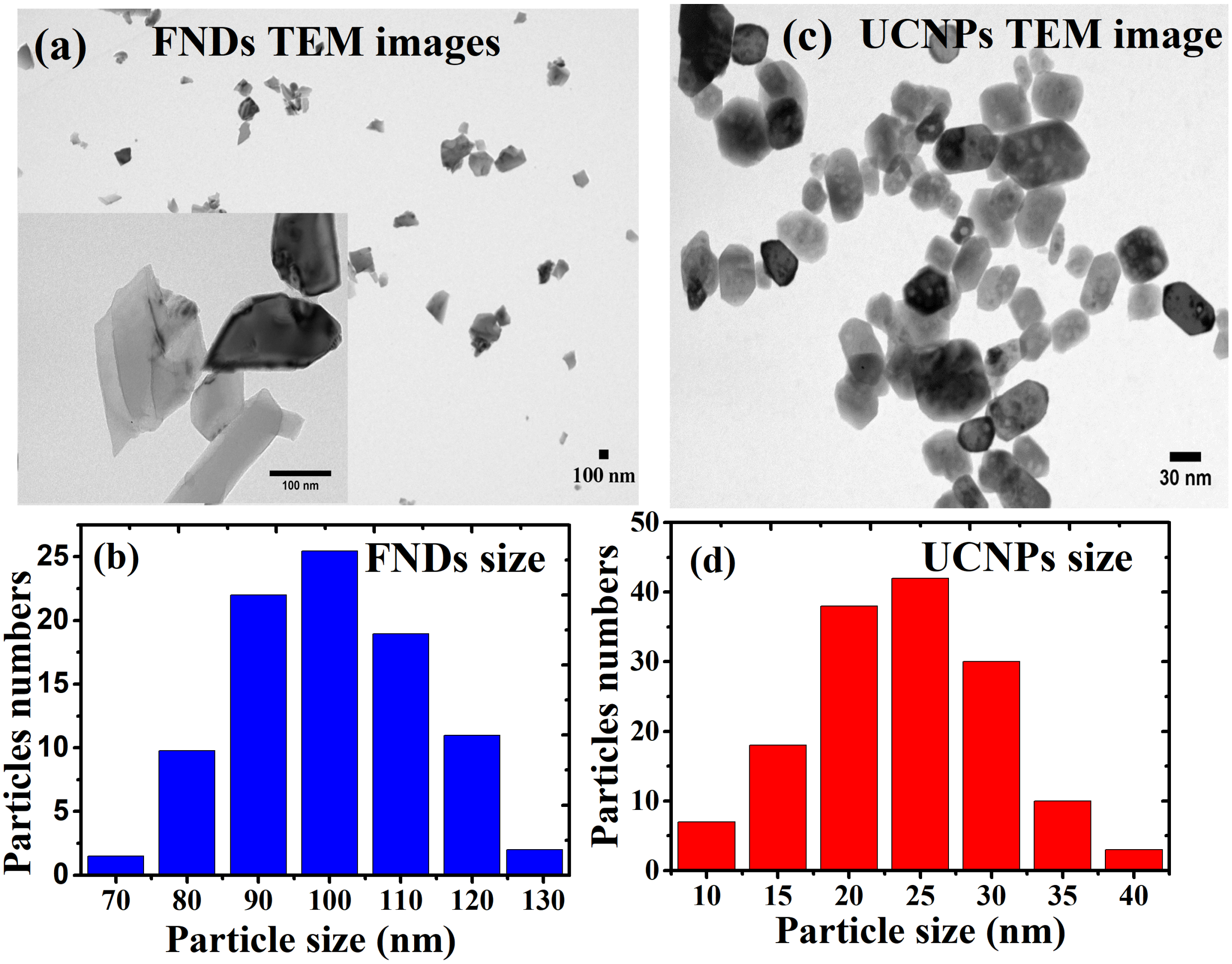

Figure 6.1: (a and c) High magnification TEM image of the fluorescent nanodiamonds (FNDs) and UCNPs dispersed in water and dropped onto a microgrid. The TEM images show well dispersed and nonagglomerated FNDs with average size (100nm) and well crystalline UCNPs with average size (25nm). (b and d) Average size distributions of the FNDs and UCNPs recorded by DLS.

Optical characterizations of FNDs and UCNPs, both inside and outside embryos, were performed using a home-built confocal scanning microscope equipped with variety of laser wavelengths ranging from visible (VIS) to near infrared (NIR). The excitation lasers are focused through a long working distance VIS/NIR corrected microscope objective with NA = 0.8 (Olympus) with magnification 100x. The fluorescence was collected, filtered from reflected laser light by optical notch filters for each illumination wavelength, and analyzed by a photon counter and homebuilt spectrometer. Also a microwave excitation system was installed on the confocal microscope to perform optically detected magnetic resonance (ODMR) spectroscopy of the NV center in FNDs.

6.3 Results and discussion

For initial optical characterization, a thin layer of nanocrystals of each sample was spin-coated over a quartz coverslip and mounted on a microwave electronics board. The samples were examined under excitation by two laser diodes, 532nm for FNDs at laser intensity of 900 W/cm^2, and 808 nm for UCNPs at intensity of 750 W/cm^2. Under green (532nm) illumination, FNDs showed a clear nitrogen-vacancy photoluminescence with neutral nitrogen-vacancy (NV^0) and negatively charged nitrogen-vacancy (NV^-) zero-phonon lines peaked at 575nm, and 638nm respectively as shown in Figure 6.2(a). ODMR spectroscopy of the NVs was then performed as shown in Figure 6.2(b). Briefly ODMR is possible in the NV because optical pumping polarizes the NV center into the $m_s = 0$ spin sublevel (80% populated). Additionally, when a resonant microwave field induces a magnetic transition between the $m_s = 0$ spin sublevel and the $m_s = \pm 1$ levels, a significant decrease of NV fluorescence results which is called optically-detected magnetic spin resonance (ODMR) [39, 50]. At zero magnetic field the S = 1 spin ground state which is split into two spin sublevels,(two fold degenerate) and with zero-field splitting D = 2.87 GHz (temperature dependent D(T)) due to spin-orbit interactions and the diamond crystal field as shown in Figure 6.3(a) [53].

The UCNP sample was examined under 808 nm laser excitation, and exhibited two strong green emission bands (520 nm, and 550 nm), and a weak red emission at 650 nm corresponding to these transitions$^2H_{11/2}\longrightarrow {}^4I_{15/2}$, ${}^4S_{3/2}\longrightarrow {}^4I_{15/2}$, and ${}^4F_{9/2} \longrightarrow {}^4I_{15/2}$ of the Er^{+3} ion as shown in Figure 6.2(c). To verify the two-photon nature of the upconversion process, power-dependent emission intensities measurements of the UCNPs sample under 808 nm laser excitations were performed. Figure 6.2(d) shows a slope equal to 1.91 which indicates a two-photon process in UCNPs.

The temperature-dependent fluorescence intensity ratio (FIR) in erbium Er^{+3} as illustrated in Figure 6.3(b) is derived in detail in [222].

$$FIR = \frac{I_{525}}{I_{550}} = C\exp(\frac{-\Delta E}{KT}) \tag{6.1}$$

where, I_{525} is the upconversion luminescence (UCL) of $(^2H_{11/2}\longrightarrow {}^4I_{15/2})$ transition of the Er^{+3} doped UCNPs centered at 525 nm and I_{550} is the UCL $^4S_{3/2}\longrightarrow {}^4I_{15/2}$ transitions of the Er^{+3} doped UCNPs centered at 550 nm, respectively; C is a constant can be determined by the degeneracy, spontaneous emission rate and photon energies of the emitting states in the host materials; T is the temperature, and k is the Boltzmann's constant; ΔE is the energy gap of two thermally coupled energy levels.

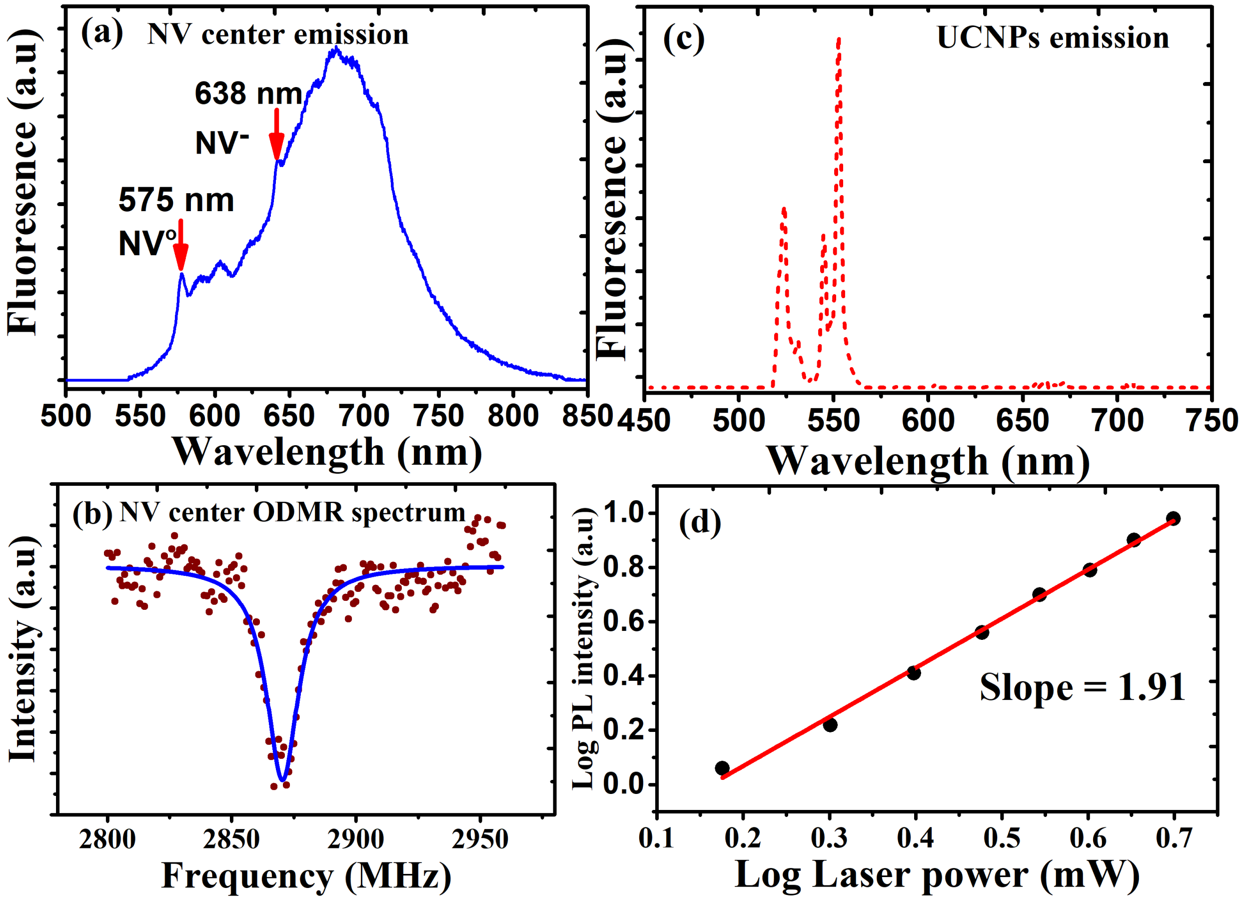

Figure 6.2: (a and c) Photoluminescence emission spectra of FNDs and UCNPs. Theses spectra reveal the NV^o and NV^- peaks at (575 nm and 638 nm) in the NV center emission curve and the two strong green emissions of erbium-doped upconversion nanoparticles.(b) ODMR spectrum of the NV center . (d) logarithmic scale of the UCNPs green luminescence dependence as a function of 808 nm excitation power.

Equation (6.1) can be rewritten as follows:

$$\ln(FIR) = \ln(C) - \frac{\Delta E}{KT} = \ln(C) - \frac{A}{T} \tag{6.2}$$

where C and A are empirical constants that need to be found experimentally.

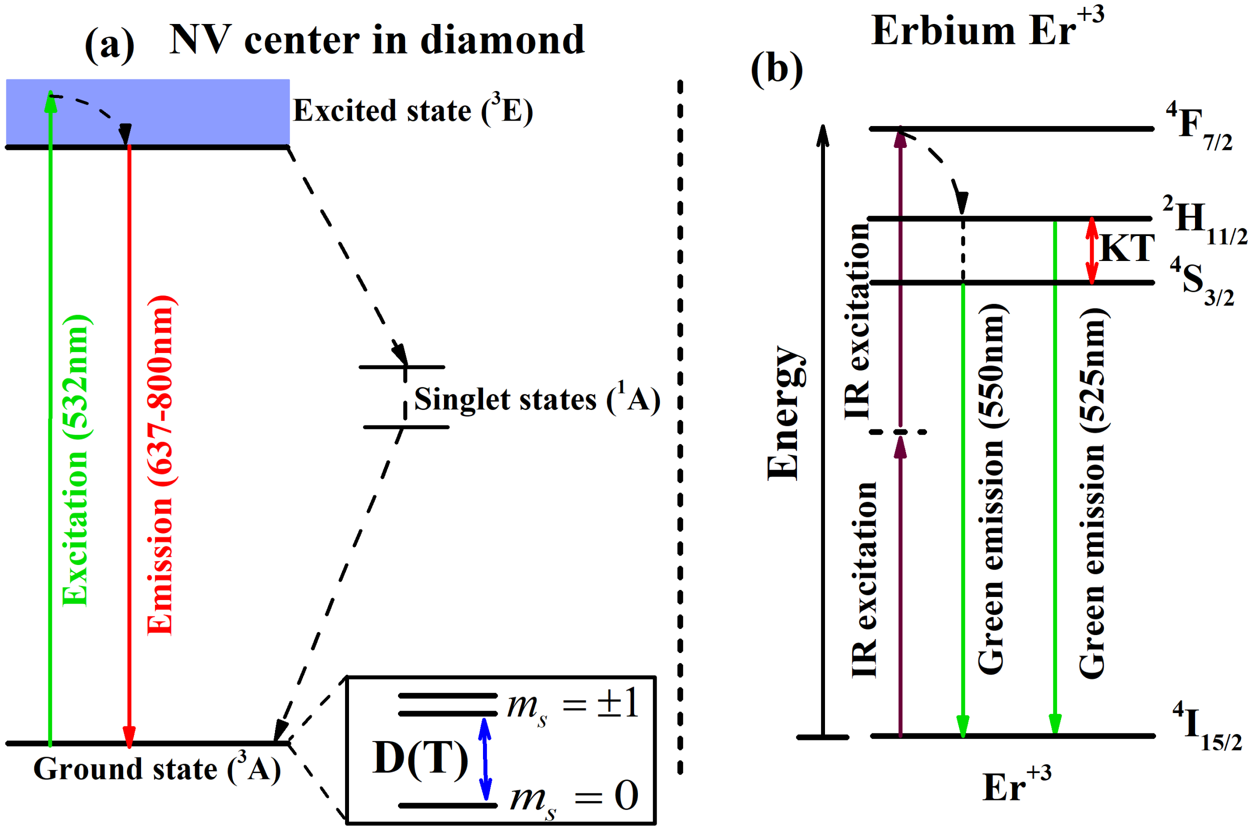

Figure 6.3: (a) Electronic structure and fluorescence emission bands for the NV . The ground state consist of three sublevels where is separated with temperature dependent zero field splitting D(T). (b) The energy level diagram and fluorescence emission bands for erbium Er^{+3}. The thermally coupled levels in the excited state are responsible for temperature sensing in erbium ion.

Prior to embryo injection, bovine embryos were fixed in 3.7% formaldehyde. 10 μL of FNDs and UCNPs were injected into individual fixed bovine embryos using a picoliter injector. Embryos were attached to a micromanipulator to hold the embryo during injection as shown in Figure 6.4(a). Bright field images of several embryos after injection are shown in Figure 6.4(b). An injected embryo was then placed into a portable incubator attached to a precise heating stage ($\pm 0.1\ ^oC$) and microwave wires to perform optical and ODMR spectroscopy for temperature sensing using FNDs. The injected embryo were scanned with 532 nm at power intensity of 900 W/cm^2 and 808 nm lasers and 808 nm for UCNPs at intensity of 750 W/cm^2 after placing the incubator on the confocal microscope. Figure 6.4(c) shows two-dimensional superimposed image of embryo scanned with green (532nm) and NIR (808nm) lasers. To demonstrate that the red and green spots are the FNDs and UCNPs, the optical spectra of NV FNDs (red spots) and Er^{+3} UCNPs (green spots) respectively are shown in Figure 6.4(d and e).

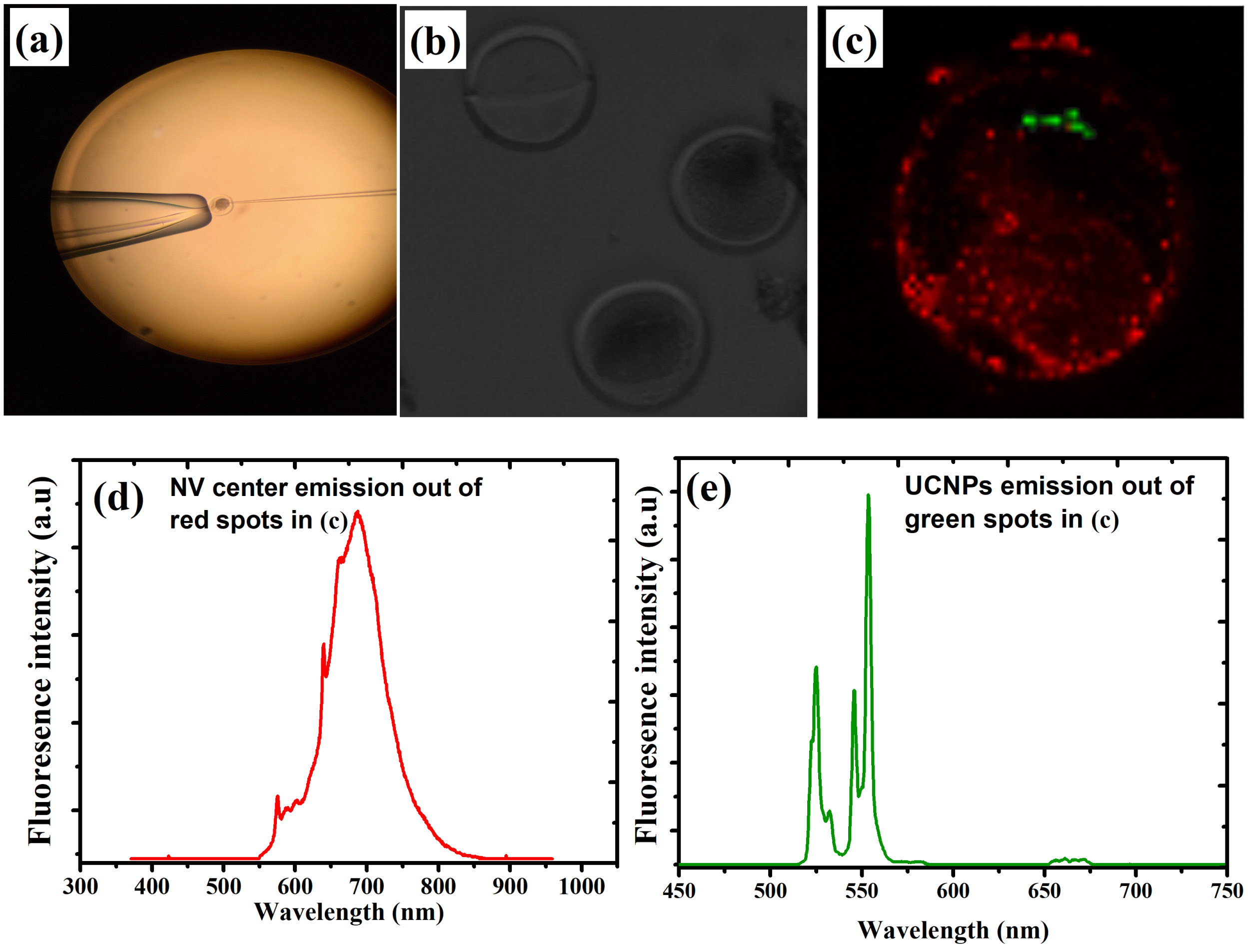

Figure 6.4: (a) An illustration of bovine embryo cell injection with FNDs and UCNPs. (b) Bright field image of some bovine embryo cells after injection (c) Superimposed image of bovine embryo cell injected with FNDs and UCNPs. The red spots represent FNDs plus some auofluoresence background induced by the green laser excitation. (d) The NV center luminescence emission curve recorded by spectrometer out of most of the red spots in (c). (e) UCNPs fluorescence emission recorded from all the green spots shown in (c).

Temperature-sensing inside embryos was done, first, using NV centers in FNDs under green (532nm) laser excitation, to perform optically detected electron spin resonance (ODMR).The NV center in FNDs is calibrated for temperature over the biological temperature range (25^oC to 40^oC) using a precise heating stage. It is well known that a 980 nm laser wavelength overlaps with water molecule absorption, resulting in biological tissues heating [167]. So we used 980 nm laser (with power varing from 1 to 10 mW) as a heating source inside the embryo in this study. Figure 6.5(a) shows ODMR spectral shifts as a function of temperature changes of over a 24^oC to 40^oC range. As the temperature of nanodiamonds increases in the embryo, the spectrum of the ODMR is shifted toward lower microwave frequencies. After fitting the experimental data, Figure 6.5(b) illustrates the linear dependence between the frequency shift of the ODMR spectra and temperature with a slope $\frac{dM}{dT}$= -72.3 $\frac{kHZ}{C}$ of a linear equation which provides a good calibration for temperature measurements using FNDs. The sensitivity of the NV color center nano-thermometer based on this data is 270 mK/$\sqrt{Hz}$.

Second, the embryo$'$s temperature was sensed using the core/shell UCNPs under NIR (808nm) laser excitation which is calibrated for temperature measurement using a precise heating stage over the biological range (25^oC to 40^oC). Here, temperature changes by laser heating (980nm) were detected using the fluorescence intensity ratio (FIR) of the transitions from the ($^2H_{11/2}$ and $^4S_{3/2}$) Erbium excited states to the $^4I_{15/2}$ ground state which is controlled by Boltzmann populations as shown in Figure 6.5(c). Fitting the experimental data shown in Figure 6.5(d) to equation (6.2) shows linear dependence between the FIR and temperature which reveals good temperature calibration for sensing temperature using UCNPs.The sensitivity of the UCNPs nano-thermometer based on this data is 320 mK/$\sqrt{Hz}$.

To demonstrate a direct correlation of temperature measurements with two modalities, we performed temperature measurements by injecting another embryo with a mixture of FNDs and UCNPs such that they were homogeneously dispersed inside the embryo. These were then excited simultaneously with three lasers, 532nm green laser for FNDs, 808nm NIR laser for UCNPs, and 980nm for laser heating and optical and ODMR spectra were acquired simultaneously. Analyzing these data gave very close temperature readings for both modalities at different laser heating powers. For instance, at 1.5mW of laser heating power, we found the temperature inside the embryo is

25.4^oC using NV centers in FNDs while the temperature is 25.6^oC using UCNPs. After increasing the power of laser heating to 2.5 mW, we recorded a higher temperature of 27.5^oC measured by FNDs and 27.8^oC measured by UCNPs. The small difference in temperature measurements is within the sensitivity limit of the two modalities.

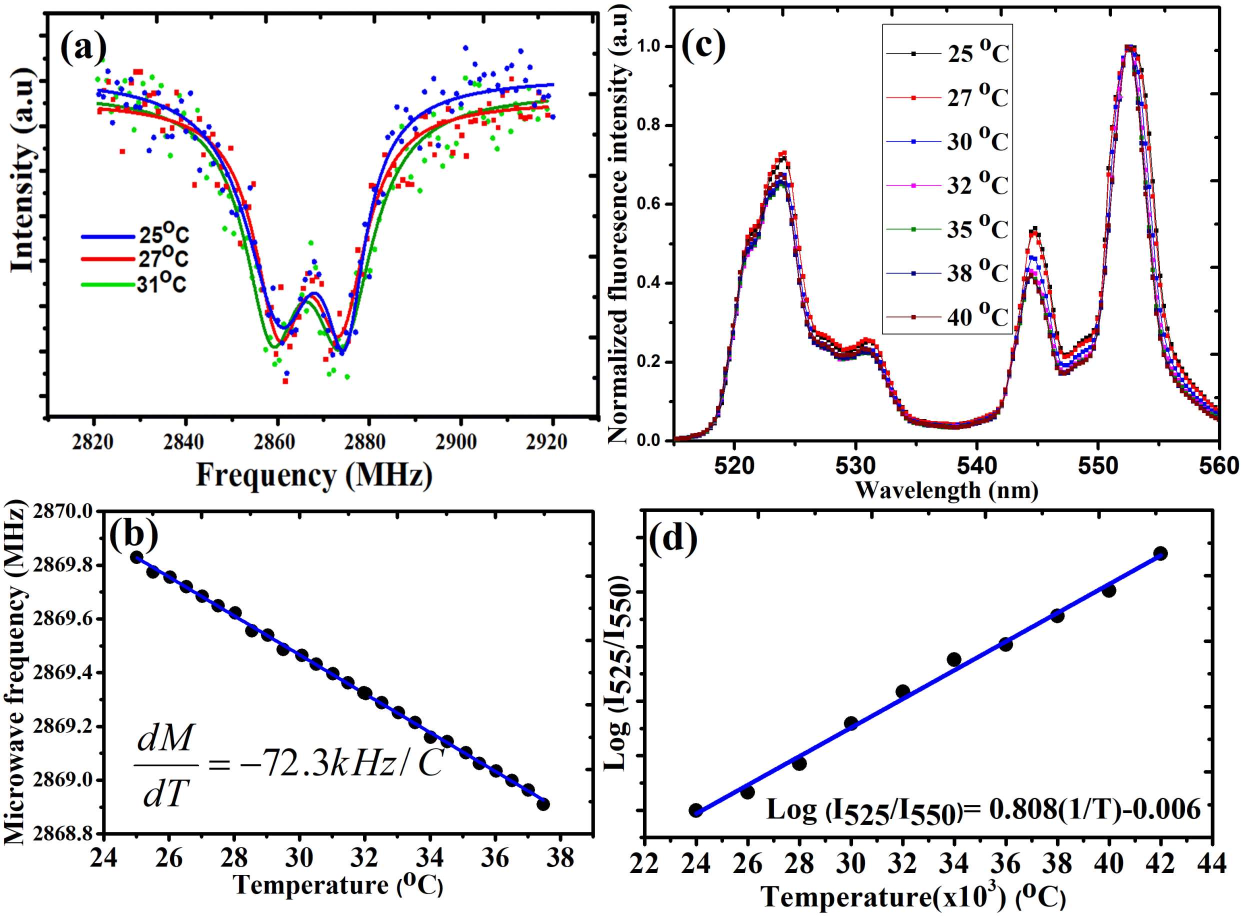

Figure 6.5: (a) ODMR spectra of NV color center in nanodiamonds inside emberyos under 532 nm illumination recorded at different temperatures induced by 980 nm laser; (25^oC black), (33^oC red), (37^oC green), and (41^oC blue). (b) Linear fitting of the central frequency of the ODMR spectrum of NV centers in FNDs as a function of temperatures. (c) The upconversion emission spectra inside the embryos under 808nm laser recorded over a small range of temperature (25^oC-40^oC) induced by 980 nm laser. (d) Linear fitting of the fluorescence intensity ratio (FIR) of the UCNPs dependence as a function of temperature.

6.4 Conclusion

In conclusion, in this work, we have succeeded in measuring temperature changes at the subcellular level simultaneously using fluorescent nanodiamonds and upconversion nanoparticles in bovine embryos. The use of two modalities make theses results far less sensitive to confusers for nanothermometers in complex systems like living cells [94]. It is anticipated that these results will lead to further investigations of temperature changes in live cells during fertilization and embryonic development. Furthermore, we will investigate the use of other color centers in FNDs and other ions doped onto UCNPs that will permit further examination of biological activity within the tissue transparency window.

7. SUMMARY AND CONCLUSIONS

In this dissertation, we discussed the most interesting fluorescent markers for biological applications. Here, we investigated fluorescent nanodiamonds (FNDs) and upconversion nanoparticles (UCNPs) from growth/synthesis to application in high contrast bio-imaging and optical temperature sensing in living organisim. This work was conducted over several chapters which can be summarized as follows:

In chapter 1, first, we discussed that FNDs are promising fluorescent markers for most of biomedical applications. Compared to colloidal quantum dots and organic dyes, they have the advantage of better photostability, lower toxicity. They exhibit a variety of emission wavelengths from visible to near infrared, with narrow or broad bandwidths depending on the color centers in FNDs. The optical properties and new color centers in FNDs were discussed in detail in this chapter. Also, we reviewed in detail their biocompatibility and exceptional applications in bio-imaging and biosensing, especially, in temperature sensing, super-resolution, and MRI imaging. Second, we discussed that upconversion nanoparticles (UCNPs) are of interest because they allow suppression of tissue autofluorescence and are therefore visible deep inside biological tissue. Compared to upconversion dyes, UCNPs have a lower pump intensity threshold, better photostability, and less toxicity. We reviewed their early developments, upconversion mechanisms, and their applications in bio-imaging and biosensing.

In chapter 2, we conducted controlled diamond growth around diamond-like seed molecules at much lower temperatures than typical HPHT nanodiamond growth. We performed different experiments to confirm success of the seeded growth approach. In particular, we observed two different color centers in nanodiamonds grown from two different diamond-like organic seed molecules. Furthermore, we observed no nanodiamonds in the absence of diamond-like seed in a control experiment. These results strongly support our claim that our nanodiamond seeded growth approach is successfully working. This success will open the door for many interesting applications using ultrasmall nanodiamonds with stable fluorescence.

In chapter 3, we reported temperature sensing with NV and Ni diamond color centers excited in the biological transparency window in FNDs crystals. For NV we show good ODMR signal at laser intensity well below the biological tissues damage threshold. Importantly, optical temperature sensing using NV and Ni color centers can be performed simultaneously using different physical mechanisms. This is a promising approach to avoid sensor confusion and provide accurate temperature measurements within living biological systems. In chapter 4, we synthesized high quality $YVO_4 : Er^{+3}, Yb^{+3}$ upconversion nanoparticles for bio-imaging in living organism. We imaged these UCNPs inside red imported fire ants (Solenopsis invicta) which have small and special body geometry that behaves as a spherical lens. Imaging a small and spherical body like an ant is a very difficult and challenging task using a confocal microscope. To overcome this problem, we designed a homemade wide field side illumination microscopy setup. We detected a strong up-conversion luminescence (UCL) with high signal-to-noise ratio, and photostable UCL for a long exposure time without damaging the ants's bodies under NIR laser excitation. This work has shown that UCNPs can used as a high contrast imaging agents in living organisms. In chapter 5, we have developed water-based, biocompatible, high efficiency upconversion fluorescent markers $YVO_4 : Er^{+3}, Yb^{+3}@Nd^{+3}$ core/shell UCNPs. Implementing Nd^{+3} into the core/shell UCNPs combination has extended the NIR excitation band to a biocompatible excitation wavelength (808 nm) and also significantly minimized the overheating issues associated with typical 980 nm illumination wavelength. Optical temperature sensing with high thermal sensitivity $1.01\%K^{-1}$ was achieved using these UCNPs. Furthermore, laser heating minimization in water with the conventional UCNPs excitation (980 nm) wavelength and the new biocompatible illumination (808 nm) wavelength was evaluated. This work shows that $YVO_4 : Er^{+3}, Yb^{+3}@Nd^{+3}$ core/shell UCNPs have a great potential for optical temperature sensing in biological applications.

In chapter 6, we have succeeded in measuring temperature changes at the subcellular level simultaneously using FNDs and UCNPs in bovine embryos. The use of two modalities make these results far less sensitive to confusers for nanothermometers in complex systems like living cells [94]. It is anticipated that these results will lead to further investigations of temperature changes in live cells during fertilization and embryonic development. Furthermore, we will investigate the use of other color centers in FNDs and other ions doped onto UCNPs that will permit further examination of biological activity within the tissue transparency window.

REFERENCES

[1] X. Ge, Z. M. Song, L. Sun, Y. F. Yang, L. Shi, R. Si, W. Ren, X. Qiu, and H. Wang, "Lanthanide (gd(3+) and yb(3+)) functionalized gold nanoparticles for in vivo imaging and therapy," *Biomaterials*, vol. 108, pp. 35–43, 2016.

[2] Y. Koide, Y. Urano, K. Hanaoka, W. Piao, M. Kusakabe, N. Saito, T. Terai, T. Okabe, and T. Nagano, "Development of nir fluorescent dyes based on si-rhodamine for in vivo imaging," *J Am Chem Soc*, vol. 134, no. 11, pp. 5029–31, 2012.

[3] X. Michalet, F. F. Pinaud, L. A. Bentolila, J. M. Tsay, S. Doose, J. J. Li, G. Sundaresan, A. M. Wu, S. S. Gambhir, and S. Weiss, "Quantum dots for live cells, in vivo imaging, and diagnostics," *Science*, vol. 307, no. 5709, pp. 538–44, 2005.

[4] M. A. Walling, J. A. Novak, and J. R. Shepard, "Quantum dots for live cell and in vivo imaging," *Int J Mol Sci*, vol. 10, no. 2, pp. 441–91, 2009.

[5] J. Yu, X. Zhang, X. Hao, X. Zhang, M. Zhou, C. S. Lee, and X. Chen, "Near-infrared fluorescence imaging using organic dye nanoparticles," *Biomaterials*, vol. 35, no. 10, pp. 3356–64, 2014.

[6] Q. Zhang, N. Iwakuma, P. Sharma, B. M. Moudgil, C. Wu, J. McNeill, H. Jiang, and S. R. Grobmyer, "Gold nanoparticles as a contrast agent for in vivo tumor imaging with photoacoustic tomography," *Nanotechnology*, vol. 20, no. 39, p. 395102, 2009.

[7] J. M. Yang, H. Yang, and L. Lin, "Quantum dot nano thermometers reveal heterogeneous local thermogenesis in living cells," *ACS Nano*, vol. 5, no. 6, pp. 5067–71, 2011.

[8] L. M. Maestro, E. M. Rodriguez, F. S. Rodriguez, M. C. la Cruz, A. Juarranz, R. Naccache, F. Vetrone, D. Jaque, J. A. Capobianco, and J. G. Sole, "Cdse quantum dots for two-photon fluorescence thermal imaging," *Nano Lett*, vol. 10, no. 12, pp. 5109–15, 2010.

[9] J. S. Donner, S. A. Thompson, M. P. Kreuzer, G. Baffou, and R. Quidant, “Mapping intracellular temperature using green fluorescent protein,” *Nano Lett*, vol. 12, no. 4, pp. 2107–11, 2012.

[10] S. Kiyonaka, T. Kajimoto, R. Sakaguchi, D. Shinmi, M. Omatsu-Kanbe, H. Matsuura, H. Imamura, T. Yoshizaki, I. Hamachi, T. Morii, and Y. Mori, “Genetically encoded fluorescent thermosensors visualize subcellular thermoregulation in living cells,” *Nat Methods*, vol. 10, no. 12, pp. 1232–8, 2013.

[11] K. Okabe, N. Inada, C. Gota, Y. Harada, T. Funatsu, and S. Uchiyama, “Intracellular temperature mapping with a fluorescent polymeric thermometer and fluorescence lifetime imaging microscopy,” *Nat Commun*, vol. 3, p. 705, 2012.

[12] X. Zheng, X. Zhu, Y. Lu, J. Zhao, W. Feng, G. Jia, F. Wang, F. Li, and D. Jin, “High-contrast visualization of upconversion luminescence in mice using time-gating approach,” *Anal Chem*, vol. 88, no. 7, pp. 3449–54, 2016.

[13] O. Zohar, M. Ikeda, H. Shinagawa, H. Inoue, H. Nakamura, D. Elbaum, D. L. Alkon, and T. Yoshioka, “Thermal imaging of receptor-activated heat production in single cells,” *Biophys J*, vol. 74, no. 1, pp. 82–9, 1998.

[14] G. Kucsko, P. C. Maurer, N. Y. Yao, M. Kubo, H. J. Noh, P. K. Lo, H. Park, and M. D. Lukin, “Nanometre-scale thermometry in a living cell,” *Nature*, vol. 500, no. 7460, pp. 54–8, 2013.

[15] F. Vetrone, R. Naccache, A. Zamarron, A. Juarranz de la Fuente, F. Sanz-Rodriguez, L. Martinez Maestro, E. Martin Rodriguez, D. Jaque, J. Garcia Sole, and J. A. Capobianco, “Temperature sensing using fluorescent nanothermometers,” *ACS Nano*, vol. 4, no. 6, pp. 3254–8, 2010.

[16] U. Resch-Genger, M. Grabolle, S. Cavaliere-Jaricot, R. Nitschke, and T. Nann, “Quantum dots versus organic dyes as fluorescent labels,” *Nat Methods*, vol. 5, no. 9, pp. 763–75, 2008.

[17] L. Gao, L. Shao, B. C. Chen, and E. Betzig, “3d live fluorescence imaging of cellular dynamics using bessel beam plane illumination microscopy,” *Nat Protoc*, vol. 9, no. 5, pp. 1083–101, 2014.

[18] L. Gu, D. J. Hall, Z. Qin, E. Anglin, J. Joo, D. J. Mooney, S. B. Howell, and M. J. Sailor, “In vivo time-gated fluorescence imaging with biodegradable luminescent porous silicon nanoparticles,” *Nat Commun*, vol. 4, p. 2326, 2013.

[19] M. F. Juette, D. S. Terry, M. R. Wasserman, Z. Zhou, R. B. Altman, Q. Zheng, and S. C. Blanchard, “The bright future of single-molecule fluorescence imaging,” *Curr Opin Chem Biol*, vol. 20, pp. 103–11, 2014.

[20] P. J. Keller, “Imaging morphogenesis: technological advances and biological insights,” *Science*, vol. 340, no. 6137, p. 1234168, 2013.

[21] A. Kusumi, T. A. Tsunoyama, K. M. Hirosawa, R. S. Kasai, and T. K. Fujiwara, “Tracking single molecules at work in living cells,” *Nat Chem Biol*, vol. 10, no. 7, pp. 524–32, 2014.

[22] A. Waggoner, “Fluorescent labels for proteomics and genomics,” *Curr Opin Chem Biol*, vol. 10, no. 1, pp. 62–6, 2006.

[23] D. Bera, L. Qian, and P. H. Holloway, *Phosphor Quantum Dots*, pp. 19–73. John Wiley & Sons, Ltd, 2008.

[24] K. Rurack and M. Spieles, “Fluorescence quantum yields of a series of red and near-infrared dyes emitting at 600-1000 nm,” *Anal Chem*, vol. 83, no. 4, pp. 1232–42, 2011.

[25] J. A. Zelken and A. P. Tufaro, “Current trends and emerging future of indocyanine green usage in surgery and oncology: An update,” *Ann Surg Oncol*, vol. 22 Suppl 3, pp. S1271–83, 2015.

[26] A. P. Alivisatos, “Semiconductor clusters, nanocrystals, and quantum dots,” *Science*, vol. 271, no. 5251, pp. 933–937, 1996.

[27] M. Alkahtani, Y. Chen, J. J. Pedraza, J. M. Gonzalez, D. Y. Parkinson, P. R. Hemmer, and H. Liang, “High resolution fluorescence bio-imaging upconversion nanoparticles in insects,” *Opt Express*, vol. 25, no. 2, pp. 1030–1039, 2017.

[28] M. H. Alkahtani, F. S. Alghannam, C. Sanchez, C. L. Gomes, H. Liang, and P. R. Hemmer, “High efficiency upconversion nanophosphors for high-contrast bioimaging,” *Nanotechnology*, vol. 27, no. 48, p. 485501, 2016.

[29] Y. F. Wang, G. Y. Liu, L. D. Sun, J. W. Xiao, J. C. Zhou, and C. H. Yan, “Nd(3+)-sensitized upconversion nanophosphors: efficient in vivo bioimaging probes with minimized heating effect,” *ACS Nano*, vol. 7, no. 8, pp. 7200–6, 2013.

[30] O. S. Wolfbeis, “An overview of nanoparticles commonly used in fluorescent bioimaging,” *Chem Soc Rev*, vol. 44, no. 14, pp. 4743–68, 2015.

[31] G. Hong, S. Diao, A. L. Antaris, and H. Dai, “Carbon nanomaterials for biological imaging and nanomedicinal therapy,” *Chemical Reviews*, vol. 115, no. 19, pp. 10816–10906, 2015.

[32] M. Montalti, A. Cantelli, and G. Battistelli, “Nanodiamonds and silicon quantum dots: ultrastable and biocompatible luminescent nanoprobes for long-term bioimaging,” *Chem Soc Rev*, vol. 44, no. 14, pp. 4853–921, 2015.

[33] N. Lewinski, V. Colvin, and R. Drezek, “Cytotoxicity of nanoparticles,” *Small*, vol. 4, no. 1, pp. 26–49, 2008.

[34] Y. Cheng, G. Lu, Y. He, H. Shen, J. Zhao, K. Xia, and Q. Gong, “Luminescence quantum yields of gold nanoparticles varying with excitation wavelengths,” *Nanoscale*, vol. 8, no. 4, pp. 2188–94, 2016.

[35] W. Rao, Q. Li, Y. Wang, T. Li, and L. Wu, “Comparison of photoluminescence quantum yield of single gold nanobipyramids and gold nanorods,” *ACS Nano*, vol. 9, no. 3, pp. 2783–91, 2015.

[36] A. Zaitsev, “Optical properties of diamond : a data handbook,” *Berlin ; New York: Springer.*, vol. xvii, 502 p., no. xvii, 502 p., 2001.

[37] W. W. Hsiao, Y. Y. Hui, P. C. Tsai, and H. C. Chang, “Fluorescent nanodiamond: A versatile tool for long-term cell tracking, super-resolution imaging, and nanoscale temperature sensing,” *Acc Chem Res*, vol. 49, no. 3, pp. 400–7, 2016.

[38] P. Reineck, A. Francis, A. Orth, D. W. M. Lau, R. D. V. Nixon-Luke, I. D. Rastogi, W. A. W. Razali, N. M. Cordina, L. M. Parker, V. K. A. Sreenivasan, L. J. Brown, and B. C. Gibson, “Brightness and photostability of emerging red and near-ir fluorescent nanomaterials for bioimaging,” *Advanced Optical Materials*, vol. 4, no. 10, pp. 1549–1557, 2016.

[39] R. Schirhagl, K. Chang, M. Loretz, and C. L. Degen, “Nitrogen-vacancy centers in diamond: nanoscale sensors for physics and biology,” *Annu Rev Phys Chem*, vol. 65, pp. 83–105, 2014.

[40] Y. Wu, F. Jelezko, M. B. Plenio, and T. Weil, “Diamond quantum devices in biology,” *Angew Chem Int Ed Engl*, vol. 55, no. 23, pp. 6586–98, 2016.

[41] T. Iwasaki, Y. Miyamoto, T. Taniguchi, P. Siyushev, M. H. Metsch, F. Jelezko, and M. Hatano, “Tin-vacancy quantum emitters in diamond,” *Phys Rev Lett*, vol. 119, no. 25, p. 253601, 2017.

[42] I. Aharonovich and E. Neu, “Diamond nanophotonics,” *Advanced Optical Materials*, vol. 2, no. 10, pp. 911–928, 2014.

[43] A. M. Zaitsev, “Vibronic spectra of impurity-related optical centers in diamond,” *Physical Review B*, vol. 61, no. 19, pp. 12909–12922, 2000.

[44] M. W. Doherty, N. B. Manson, P. Delaney, F. Jelezko, J. Wrachtrup, and L. C. L. Hollenberg, “The nitrogen-vacancy colour centre in diamond,” *Physics Reports*, vol. 528, no. 1, pp. 1–45, 2013.

[45] S. Hong, M. S. Grinolds, L. M. Pham, D. Le Sage, L. Luan, R. L. Walsworth, and A. Yacoby, “Nanoscale magnetometry with nv centers in diamond,” *MRS Bulletin*, vol. 38, no. 2, pp. 155–161, 2013.

[46] F. Dolde, H. Fedder, M. W. Doherty, T. NÃűbauer, F. Rempp, G. Balasubramanian, T. Wolf, F. Reinhard, L. C. L. Hollenberg, F. Jelezko, and J. Wrachtrup, "Electric-field sensing using single diamond spins," *Nature Physics*, vol. 7, p. 459, 2011.

[47] D. M. Toyli, D. J. Christle, A. Alkauskas, B. B. Buckley, C. G. Van de Walle, and D. D. Awschalom, "Measurement and control of single nitrogen-vacancy center spins above 600 k," *Physical Review X*, vol. 2, no. 3, p. 031001, 2012.

[48] J. R. Maze, P. L. Stanwix, J. S. Hodges, S. Hong, J. M. Taylor, P. Cappellaro, L. Jiang, M. V. G. Dutt, E. Togan, A. S. Zibrov, A. Yacoby, R. L. Walsworth, and M. D. Lukin, "Nanoscale magnetic sensing with an individual electronic spin in diamond," *Nature*, vol. 455, p. 644, 2008.

[49] G. Balasubramanian, P. Neumann, D. Twitchen, M. Markham, R. Kolesov, N. Mizuochi, J. Isoya, J. Achard, J. Beck, J. Tissler, V. Jacques, P. R. Hemmer, F. Jelezko, and J. Wrachtrup, "Ultralong spin coherence time in isotopically engineered diamond," *Nat Mater*, vol. 8, no. 5, pp. 383–7, 2009.

[50] G. Balasubramanian, I. Y. Chan, R. Kolesov, M. Al-Hmoud, J. Tisler, C. Shin, C. Kim, A. Wojcik, P. R. Hemmer, A. Krueger, T. Hanke, A. Leitenstorfer, R. Bratschitsch, F. Jelezko, and J. Wrachtrup, "Nanoscale imaging magnetometry with diamond spins under ambient conditions," *Nature*, vol. 455, no. 7213, pp. 648–51, 2008.

[51] L. T. Hall, C. D. Hill, J. H. Cole, B. Stadler, F. Caruso, P. Mulvaney, J. Wrachtrup, and L. C. Hollenberg, "Monitoring ion-channel function in real time through quantum decoherence," *Proc Natl Acad Sci U S A*, vol. 107, no. 44, pp. 18777–82, 2010.

[52] L. T. Hall, G. C. Beart, E. A. Thomas, D. A. Simpson, L. P. McGuinness, J. H. Cole, J. H. Manton, R. E. Scholten, F. Jelezko, J. Wrachtrup, S. Petrou, and L. C. Hollenberg, "High spatial and temporal resolution wide-field imaging of neuron activity using quantum nv-diamond," *Sci Rep*, vol. 2, p. 401, 2012.

[53] F. M. Hossain, M. W. Doherty, H. F. Wilson, and L. C. Hollenberg, “Ab initio electronic and optical properties of the n - v- center in diamond,” *Phys Rev Lett*, vol. 101, no. 22, p. 226403, 2008.

[54] J. Wang, F. Feng, J. Zhang, J. Chen, Z. Zheng, L. Guo, W. Zhang, X. Song, G. Guo, L. Fan, C. Zou, L. Lou, W. Zhu, and G. Wang, “High-sensitivity temperature sensing using an implanted single nitrogen-vacancy center array in diamond,” *Physical Review B*, vol. 91, no. 15, p. 155404, 2015.

[55] V. M. Acosta, E. Bauch, M. P. Ledbetter, A. Waxman, L. S. Bouchard, and D. Budker, “Temperature dependence of the nitrogen-vacancy magnetic resonance in diamond,” *Phys Rev Lett*, vol. 104, no. 7, p. 070801, 2010.

[56] D. Genovese, S. Bonacchi, R. Juris, M. Montalti, L. Prodi, E. Rampazzo, and N. Zaccheroni, “Prevention of self-quenching in fluorescent silica nanoparticles by efficient energy transfer,” *Angew Chem Int Ed Engl*, vol. 52, no. 23, pp. 5965–8, 2013.

[57] O. Shenderova, N. Nunn, T. Oeckinghaus, M. Torelli, G. McGuire, K. Smith, E. Danilov, R. Reuter, J. Wrachtrup, A. Shames, D. Filonova, and A. Kinev, “Commercial quantities of ultrasmall fluorescent nanodiamonds containing color centers,” vol. 10118, pp. 1011803–1011803–16.

[58] J. Wehling, R. Dringen, R. N. Zare, M. Maas, and K. Rezwan, “Bactericidal activity of partially oxidized nanodiamonds,” *ACS Nano*, vol. 8, no. 6, pp. 6475–83, 2014.

[59] G. Jarre, Y. Liang, P. Betz, D. Lang, and A. Krueger, “Playing the surface game-diels-alder reactions on diamond nanoparticles,” *Chem Commun (Camb)*, vol. 47, no. 1, pp. 544–6, 2011.

[60] Y. Liang, T. Meinhardt, G. Jarre, M. Ozawa, P. Vrdoljak, A. Scholl, F. Reinert, and A. Krueger, “Deagglomeration and surface modification of thermally annealed nanoscale diamond,” *J Colloid Interface Sci*, vol. 354, no. 1, pp. 23–30, 2011.

[61] K. Turcheniuk and V. N. Mochalin, "Biomedical applications of nanodiamond (review)," *Nanotechnology*, vol. 28, no. 25, p. 252001, 2017.

[62] A. Kruger, Y. Liang, G. Jarre, and J. Stegk, "Surface functionalisation of detonation diamond suitable for biological applications," *journal of Materials Chemistry*, vol. 16, no. 24, pp. 2322–2328, 2006.

[63] L. C. Huang and H. C. Chang, "Adsorption and immobilization of cytochrome c on nanodiamonds," *Langmuir*, vol. 20, no. 14, pp. 5879–84, 2004.

[64] N. Kossovsky, A. Gelman, H. J. Hnatyszyn, S. Rajguru, R. L. Garrell, S. Torbati, S. S. Freitas, and G. M. Chow, "Surface-modified diamond nanoparticles as antigen delivery vehicles," *Bioconjug Chem*, vol. 6, no. 5, pp. 507–11, 1995.

[65] K. Ushizawa, Y. Sato, T. Mitsumori, T. Machinami, T. Ueda, and T. Ando, "Covalent immobilization of dna on diamond and its verification by diffuse reflectance infrared spectroscopy," *Chemical Physics Letters*, vol. 351, no. 1, pp. 105–108, 2002.

[66] J. Havlik, H. Raabova, M. Gulka, V. Petrakova, M. Krecmarova, V. Masek, P. Lousa, J. Stursa, H.-G. Boyen, M. Nesladek, and P. Cigler, "Benchtop fluorination of fluorescent nanodiamonds on a preparative scale: Toward unusually hydrophilic bright particles," *Advanced Functional Materials*, vol. 26, no. 23, pp. 4134–4142, 2016.

[67] Y. C. Lin, K. T. Wu, Z. R. Lin, E. Perevedentseva, A. Karmenyan, M. D. Lin, and C. L. Cheng, "Nanodiamond for biolabelling and toxicity evaluation in the zebrafish embryo in vivo," *J Biophotonics*, vol. 9, no. 8, pp. 827–36, 2016.

[68] N. Mohan, C.-S. Chen, H.-H. Hsieh, Y.-C. Wu, and H.-C. Chang, "In vivo imaging and toxicity assessments of fluorescent nanodiamonds in caenorhabditis elegans," *Nano Letters*, vol. 10, no. 9, pp. 3692–3699, 2010.

[69] S. J. Yu, M. W. Kang, H. C. Chang, K. M. Chen, and Y. C. Yu, "Bright fluorescent nanodiamonds: no photobleaching and low cytotoxicity," *J Am Chem Soc*, vol. 127, no. 50, pp. 17604–5, 2005.

[70] V. Vaijayanthimala, P. Y. Cheng, S. H. Yeh, K. K. Liu, C. H. Hsiao, J. I. Chao, and H. C. Chang, “The long-term stability and biocompatibility of fluorescent nanodiamond as an in vivo contrast agent,” *Biomaterials*, vol. 33, no. 31, pp. 7794–802, 2012.

[71] A. M. Schrand, S. A. C. Hens, and O. A. Shenderova, “Nanodiamond particles: Properties and perspectives for bioapplications,” *Critical Reviews in Solid State and Materials Sciences*, vol. 34, no. 1-2, pp. 18–74, 2009.

[72] H. Huang, E. Pierstorff, E. Osawa, and D. Ho, “Active nanodiamond hydrogels for chemotherapeutic delivery,” *Nano Lett*, vol. 7, no. 11, pp. 3305–14, 2007.

[73] E. K. Chow, X. Q. Zhang, M. Chen, R. Lam, E. Robinson, H. Huang, D. Schaffer, E. Osawa, A. Goga, and D. Ho, “Nanodiamond therapeutic delivery agents mediate enhanced chemoresistant tumor treatment,” *Sci Transl Med*, vol. 3, no. 73, p. 73ra21, 2011.

[74] E. K. Chow, X.-Q. Zhang, M. Chen, R. Lam, E. Robinson, H. Huang, D. Schaffer, E. Osawa, A. Goga, and D. Ho, “Nanodiamond therapeutic delivery agents mediate enhanced chemoresistant tumor treatment,” *Science Translational Medicine*, vol. 3, no. 73, pp. 73ra21–73ra21, 2011.

[75] Landeros-Mart, xed, L.-L. nez, D. Chavez-Flores, E. Orrantia-Borunda, and N. Flores-Holguin, “Construction of a nanodiamond tamoxifen complex as a breast cancer drug delivery vehicle,” *journal of Nanomaterials*, vol. 2016, p. 9, 2016.

[76] B. Guan, F. Zou, and J. Zhi, “Nanodiamond as the ph-responsive vehicle for an anticancer drug,” *Small*, vol. 6, no. 14, pp. 1514–9, 2010.

[77] M. Chen, E. D. Pierstorff, R. Lam, S. Y. Li, H. Huang, E. Osawa, and D. Ho, “Nanodiamond-mediated delivery of water-insoluble therapeutics,” *ACS Nano*, vol. 3, no. 7, pp. 2016–22, 2009.

[78] T. B. Toh, D. K. Lee, W. Hou, L. N. Abdullah, J. Nguyen, D. Ho, and E. K. Chow, “Nanodiamond-mitoxantrone complexes enhance drug retention in chemoresistant breast cancer cells,” *Mol Pharm*, vol. 11, no. 8, pp. 2683–91, 2014.

[79] R. A. Shimkunas, E. Robinson, R. Lam, S. Lu, X. Xu, X. Q. Zhang, H. Huang, E. Osawa, and D. Ho, “Nanodiamond-insulin complexes as ph-dependent protein delivery vehicles,” *Biomaterials*, vol. 30, no. 29, pp. 5720–8, 2009.

[80] J. Slegerova, M. Hajek, I. Rehor, F. Sedlak, J. Stursa, M. Hruby, and P. Cigler, “Designing the nanobiointerface of fluorescent nanodiamonds: highly selective targeting of glioma cancer cells,” *Nanoscale*, vol. 7, no. 2, pp. 415–20, 2015.

[81] Y. Wu, A. Ermakova, W. Liu, G. Pramanik, T. M. Vu, A. Kurz, L. McGuinness, B. Naydenov, S. Hafner, R. Reuter, J. Wrachtrup, J. Isoya, C. FÃűrtsch, H. Barth, T. Simmet, F. Jelezko, and T. Weil, “Programmable biopolymers for advancing biomedical applications of fluorescent nanodiamonds,” *Advanced Functional Materials*, vol. 25, no. 42, pp. 6576–6585, 2015.

[82] D. Jaque and F. Vetrone, “Luminescence nanothermometry,” *Nanoscale*, vol. 4, no. 15, pp. 4301–4326, 2012.

[83] C.-C. Fu, H.-Y. Lee, K. Chen, T.-S. Lim, H.-Y. Wu, P.-K. Lin, P.-K. Wei, P.-H. Tsao, H.-C. Chang, and W. Fann, “Characterization and application of single fluorescent nanodiamonds as cellular biomarkers,” *Proceedings of the National Academy of Sciences*, vol. 104, no. 3, pp. 727–732, 2007.

[84] Y. R. Chang, H. Y. Lee, K. Chen, C. C. Chang, D. S. Tsai, C. C. Fu, T. S. Lim, Y. K. Tzeng, C. Y. Fang, C. C. Han, H. C. Chang, and W. Fann, “Mass production and dynamic imaging of fluorescent nanodiamonds,” *Nat Nanotechnol*, vol. 3, no. 5, pp. 284–8, 2008.

[85] L. P. McGuinness, Y. Yan, A. Stacey, D. A. Simpson, L. T. Hall, D. Maclaurin, S. Prawer, P. Mulvaney, J. Wrachtrup, F. Caruso, R. E. Scholten, and L. C. Hollenberg, “Quantum measurement and orientation tracking of fluorescent nanodiamonds inside living cells,” *Nat Nanotechnol*, vol. 6, no. 6, pp. 358–63, 2011.

[86] P. Neumann, I. Jakobi, F. Dolde, C. Burk, R. Reuter, G. Waldherr, J. Honert, T. Wolf, A. Brunner, and J. H. Shim, “High-precision nanoscale temperature sensing using single

defects in diamond," *Nano Lett*, vol. 13, no. 6, pp. 2738–42, 2013.

[87] D. M. Toyli, C. F. de las Casas, D. J. Christle, V. V. Dobrovitski, and D. D. Awschalom, "Fluorescence thermometry enhanced by the quantum coherence of single spins in diamond," *Proc Natl Acad Sci U S A*, vol. 110, no. 21, pp. 8417–21, 2013.

[88] Y.-K. Tzeng, P.-C. Tsai, H.-Y. Liu, O. Y. Chen, H. Hsu, F.-G. Yee, M.-S. Chang, and H.-C. Chang, "Time-resolved luminescence nanothermometry with nitrogen-vacancy centers in nanodiamonds," *Nano Letters*, vol. 15, no. 6, pp. 3945–3952, 2015. PMID: 25951304.

[89] T. Plakhotnik, M. W. Doherty, J. H. Cole, R. Chapman, and N. B. Manson, "All-optical thermometry and thermal properties of the optically detected spin resonances of the nv(-) center in nanodiamond," *Nano Lett*, vol. 14, no. 9, pp. 4989–96, 2014.

[90] Y. K. Tzeng, P. C. Tsai, H. Y. Liu, O. Y. Chen, H. Hsu, F. G. Yee, M. S. Chang, and H. C. Chang, "Time-resolved luminescence nanothermometry with nitrogen-vacancy centers in nanodiamonds," *Nano Lett*, vol. 15, no. 6, pp. 3945–52, 2015.

[91] N. Wang, G.-Q. Liu, W.-H. Leong, H.-L. Zeng, X. Feng, S.-H. Li, F. Dolde, H. Fedder, J. Wrachtrup, and X.-D. Cui, "Magnetic criticality-enhanced hybrid nanodiamond-thermometer under ambient conditions," *arXiv preprint arXiv:1707.02885*, 2017.

[92] C. T. Nguyen, R. E. Evans, A. Sipahigil, M. K. Bhaskar, D. D. Sukachev, V. N. Agafonov, V. A. Davydov, L. F. Kulikova, F. Jelezko, and M. D. Lukin, "All-optical nanoscale thermometry with silicon-vacancy centers in diamond," *arXiv preprint arXiv:1708.05419*, 2017.

[93] J.-W. Fan, I. Cojocaru, J. Becker, I. V. Fedotov, M. H. A. Alkahtani, A. Alajlan, S. Blakley, M. Rezaee, A. Lyamkina, Y. N. Palyanov, Y. M. Borzdov, Y.-P. Yang, A. Zheltikov, P. Hemmer, and A. V. Akimov, "Germanium-vacancy color center in diamond as a temperature sensor," *ACS Photonics*, 2018.

[94] G. Baffou, H. Rigneault, D. Marguet, and L. Jullien, "A critique of methods for temperature imaging in single cells," *Nat Methods*, vol. 11, no. 9, pp. 899–901, 2014.

[95] M. Alkahtani, L. Jiang, R. Brick, P. Hemmer, and M. Scully, "Nanometer-scale luminescent thermometry in bovine embryos," *Opt Lett*, vol. 42, no. 23, pp. 4812–4815, 2017.

[96] E. O. Gracheva, J. F. Cordero-Morales, J. A. Gonzalez-Carcacia, N. T. Ingolia, C. Manno, C. I. Aranguren, J. S. Weissman, and D. Julius, "Ganglion-specific splicing of trpv1 underlies infrared sensation in vampire bats," *Nature*, vol. 476, no. 7358, pp. 88–91, 2011.

[97] J. Vriens, B. Nilius, and T. Voets, "Peripheral thermosensation in mammals," *Nat Rev Neurosci*, vol. 15, no. 9, pp. 573–89, 2014.

[98] D. D. McKemy, W. M. Neuhausser, and D. Julius, "Identification of a cold receptor reveals a general role for trp channels in thermosensation," *Nature*, vol. 416, no. 6876, pp. 52–8, 2002.

[99] A. A. Lanin, I. V. Fedotov, Y. G. Ermakova, D. A. Sidorov-Biryukov, A. B. Fedotov, P. Hemmer, V. V. Belousov, and A. M. Zheltikov, "Fiber-optic electron-spin-resonance thermometry of single laser-activated neurons," *Opt Lett*, vol. 41, no. 23, pp. 5563–5566, 2016.

[100] B. R. Masters, "Fluorescence microscopy: From principles to biological applications," *journal of Biomedical Optics*, vol. 19, no. 4, pp. 049901–049901, 2014.

[101] Z. Zhehai and Z. Lianqing, "Sted microscopy based on axially symmetric polarized vortex beams," *Chinese Physics B*, vol. 25, no. 3, p. 030701, 2016.

[102] E. Rittweger, K. Y. Han, S. E. Irvine, C. Eggeling, and S. W. Hell, "Sted microscopy reveals crystal colour centres with nanometric resolution," *Nature Photonics*, vol. 3, p. 144, 2009.

[103] K. Y. Han, K. I. Willig, E. Rittweger, F. Jelezko, C. Eggeling, and S. W. Hell, "Three-dimensional stimulated emission depletion microscopy of nitrogen-vacancy centers in diamond using continuous-wave light," *Nano Lett*, vol. 9, no. 9, pp. 3323–9, 2009.

[104] Y. K. Tzeng, O. Faklaris, B. M. Chang, Y. Kuo, J. H. Hsu, and H. C. Chang, "Superresolution imaging of albumin-conjugated fluorescent nanodiamonds in cells by stimulated emission depletion," *Angew Chem Int Ed Engl*, vol. 50, no. 10, pp. 2262–5, 2011.

[105] S. Arroyo-Camejo, M. P. Adam, M. Besbes, J. P. Hugonin, V. Jacques, J. J. Greffet, J. F. Roch, S. W. Hell, and F. Treussart, "Stimulated emission depletion microscopy resolves individual nitrogen vacancy centers in diamond nanocrystals," *ACS Nano*, vol. 7, no. 12, pp. 10912–9, 2013.

[106] B. D. Armstrong and S. Han, "A new model for overhauser enhanced nuclear magnetic resonance using nitroxide radicals," *J Chem Phys*, vol. 127, no. 10, p. 104508, 2007.

[107] U. L. Gunther, "Dynamic nuclear hyperpolarization in liquids," *Top Curr Chem*, vol. 335, pp. 23–69, 2013.

[108] A. E. Fischer and L. D. Hall, "Roles for paramagnetic substances in mri: contrast agents, molecular amplifiers, and indicators for redox and ph mapping," *Magnetic Resonance Materials in Physics, Biology and Medicine*, vol. 2, no. 3, pp. 203–210, 1994.

[109] M. C. Cassidy, H. R. Chan, B. D. Ross, P. K. Bhattacharya, and C. M. Marcus, "In vivo magnetic resonance imaging of hyperpolarized silicon particles," *Nature Nanotechnology*, vol. 8, p. 363, 2013.

[110] L. M. Manus, D. J. Mastarone, E. A. Waters, X.-Q. Zhang, E. A. Schultz-Sikma, K. W. MacRenaris, D. Ho, and T. J. Meade, "Gd(iii)-nanodiamond conjugates for mri contrast enhancement," *Nano Letters*, vol. 10, no. 2, pp. 484–489, 2010.

[111] R. J. McDonald, J. S. McDonald, D. F. Kallmes, M. E. Jentoft, D. L. Murray, K. R. Thielen, E. E. Williamson, and L. J. Eckel, "Intracranial gadolinium deposition after contrast-enhanced mr imaging," *Radiology*, vol. 275, no. 3, pp. 772–82, 2015.

[112] D. E. J. Waddington, M. Sarracanie, H. Zhang, N. Salameh, D. R. Glenn, E. Rej, T. Gaebel, T. Boele, R. L. Walsworth, D. J. Reilly, and M. S. Rosen, "Nanodiamond-enhanced mri via in situ hyperpolarization," *Nat Commun*, vol. 8, p. 15118, 2017.

[113] D. J. Lurie, H. Li, S. Petryakov, and J. L. Zweier, "Development of a pedri free-radical imager using a 0.38 t clinical mri system," *Magn Reson Med*, vol. 47, no. 1, pp. 181–6, 2002.

[114] K. Golman, I. Leunbach, J. S. Petersson, D. Holz, and J. Overweg, “Overhauser-enhanced mri,” *Acad Radiol*, vol. 9 Suppl 1, pp. S104–8, 2002.

[115] N. Koonjoo, E. Parzy, P. Massot, M. Lepetit-Coiffe, S. R. Marque, J. M. Franconi, E. Thiaudiere, and P. Mellet, “In vivo overhauser-enhanced mri of proteolytic activity,” *Contrast Media Mol Imaging*, vol. 9, no. 5, pp. 363–71, 2014.

[116] K. Ichikawa and K. Yasukawa, “Imaging in vivo redox status in high spatial resolution with omri,” *Free Radic Res*, vol. 46, no. 8, pp. 1004–10, 2012.

[117] M. Sarracanie, B. D. Armstrong, J. Stockmann, and M. S. Rosen, “High speed 3d overhauser-enhanced mri using combined b-ssfp and compressed sensing,” *Magn Reson Med*, vol. 71, no. 2, pp. 735–45, 2014.

[118] R. B. Clarkson, B. M. Odintsov, P. J. Ceroke, J. H. Ardenkjaer-Larsen, M. Fruianu, and R. L. Belford, “Electron paramagnetic resonance and dynamic nuclear polarization of char suspensions: surface science and oximetry,” *Phys Med Biol*, vol. 43, no. 7, pp. 1907–20, 1998.

[119] J. H. Ardenkjaer-Larsen, I. Laursen, I. Leunbach, G. Ehnholm, L. G. Wistrand, J. S. Petersson, and K. Golman, “Epr and dnp properties of certain novel single electron contrast agents intended for oximetric imaging,” *J Magn Reson*, vol. 133, no. 1, pp. 1–12, 1998.

[120] S. Jochen, S. Ilai, C. Qiong, S.-S. David, C. Patrick, H. Peter, R. Alexander, S. Hitoshi, I. Junichi, L. Burkhard, B. P. Martin, N. Boris, and J. Fedor, “Optically induced dynamic nuclear spin polarisation in diamond,” *New journal of Physics*, vol. 18, no. 1, p. 013040, 2016.

[121] J. P. King, P. J. Coles, and J. A. Reimer, “Optical polarization of ^{13}C nuclei in diamond through nitrogen vacancy centers,” *Physical Review B*, vol. 81, no. 7, p. 073201, 2010.

[122] E. Rej, T. Gaebel, T. Boele, D. E. Waddington, and D. J. Reilly, “Hyperpolarized nanodiamond with long spin-relaxation times,” *Nat Commun*, vol. 6, p. 8459, 2015.

[123] J. P. King, K. Jeong, C. C. Vassiliou, C. S. Shin, R. H. Page, C. E. Avalos, H. J. Wang, and A. Pines, “Room-temperature in situ nuclear spin hyperpolarization from optically pumped nitrogen vacancy centres in diamond,” *Nat Commun*, vol. 6, p. 8965, 2015.

[124] L. B. Casabianca, A. I. Shames, A. M. Panich, O. Shenderova, and L. Frydman, “Factors affecting dnp nmr in polycrystalline diamond samples,” *The journal of Physical Chemistry C*, vol. 115, no. 39, pp. 19041–19048, 2011.

[125] P. Dutta, G. V. Martinez, and R. J. Gillies, “Nanodiamond as a new hyperpolarizing agent and its 13c mrs,” *The journal of Physical Chemistry Letters*, vol. 5, no. 3, pp. 597–600, 2014.

[126] L. Kuang-Kai, C. Chia-Liang, C. Chia-Ching, and I. C. Jui, “Biocompatible and detectable carboxylated nanodiamond on human cell,” *Nanotechnology*, vol. 18, no. 32, p. 325102, 2007.

[127] I. Vlasov, A. A. Shiryaev, T. Rendler, S. Steinert, S. Y. Lee, D. Antonov, M. Voros, F. Jelezko, A. V. Fisenko, L. F. Semjonova, J. Biskupek, U. Kaiser, O. I. Lebedev, I. Sildos, P. R. Hemmer, V. I. Konov, A. Gali, and J. Wrachtrup, “Molecular-sized fluorescent nanodiamonds,” *Nat Nanotechnol*, vol. 9, no. 1, pp. 54–8, 2014.

[128] J. Uwe, B. K. Andrea, S. R. Daniel, S. Clemens, D. J. Kay, L. A. Ulrik, A. D. Valery, N. A. Viatcheslav, K. Alexander, J. R. Lachlan, and J. Fedor, “Nanodiamonds carrying silicon-vacancy quantum emitters with almost lifetime-limited linewidths,” *New journal of Physics*, vol. 18, no. 7, p. 073036, 2016.

[129] I. Aharonovich, C. Zhou, A. Stacey, J. Orwa, S. Castelletto, D. Simpson, A. D. Greentree, F. Treussart, J.-F. Roch, and S. Prawer, “Enhanced single-photon emission in the near infrared from a diamond color center,” *Physical Review B*, vol. 79, no. 23, p. 235316, 2009.

[130] M. H. Nazare, A. J. Neves, and G. Davies, “Optical studies of the 1.40-ev ni center in diamond,” *Phys Rev B Condens Matter*, vol. 43, no. 17, pp. 14196–14205, 1991.

[131] T. Iwasaki, F. Ishibashi, Y. Miyamoto, Y. Doi, S. Kobayashi, T. Miyazaki, K. Tahara, K. D. Jahnke, L. J. Rogers, B. Naydenov, F. Jelezko, S. Yamasaki, S. Nagamachi, T. Inubushi, N. Mizuochi, and M. Hatano, "Germanium-vacancy single color centers in diamond," *Sci Rep*, vol. 5, p. 12882, 2015.

[132] R. Igarashi, Y. Yoshinari, H. Yokota, T. Sugi, F. Sugihara, K. Ikeda, H. Sumiya, S. Tsuji, I. Mori, H. Tochio, Y. Harada, and M. Shirakawa, "Real-time background-free selective imaging of fluorescent nanodiamonds in vivo," *Nano Lett*, vol. 12, no. 11, pp. 5726–32, 2012.

[133] A. Hegyi and E. Yablonovitch, "Molecular imaging by optically detected electron spin resonance of nitrogen-vacancies in nanodiamonds," *Nano Lett*, vol. 13, no. 3, pp. 1173–8, 2013.

[134] T. Zapata, N. Bennett, V. Struzhkin, Y. Fei, F. Jelezko, J. Biskupek, R. Kaiser, Reuter, J. Wrachtrup, F. A. Ghannam, and P. Hemmer, "Organic nanodiamonds," *arXiv:1702.06854*, vol. 1702, 2017.

[135] S. Waldchen, J. Lehmann, T. Klein, S. van de Linde, and M. Sauer, "Light-induced cell damage in live-cell super-resolution microscopy," *Sci Rep*, vol. 5, p. 15348, 2015.

[136] N. Bloembergen, "Solid state infrared quantum counters," *Physical Review Letters*, vol. 2, no. 3, pp. 84–85, 1959.

[137] F. Auzel and D. Pecile, "Absolute efficiency for ir to blue conversion materials and theoretical prediction for optimized matrices," *journal of Luminescence*, vol. 11, no. 5, pp. 321–330, 1976.

[138] F. Auzel and D. Pecile, "Comparison and efficiency of materials for summation of photons assisted by energy transfer," *journal of Luminescence*, vol. 8, no. 1, pp. 32–43, 1973.

[139] F. Auzel, "Upconversion and anti-stokes processes with f and d ions in solids," *Chem Rev*, vol. 104, no. 1, pp. 139–73, 2004.

[140] C. T. Xu, Q. Zhan, H. Liu, G. Somesfalean, J. Qian, S. He, and S. Andersson-Engels, "Upconverting nanoparticles for pre-clinical diffuse optical imaging, microscopy and sensing:

Current trends and future challenges," *Laser & Photonics Reviews*, vol. 7, no. 5, pp. 663–697, 2013.

[141] M. Haase and H. Schafer, "Upconverting nanoparticles," *Angew Chem Int Ed Engl*, vol. 50, no. 26, pp. 5808–29, 2011.

[142] G. W. Faris, W. H. Wright, S. Pati, L. V. Schneider, D. A. E. D. S.-M. E. Zarling, and D. Benaron, "Upconverting reporters for biomedical diagnostics: Applications in antibody and dna detection," in *Biomedical Optical Spectroscopy and Diagnostics*, vol. 3 of *OSA Trends in Optics and Photonics Series*, p. DR2, Optical Society of America.

[143] G. W. Faris, W. H. Wright, M. P. Hall, Y. Chen, Y.-M. M. Yao, N. A. Mufti, D. E. E. D. S.-M. E. Cooper, and J. Izatt, "Upconverting phosphors as reporters for immunoassay," in *Biomedical Optical Spectroscopy and Diagnostics / Therapeutic Laser Applications*, vol. 22 of *OSA Trends in Optics and Photonics*, p. BTuB4, Optical Society of America.

[144] J. Hampl, M. Hall, N. A. Mufti, Y. M. Yao, D. B. MacQueen, W. H. Wright, and D. E. Cooper, "Upconverting phosphor reporters in immunochromatographic assays," *Anal Biochem*, vol. 288, no. 2, pp. 176–87, 2001.

[145] K. Schenke-Layland, I. Riemann, O. Damour, U. A. Stock, and K. Konig, "Two-photon microscopes and in vivo multiphoton tomographs–powerful diagnostic tools for tissue engineering and drug delivery," *Adv Drug Deliv Rev*, vol. 58, no. 7, pp. 878–96, 2006.

[146] J. Chen and J. X. Zhao, "Upconversion nanomaterials: synthesis, mechanism, and applications in sensing," *Sensors (Basel)*, vol. 12, no. 3, pp. 2414–35, 2012.

[147] X. Li, F. Zhang, and D. Zhao, "Highly efficient lanthanide upconverting nanomaterials: Progresses and challenges," *Nano Today*, vol. 8, no. 6, pp. 643–676, 2013.

[148] G. Mialon, S. TÃijrkcan, G. Dantelle, D. P. Collins, M. Hadjipanayi, R. A. Taylor, T. Gacoin, A. Alexandrou, and J.-P. Boilot, "High up-conversion efficiency of yvo4:yb,er nanoparticles in water down to the single-particle level," *The journal of Physical Chemistry C*, vol. 114, no. 51, pp. 22449–22454, 2010.

[149] Z. Li, Y. Zhang, and S. Jiang, "Multicolor core/shell-structured upconversion fluorescent nanoparticles," *Advanced Materials*, vol. 20, no. 24, pp. 4765–4769, 2008.

[150] S. Wu, G. Han, D. J. Milliron, S. Aloni, V. Altoe, D. V. Talapin, B. E. Cohen, and P. J. Schuck, "Non-blinking and photostable upconverted luminescence from single lanthanide-doped nanocrystals," *Proc Natl Acad Sci U S A*, vol. 106, no. 27, pp. 10917–21, 2009.

[151] L. Xiong, Z. Chen, Q. Tian, T. Cao, C. Xu, and F. Li, "High contrast upconversion luminescence targeted imaging in vivo using peptide-labeled nanophosphors," *Anal Chem*, vol. 81, no. 21, pp. 8687–94, 2009.

[152] H. J. Zijlmans, J. Bonnet, J. Burton, K. Kardos, T. Vail, R. S. Niedbala, and H. J. Tanke, "Detection of cell and tissue surface antigens using up-converting phosphors: a new reporter technology," *Anal Biochem*, vol. 267, no. 1, pp. 30–6, 1999.

[153] G. Jiang, S. Zhou, X. Wei, Y. Chen, C. Duan, M. Yin, B. Yang, and W. Cao, "794 nm excited core-shell upconversion nanoparticles for optical temperature sensing," *RSC Advances*, vol. 6, no. 14, pp. 11795–11801, 2016.

[154] O. A. Savchuk, J. J. Carvajal, C. Cascales, J. Massons, M. Aguilo, and F. Diaz, "Thermochromic upconversion nanoparticles for visual temperature sensors with high thermal, spatial and temporal resolution," *journal of Materials Chemistry C*, vol. 4, no. 27, pp. 6602–6613, 2016.

[155] X. Zhu, W. Feng, J. Chang, Y. W. Tan, J. Li, M. Chen, Y. Sun, and F. Li, "Temperature-feedback upconversion nanocomposite for accurate photothermal therapy at facile temperature," *Nat Commun*, vol. 7, p. 10437, 2016.

[156] T. V. GavriloviÄĞ, D. J. JovanoviÄĞ, V. Lojpur, and M. D. DramiÄĞanin, "Multifunctional eu3+- and er3+/yb3+-doped gdvo4 nanoparticles synthesized by reverse micelle method," *Scientific Reports*, vol. 4, p. 4209, 2014.

[157] S. Wilhelm, M. Kaiser, C. Wurth, J. Heiland, C. Carrillo-Carrion, V. Muhr, O. S. Wolfbeis, W. J. Parak, U. Resch-Genger, and T. Hirsch, "Water dispersible upconverting nanoparticles:

effects of surface modification on their luminescence and colloidal stability," *Nanoscale*, vol. 7, no. 4, pp. 1403–10, 2015.

[158] J.-C. Boyer and F. C. J. M. van Veggel, "Absolute quantum yield measurements of colloidal nayf4: Er3+, yb3+ upconverting nanoparticles," *Nanoscale*, vol. 2, no. 8, pp. 1417–1419, 2010.

[159] D. J. Gargas, E. M. Chan, A. D. Ostrowski, S. Aloni, M. V. Altoe, E. S. Barefard, B. Sanii, J. J. Urban, D. J. Milliron, B. E. Cohen, and P. J. Schuck, "Engineering bright sub-10-nm upconverting nanocrystals for single-molecule imaging," *Nat Nanotechnol*, vol. 9, no. 4, pp. 300–5, 2014.

[160] Y. Sun, H. Liu, X. Wang, X. Kong, and H. Zhang, "Optical spectroscopy and visible upconversion studies of yvo4:er3+ nanocrystals synthesized by a hydrothermal process," *Chemistry of Materials*, vol. 18, no. 11, pp. 2726–2732, 2006.

[161] T. Taniguchi, K. Soga, K. Tokuzen, K. Tsujiuchi, T. Kidokoro, K. Tomita, K.-i. Katsumata, N. Matsushita, and K. Okada, "Nir-excited nir and visible luminescent properties of amphipathic yvo4: Er3+/yb3+ nanoparticles," *journal of Materials Science*, vol. 47, no. 5, pp. 2241–2247, 2012.

[162] G. Mialon, S. TÃijrkcan, A. Alexandrou, T. Gacoin, and J. P. Boilot, "New insights into size effects in luminescent oxide nanocrystals," *The journal of Physical Chemistry C*, vol. 113, no. 43, pp. 18699–18706, 2009.

[163] Q. Liu, W. Feng, T. Yang, T. Yi, and F. Li, "Upconversion luminescence imaging of cells and small animals," *Nat Protoc*, vol. 8, no. 10, pp. 2033–44, 2013.

[164] X. Xie, N. Gao, R. Deng, Q. Sun, Q. H. Xu, and X. Liu, "Mechanistic investigation of photon upconversion in nd(3+)-sensitized core-shell nanoparticles," *J Am Chem Soc*, vol. 135, no. 34, pp. 12608–11, 2013.

[165] F. LiÃľgard, J. L. Doualan, R. MoncorgÃľ, and M. Bettinelli, “Nd3+ âĘŠ yb3+ energy transfer in a codoped metaphosphate glass as a model for yb3+ laser operation around 980 nm,” *Applied Physics B*, vol. 80, no. 8, pp. 985–991, 2005.

[166] F. Wang, R. Deng, J. Wang, Q. Wang, Y. Han, H. Zhu, X. Chen, and X. Liu, “Tuning upconversion through energy migration in core-shell nanoparticles,” *Nat Mater*, vol. 10, no. 12, pp. 968–73, 2011.

[167] M. H. Alkahtani, C. L. Gomes, and P. R. Hemmer, “Engineering water-tolerant core/shell upconversion nanoparticles for optical temperature sensing,” *Opt Lett*, vol. 42, no. 13, pp. 2451–2454, 2017.

[168] J. Tisler, G. Balasubramanian, B. Naydenov, R. Kolesov, B. Grotz, R. Reuter, J. P. Boudou, P. A. Curmi, M. Sennour, A. Thorel, M. Borsch, K. Aulenbacher, R. Erdmann, P. R. Hemmer, F. Jelezko, and J. Wrachtrup, “Fluorescence and spin properties of defects in single digit nanodiamonds,” *ACS Nano*, vol. 3, no. 7, pp. 1959–65, 2009.

[169] V. N. Mochalin, O. Shenderova, D. Ho, and Y. Gogotsi, “The properties and applications of nanodiamonds,” *Nat Nanotechnol*, vol. 7, no. 1, pp. 11–23, 2011.

[170] D. Amans, A.-C. Chenus, G. Ledoux, C. Dujardin, C. Reynaud, O. Sublemontier, K. Masenelli-Varlot, and O. Guillois, “Nanodiamond synthesis by pulsed laser ablation in liquids,” *Diamond and Related Materials*, vol. 18, no. 2, pp. 177–180, 2009.

[171] A. K. Khachatryan, S. G. Aloyan, P. W. May, R. Sargsyan, V. A. Khachatryan, and V. S. Baghdasaryan, “Graphite-to-diamond transformation induced by ultrasound cavitation,” *Diamond and Related Materials*, vol. 17, no. 6, pp. 931–936, 2008.

[172] N. Elke, S. David, R.-M. Janine, G. Stefan, F. Martin, S. Matthias, and B. Christoph, “Single photon emission from silicon-vacancy colour centres in chemical vapour deposition nanodiamonds on iridium,” *New journal of Physics*, vol. 13, no. 2, p. 025012, 2011.

[173] A. Kumar, P. Ann Lin, A. Xue, B. Hao, Y. Khin Yap, and R. M. Sankaran, “Formation of nanodiamonds at near-ambient conditions via microplasma dissociation of ethanol vapour,” *Nat Commun*, vol. 4, p. 2618, 2013.

[174] V. A. Davydov, A. V. Rakhmanina, V. N. Agafonov, and V. N. Khabashesku, “Synergistic effect of fluorine and hydrogen on processes of graphite and diamond formation from fluorographite-naphthalene mixtures at high pressures,” *The journal of Physical Chemistry C*, vol. 115, no. 43, pp. 21000–21008, 2011.

[175] V. A. Davydov, A. V. Rakhmanina, S. G. Lyapin, I. D. Ilichev, K. N. Boldyrev, A. A. Shiryaev, and V. N. Agafonov, “Production of nano- and microdiamonds with si-v and n-v luminescent centers at high pressures in systems based on mixtures of hydrocarbon and fluorocarbon compounds,” *JETP Letters*, vol. 99, no. 10, pp. 585–589, 2014.

[176] R. H. Wentorf, “The behavior of some carbonaceous materials at very high pressures and high temperatures,” *The journal of Physical Chemistry*, vol. 69, no. 9, pp. 3063–3069, 1965.

[177] J. L. Zhang, H. Ishiwata, T. M. Babinec, M. Radulaski, K. Muller, K. G. Lagoudakis, C. Dory, J. Dahl, R. Edgington, V. Souliere, G. Ferro, A. A. Fokin, P. R. Schreiner, Z. X. Shen, N. A. Melosh, and J. Vuckovic, “Hybrid group iv nanophotonic structures incorporating diamond silicon-vacancy color centers,” *Nano Lett*, vol. 16, no. 1, pp. 212–7, 2016.

[178] Y. K. Tzeng, J. L. Zhang, H. Lu, H. Ishiwata, J. Dahl, R. M. Carlson, H. Yan, P. R. Schreiner, J. Vuckovic, Z. X. Shen, N. Melosh, and S. Chu, “Vertical-substrate mpcvd epitaxial nanodiamond growth,” *Nano Lett*, vol. 17, no. 3, pp. 1489–1495, 2017.

[179] H. Ishiwata, J. L. Zhang, R. Edgington, T. M. Babinec, K. Muller, K. G. Lagoudakis, N. Melosh, Z.-X. Shen, and J. Vuckovic, “Fluorescent nanodiamonds from molecular diamond seed,” in *CLEO: 2015*, OSA Technical Digest (online), p. FM2E.2, Optical Society of America.

[180] J. E. P. Dahl, J. M. Moldowan, Z. Wei, P. A. Lipton, P. Denisevich, R. Gat, S. Liu, P. R. Schreiner, and R. M. K. Carlson, “Synthesis of higher diamondoids and implications for

their formation in petroleum," *Angewandte Chemie Interefational Edition*, vol. 49, no. 51, pp. 9881–9885, 2010.

[181] S. Tomoki, M. Hiroyuki, S. Koya, S. Sven, S. Minoru, S. Takehiko, and T. Kazuo, "Synthesis of diamondoids by supercritical xenon discharge plasma," *Japanese journal of Applied Physics*, vol. 50, no. 3R, p. 030207, 2011.

[182] E. Wu, J. R. Rabeau, F. Treussart, H. Zeng, P. Grangier, S. Prawer, and J. F. Roch, "Nonclassical photon statistics in a single nickelâĂŞnitrogen diamond color center photoluminescence at room temperature," *journal of Moderef Optics*, vol. 55, no. 17, pp. 2893–2901, 2008.

[183] C. E. Weir, E. R. Lippincott, A. Van Valkenburg, and E. N. Bunting, "Infrared studies in the 1- to 15-micron region to 30,000 atmospheres," vol. 63A, no. 1, p. 55, 1959.

[184] R. A. Forman, G. J. Piermarini, J. D. Barefett, and S. Block, "Pressure measurement made by the utilization of ruby sharp-line luminescence," *Science*, vol. 176, no. 4032, pp. 284–285, 1972.

[185] K. Bray, R. Sandstrom, C. Elbadawi, M. Fischer, M. Schreck, O. Shimoni, C. Lobo, M. Toth, and I. Aharonovich, "Localization of narrowband single photon emitters in nanodiamonds," *ACS Applied Materials & Interfaces*, vol. 8, no. 11, pp. 7590–7594, 2016.

[186] Y. Yue and X. Wang, "Nanoscale thermal probing," *Nano Rev*, vol. 3, 2012.

[187] J. O. Orwa, I. Aharonovich, F. Jelezko, G. Balasubramanian, P. Balog, M. Markham, D. J. Twitchen, A. D. Greentree, and S. Prawer, "Nickel related optical centres in diamond created by ion implantation," *journal of Applied Physics*, vol. 107, no. 9, p. 093512, 2010.

[188] T. SÃąra, H. LÃąszlÃş, and K. Margit, "Nickel-silicon related color center formed in nanodiamond grains under cvd growth," *journal of Nanoscience*, vol. 2015, p. 6, 2015.

[189] J. P. Goss, P. R. Briddon, R. Jones, and S. Sque, "Donor and acceptor states in diamond," *Diamond and Related Materials*, vol. 13, no. 4, pp. 684–690, 2004.

[190] N. Aslam, G. Waldherr, P. Neumann, F. Jelezko, and J. Wrachtrup, “Photo-induced ionization dynamics of the nitrogen vacancy defect in diamond investigated by single-shot charge state detection,” *New journal of Physics*, vol. 15, no. 1, p. 013064, 2013.

[191] J. Jeske, D. W. Lau, X. Vidal, L. P. McGuinness, P. Reineck, B. C. Johnson, M. W. Doherty, J. C. McCallum, S. Onoda, F. Jelezko, T. Ohshima, T. Volz, J. H. Cole, B. C. Gibson, and A. D. Greentree, “Stimulated emission from nitrogen-vacancy centres in diamond,” *Nat Commun*, vol. 8, p. 14000, 2017.

[192] Y. Doi, T. Fukui, H. Kato, T. Makino, S. Yamasaki, T. Tashima, H. Morishita, S. Miwa, F. Jelezko, Y. Suzuki, and N. Mizuochi, “Pure negatively charged state of the nv center in n-type diamond,” *Physical Review B*, vol. 93, no. 8, p. 081203, 2016.

[193] H. Foth, S. Farber, A. Gauer, and R. Wagner, “Thermal damage threshold at 633 nm of tympanic membrane of pig,” *Hear Res*, vol. 142, no. 1-2, pp. 71–8, 2000.

[194] J. Wolters, N. Sadzak, A. W. Schell, T. SchrÃűder, and O. Benson, “Measurement of the ultrafast spectral diffusion of the optical transition of nitrogen vacancy centers in nano-size diamond using correlation interferometry,” *Physical Review Letters*, vol. 110, no. 2, p. 027401, 2013.

[195] N. Elke, H. Christian, H. Michael, G. Stefan, F. Martin, S. Hadwig, S.-N. Doris, S. Matthias, and B. Christoph, “Low-temperature investigations of single silicon vacancy colour centres in diamond,” *New journal of Physics*, vol. 15, no. 4, p. 043005, 2013.

[196] Q. le Masne de Chermont, C. ChanÃl’ac, J. Seguin, F. PellÃl’, S. MaÃőtrejean, J.-P. Jolivet, D. Gourier, M. Bessodes, and D. Scherman, “Nanoprobes with near-infrared persistent luminescence for in vivo imaging,” *Proceedings of the National Academy of Sciences of the United States of America*, vol. 104, no. 22, pp. 9266–9271, 2007.

[197] J. Yang, Y. Deng, Q. Wu, J. Zhou, H. Bao, Q. Li, F. Zhang, F. Li, B. Tu, and D. Zhao, “Mesoporous silica encapsulating upconversion luminescence rare-earth fluoride nanorods for secondary excitation,” *Langmuir*, vol. 26, no. 11, pp. 8850–8856, 2010.

[198] F. Zhang, *Upconversion Nanoparticle-Based Nanocomposites*, pp. 121–157. Berlin, Heidelberg: Springer Berlin Heidelberg, 2015.

[199] J. Zhou, Y. Sun, X. Du, L. Xiong, H. Hu, and F. Li, "Dual-modality in vivo imaging using rare-earth nanocrystals with near-infrared to near-infrared (nir-to-nir) upconversion luminescence and magnetic resonance properties," *Biomaterials*, vol. 31, no. 12, pp. 3287–95, 2010.

[200] C. R. Allen, S. Demarais, and R. S. Lutz, "Red imported fire ant impact on wildlife: an overview," 1994.

[201] A. Jemal and M. Hugh-Jones, "A review of the red imported fire ant (solenopsis invicta buren) and its impacts on plant, animal, and human health," *Preventive Veterinary Medicine*, vol. 17, no. 1, pp. 19–32, 1993.

[202] Y. Chen, C. Sanchez, Y. Yue, M. de Almeida, J. M. Gonzalez, D. Y. Parkinson, and H. Liang, "Observation of yttrium oxide nanoparticles in cabbage (brassica oleracea) through dual energy k-edge subtraction imaging," *J Nanobiotechnology*, vol. 14, p. 23, 2016.

[203] T. Hulland, "Selected histochemical and histopathological methods," *The Canadian Veterinary journal*, vol. 8, no. 2, p. 51, 1967.

[204] J. H. Yao, K. R. Elder, H. Guo, and M. Grant, "Theory and simulation of ostwald ripening," *Phys Rev B Condens Matter*, vol. 47, no. 21, pp. 14110–14125, 1993.

[205] S. L. Jacques, "Optical properties of biological tissues: a review," *Phys Med Biol*, vol. 58, no. 11, pp. R37–61, 2013.

[206] Y. Chen, C. Sanchez, Y. Yue, J. M. Gonzalez, D. Y. Parkinson, and H. Liang, "Observation of two-dimensional yttrium oxide nanoparticles in mealworm beetles (tenebrio molitor)," *J Synchrotron Radiat*, vol. 23, no. Pt 5, pp. 1197–201, 2016.

[207] W. Chen, C. Shi, T. Tao, M. Ji, S. Zheng, X. Sang, X. Liu, and J. Qiu, "Optical temperature sensing with minimized heating effect using core-shell upconversion nanoparticles," *RSC Advances*, vol. 6, no. 26, pp. 21540–21545, 2016.

[208] C. de Mello DonegÃą, M. Bode, and A. Meijerink, "Size- and temperature-dependence of exciton lifetimes in cdse quantum dots," *Physical Review B*, vol. 74, no. 8, p. 085320, 2006.

[209] D. Jaque, B. D. Rosal, E. M. Rodriguez, L. M. Maestro, P. Haro-Gonzalez, and J. G. Sole, "Fluorescent nanothermometers for intracellular thermal sensing," *Nanomedicine (Lond)*, vol. 9, no. 7, pp. 1047–62, 2014.

[210] B. Han, W. L. Hanson, K. Bensalah, A. Tuncel, J. M. Steref, and J. A. Cadeddu, "Development of quantum dot-mediated fluorescence thermometry for thermal therapies," *Ann Biomed Eng*, vol. 37, no. 6, pp. 1230–9, 2009.

[211] Y. Liu, K. Ai, X. Cheng, L. Huo, and L. Lu, "Gold-nanocluster-based fluorescent sensors for highly sensitive and selective detection of cyanide in water," *Advanced Functional Materials*, vol. 20, no. 6, pp. 951–956, 2010.

[212] X. Huang, "Enhancement of near-infrared to near-infrared upconversion luminescence in sub-10-nm ultra-small laf(3):yb(3+)/tm(3+) nanoparticles through lanthanide doping," *Opt Lett*, vol. 40, no. 22, pp. 5231–4, 2015.

[213] X. Huang, "Giant enhancement of upconversion emission in (nayf4:nd3+/yb3+/ho3+)/(nayf4:nd3+/yb3+) core/shell nanoparticles excited at 808nm," *Optics Letters*, vol. 40, no. 15, pp. 3599–3602, 2015.

[214] X. Huang, "Broadband dye-sensitized upconversion: A promising new platform for future solar upconverter design," *journal of Alloys and Compounds*, vol. 690, pp. 356–359, 2017.

[215] L. Tian, Z. Xu, S. Zhao, Y. Cui, Z. Liang, J. Zhang, and X. Xu, "The upconversion luminescence of er(3+)/yb(3+)/nd(3+) triply-doped Îš-nayf(4) nanocrystals under 808-nm excitation," *Materials*, vol. 7, no. 11, pp. 7289–7303, 2014.

[216] F. Zhang, *Upconversion Nanoparticles for Thermal Sensing*, pp. 343–374. Berlin, Heidelberg: Springer Berlin Heidelberg, 2015.

[217] L. H. Fischer, G. S. Harms, and O. S. Wolfbeis, "Upconverting nanoparticles for nanoscale thermometry," *Angew Chem Int Ed Engl*, vol. 50, no. 20, pp. 4546–51, 2011.

[218] S. G. Kuntz and M. B. Eisen, "drosophila embryogenesis scales uniformly across temperature and developmentally diverse species," *bioRxiv*, 2013.

[219] R. B. . E. W. Stiling and L. G. Peter, "Biology," *McGraw-Hill*, no. 2011, 2011.

[220] P. A. Lawrence, "The embryonic development of drosophila melanogaster," *Cell*, vol. 44, no. 5, p. 671.

[221] B. Pingault, D.-D. Jarausch, C. Hepp, L. Klintberg, J. N. Becker, M. Markham, C. Becher, and M. AtatÃijre, "Coherent control of the silicon-vacancy spin in diamond," *Nature Communications*, vol. 8, p. 15579, 2017.

[222] B. Dong, T. Yang, and M. K. Lei, "Optical high temperature sensor based on green upconversion emissions in er3+ doped al2o3," *Sensors and Actuators B: Chemical*, vol. 123, no. 2, pp. 667–670, 2007.